# Engineering Three Dimensional In Vitro Approaches to Study Cardiac Injury and Repair

by

Shoshana Lea Das

B.S., Biological Engineering
B.S., Biological Sciences
Cornell University, 2016

Submitted to the Harvard-MIT Program in Health Sciences and Technology in Partial Fulfillment of the Requirements for the Degree of

Doctor of Philosophy in Medical Engineering and Medical Physics

at the

MASSACHUSETTS INSTITUTE OF TECHNOLOGY

May 2022



Signature of Author: _____
Harvard-MIT Program in Health Sciences and Technology
April 27, 2022

Certified by: _____
Christopher S. Chen, M.D., PhD.
Professor of Biomedical Engineering
Boston University
Thesis Supervisor

Accepted by: _____
Emery N. Brown, M.D., Ph.D.
Director, Harvard-MIT Program in Health Sciences and Technology
Professor of Computational Neuroscience and Health Sciences and Technology

# Engineering Three Dimensional In Vitro Approaches to Study Cardiac Injury and Repair

by

Shoshana Lea Das

Submitted to the Harvard-MIT Program of Health Sciences and Technology
On May 10, 2022, in partial fulfillment of the requirements for the degree
of Doctor of Philosophy in Medical Engineering and Medical Physics

## Abstract

Each year, over one million people in the United States have a myocardial infarction (MI). After an infarct, the affected region undergoes massive cell death and a pathological fibrotic response. As cardiomyocytes (CMs) do not regenerate, the CM content is predominately replaced by activated cardiac fibroblasts (CFs). This modifies the regional mechanical and electrical properties, which increases the risk for arrythmias and heart failure in heart attack survivors. Despite the high incidence of MI, current treatments to mitigate the associated morbidity are limited, and the development of new treatments is impeded by expensive, low-throughput, in vivo studies that poorly predict clinical success.

The goal of this dissertation is to develop 3D engineered tissue systems and technologies to study cardiac injury and healing responses. The presented work develops a series of in vitro models that recapitulate the focal fibrosis created by MI and develops tools to functionally characterize engineered heart tissue (EHT) models after injury.

First, we create a 3D biomimetic model using human induced pluripotent stem cell (iPSC)-derived CMs and primary human CFs. Using a high-power, pulsed laser, we locally injure our EHT model to reproduce the regional cell death and loss of electrical and mechanical function seen in focal fibrosis of infarcted myocardium. We then demonstrate the capacity of this model to capture cardiac remodeling and the compensatory response of the surrounding tissue after injury. Second, we adapt a genetically-encoded voltage sensor, called Archon1, to enable the study of electrical activity of individual CMs within EHTs. We use this sensor to take high fidelity action potential measurements in iPSC-derived CMs and EHTs. Finally, as myocardium is highly aligned tissue, we explore the role of extracellular matrix (ECM) alignment on injury response. We study the behavior of fibroblasts in engineered anisotropic and isotropic tissues after injury. Our results indicate that the alignment of ECM directs provisional matrix assembly, a key healing response process.

In summary, this work demonstrates the development and utility of engineered tissue systems to study cardiac injury response. Such systems can be used to better understand injury responses and probe new therapies to improve recovery.

**Thesis Supervisor:**
Christopher S. Chen, MD, PhD
Professor of Biomedical Engineering, Boston University

**Thesis Chair:**
Ellen Roche, PhD
W.M. Keck Career Development Professor in Biomedical Engineering; Associate Professor of Mechanical Engineering and of the Institute for Medical Engineering & Science, MIT

**Thesis Reader:**
Christine Seidman, M.D.
Professor of Medicine, Harvard Medical School

## Acknowledgments

The journey of a PhD is long, and it can be easy to become lost or discouraged at times. I was extremely lucky to be surrounded by countless mentors, colleagues, friends, and family who kept me excited about my work and constantly inspired me to continually grow as a scientist and person.

I would like to first and foremost thank my advisor Prof. Christopher Chen for all of his support and mentorship over the years. For the independence and trust given to me, from even the first days rotating with him, to explore ideas and opportunities both within and outside of lab. For the endless encouragement and support to start new collaborations, learn new skills, and engage in professional activities outside of lab for my own development. Chris, you have taught me a lot about navigating the scientific community, the mentorship of others, and how to balance excellence in research and other life priorities. I also want to thank you for putting together such a wonderful team of engineers and scientist to grow with and learn from.

I would like to thank Dr. Ellen Roche, for serving as my thesis chair and sharing her expertise in cardiac disease and devices, but also for being a role model over the years – for her support of me on my path and for always being my advocate. I would like to thank both Dr. Kricket Seidman and Dr. Jon Seidman for years of guidance and sharing their knowledge of cardiac biology, disease, and RNA sequencing techniques. I left every meeting with their team feeling inspired and invigorated about my work and new avenues to explore. Kricket and Jon, your excitement and love of science inspires those around you. I would particularly like to thank Kricket for serving on my thesis committee and giving clinical perspective to my work. Another big thank you to all of my collaborators over the years who helped make this work possible.

Next I would like to thank the members of the Chen Lab over the years. I consider myself very lucky to have had the opportunity to work with such an inspiring group of individuals from all over the world. I not only grew as a scientist, but professionally and personally. First, I would like to thank Dr. Jeroen Eyckmans for his scientific guidance and constant encouragement over the years, starting my first day in lab up until the last hour before my defense, for always taking the time to support and guide me. I would like to thank the whole cardiac team, but especially Kehan Zhang, Christos Michas, Jourdan Ewoldt, and Rebeccah Luu, all of whom I worked closely with over the years. I would also like to thank Marina Uroz, Jinling Yang, Linqing Li, Juliann Tefft, Jen Bays and other Chen Lab friends for your friendship and support over the years. I was lucky to be able to come into work everyday and be surrounded by such a supportive community.

Throughout the years I have been lucky to have the support of many friends outside the lab and also the MIT community. These are the people that truly made the last six years the experience that it was. A thank you to my HST cohort and other HST friends, and to all of the people I have met and befriended along the way here in Boston, particularly Efi Goffer and Hannah Emerson, for their endless support and friendship over the years as we've evolved and grown to learn more about ourselves. I am honored to belong to such a vibrant and caring community of people. For all of my Cornell friends, especially Marisa Gianfortune, Molly Dasso,

Joel Lawson, and Jessy Garcia for their constant support over the last ten years, both at Cornell and throughout my PhD. Also, to Dr. Claudia Varela, my roommate for this entire PhD journey. Being able to undergo this PhD with you from our first day of classes through both of our defenses was an honor. Thank you for always being there, for celebrating the successes and for supporting me during the failures. Thank you for growing together with me over the last six years and for being on this journey together to mend hearts.

Last but most importantly, I thank my family for their support over my entire life. To my siblings Kishen and Sarita, thank you for growing up together and for constantly pushing each other to explore and grow. I cannot wait to see what life has in store for us all. To my parents, Margaret and Soumen, thank you for everything you have sacrificed over the years for us kids, I could have not made it to where I am without you. Thank you teaching me that life is an adventure, for raising me to believe that I could achieve anything I put my mind to, and for your unwavering support as I pursue my dreams.

# Table of Contents

## List of Figures

# Chapter 1: Introduction

## 1.1 Myocardial infarction

Heart disease kills around 610,000 Americans every year, accounting for 1 out of every 4 deaths[1]. In 2011, hypertension, heart failure, cardiac hypertrophy, cardiomyopathy, endocarditis, thrombosis, atherosclerosis, valvular regurgitation and stenosis cost the United States $320 billion in healthcare[1]. Myocardial infarctions (MIs), in which a region of the heart loses its blood supply leading to tissue hypoxia, occurs in 735,000 Americans each year, and is the most common source of cardiac scarring [1,2]. MIs are caused by an occlusion of the coronary arteries mediated by the buildup of atherosclerotic plaques within them. Overtime, the buildup of plaque causes narrowing of the arteries and can lead to blockages which disrupt the supply of blood to a region of the heart. After a blockage and subsequent hypoxia occurs, the heart undergoes an injury response which creates fibrotic regions or scar tissue within the cardiac muscle[3–5]. While cardiac remodeling is important to prevent rupture, the excessive deposited extracellular matrix (ECM) can have adverse consequences, as it alters the mechanical and electrical properties of the tissue[6]. Most people who have a MI will survive the initial event[6,7], however the resulting scar leads to disturbed heart function. In the long run this heart dysfunction, ends up being the cause of death for many patients by arrhythmias or heart failure[5,8–10]. The presence of scar tissue leads to both mechanical and electrical consequences[11]. Mechanically the heart has reduced pumping ability, putting stress onto the remaining tissue, and eventually leading to low cardiac output clinically referred to as heart failure. Electrically, the presence of a scar disrupts the normal conduction pathways and leads to electrical disturbances and abnormal heart rhythms known as cardiac arrythmias which can cause sudden death for patients[12–14].

## 1.2 Healthy cardiac tissue

To build an in vitro model of cardiac injury, we first must consider the components and the characteristics of healthy cardiac tissue and their functions, then understand how each of these react to and contribute to injury and progressive scarring. Adult cardiac tissue is composed of different cell types and extracellular matrix (ECM) components arranged in an aligned structure, which together give the tissue unique electrical and mechanical properties to enable it to pump blood around the body's circulation[15,16].

### 1.2.1 Cells within the heart

Cardiac tissue is composed of many cell types: cardiomyocytes (CMs), fibroblasts (FBs), endothelial cells (ECs), pericytes, smooth muscle cells (SMCs), immune cells (myeloid and lymphoid), adipocytes, mesothelial cells and neuronal cells[17,18]. For the scope of this thesis, we will primarily focus on CMs and FBs, and acknowledge the contribution of endothelial and immune cells, which their incorporation into in vitro models remain a large challenge within the field[19,20].

CMs make up the majority of the bulk volume and are the highly metabolic and contractile cells of the heart. CMs are both mechanically and electrically coupled. These cells contain contractile units known as sarcomeres, which are made up of myosin motors and actin filaments. These muscle fibers are organized in larger components known as myofibrils, making up the highly aligned structure of the myocardium. Electrical signals then propagate through these structures to coordinate contraction of the heart chambers and move blood through the circulatory system[21].

CFs, another prominent cell type in the heart, are important in the production, deposition, and maintenance of ECM, cell-cell communication with CMs and endothelial cells, as well as the secretion of various growth factors and cytokines[22]. During injury and

repair processes these cells become activated and are largely responsible to the remodeling processes which occur[23–25].

ECs and immune cells both are important cells in the heart, particularly in the setting of injury and repair[26]. ECs are important for the delivery of oxygen and nutrients to and removal of waste from cells, providing essential barrier function. They also play an important role in signaling pathways interacting with both with CMs and FBs[26,27]. During injury, a large number of immune cells are recruited to the heart, particularly after an acute process such as an MI[26]. These play a large role in the subsequent fibrotic processes[28]. In addition, there is also a significant population of resident immune cells which have important roles in cell-to-cell signaling and maintaining tissue homeostasis[17,29,30].

### 1.2.2 Extracellular matrix

The ECM of cardiac tissue also plays an essential role in the properties of myocardium[16]. It consists of multiple highly-aligned fibril proteins, mainly collagen (type I and III), fibronectin, and elastin, as well as matricellular proteins, matrix metalloproteinases (MMPs), and tissue inhibitors of MMPs (TIMPs)[16,31,32]. These ECM proteins are highly organized; this alignment is essential for the heart structure and function[16,31]. CMs and their surrounding blood vessels, are aligned along these ECM molecules and the orientation is crucial for efficient electrical signal propagation and subsequent contraction[32]. Disturbances to this alignment, for example during scarring, can create disturbances to the usual function of the heart[11].

Alignment also plays an important role in the repair mechanisms of the heart. The anisotropic contraction of the heart affects ECM deposition during healing and scarring and disturbances to the alignment of ECM can affect local mechanical properties[6,11,33]. Many studies have explored the role that ECM alignment has on injury response and repair

mechanism, particularly focusing on its impact on FBs[34,35]. For example, it is known that ECM alignment affects FB migration and the ability of cells to bind and interact to various ECM components[36–40].

### 1.2.3 Electrical Function

The contraction of the heart is coordinated through electrical signals known as action potentials which rapidly propagate through the myocardium. Ion channels in the cell membrane facilitate the rapid flux of ions in and out to create changes in the membrane potential[21]. Between cells, this is mediated through what are known as gap junctions, connexin-43 is one of the most prominent of these gap junctions, sitting at the intercalated discs where cells connect on longitudinally[41]. These junctions enable to rapid passing of action potentials between cells. An action potential is triggered when a certain membrane voltage threshold is reached, this causes a small influx of calcium into the cytoplasm which then rapidly triggers a large calcium release from the sarcoplasmic reticulum. This calcium binds to a protein known as troponin in the contractile apparatus of the cell, changing the configuration to enable binding and in effect triggers contraction[42].

### 1.2.4 Mechanical Function

The mechanical function of the heart is also highly important. Within cells, sarcomeres make up the contractile units of cells and are located between what are known as Z-discs. These sarcomeres make up longer fibers called myofibrils. Once an action potential causes the release of calcium and subsequent binding to troponin, the myosin heads can bind to actin leading to a contraction. The coordination of individual sarcomere shortening and relaxation within and between cells are what lead to the highly coordinated pumping of the heart[42].

## 1.3 Response to injury

### 1.3.1 Generalized wound healing

In general, after injury to a tissue occurs, an immune response is initiated followed by a tissue repair phase. The damage to cell during injury typically causes the release of various inflammatory factors which leads to the recruitment and migration of cells from both the blood and surrounding tissue into the region[43]. Neutrophils and macrophages become activated and migrate into the region to remove debris which resulted from the cell death. These, in turn, recruit fibroblasts to begin producing new ECM, typically a mixture of fibronectin and collagen, to reinforce the region and support new tissue growth. This de novo tissue enables the migration of cells to repopulate and the eventual re-functionalization of the region[44–46].

### 1.3.2 Cardiac injury response

This injury and healing response is also seen within the myocardium after an acute infarct. When a region of the heart loses its supply of oxygen it triggers cell death in that region primarily through a combination of apoptosis and necrosis[47–49]. The cell death and damage trigger an inflammatory and fibrotic response that leads to an influx of immune cells, fibroblasts, and endothelial cells to the region[50]. Together, these cells work to help maintain the structural integrity of the heart and prevent rupture[6,51]. These responses are characterized by increases in various inflammatory cytokines, chemokines, and growth factors. Various pathways are activated including interleukin (IL)-1β, IL-6, tumor necrosis factor (TNF-α), transforming growth factor (TGF-β1), and fibroblast growth factor (FGF)[2]. These factors, alongside other proteins and lipids, activate the immune system, recruiting macrophages and neutrophils to the damaged region to clear dead cells from the injury site.

In turn, this inflammatory activation promotes fibrotic pathways, which lead to the recruitment of CFs and the subsequent ECM remodeling[3,31]. Typically, CFs are not highly proliferative cells. During the healing process, however, some CFs differentiate into myofibroblasts (MyoFs)[52–54]. This transition is mediated by various profibrotic factors that are released by injured resident cardiac cells as well as recruited immune cells. MyoFs are highly proliferative, and express contractile proteins like α-smooth muscle actin (α-SMA). MyoFs are able to contract and remodel their surroundings and produce large amounts of ECM[55,56]. In most tissues of the body, these MyoFs apoptosis after scar formation. However, unlike in typical wound healing, in cardiac tissue, constant hemodynamic stress and mechanical strain reduces this apoptosis[31,57,58]. This can lead to excessive scar formation, where too much ECM becomes deposited, leading to fibrosis and adverse tissue properties. Fibrosis is characterized by an increased collagen content within a tissue that leads to an increase in tissue stiffness; in cardiac tissue, this leads to reduced contractility, ultimately reducing cardiac output leading to heart failure[31,59,60]. In this healing process, ECs are also recruited to begin re-vascularization and restoration of the oxygen supply to the region[61,62].

Unlike FBs and ECs, which can repopulate the infarcted region, adult CMs have very minimal proliferative and migratory capabilities[63–67]. The turnover rate has been reported between 0.3 to 1%[66]. This means that these cells are unable to repopulate the injured region, causing a large heterogeneity within the tissue. The CM volume is replaced by fibroblasts and other cell types, and results in the region becoming dense and scar-like[6,11,26]. Not only does it lack contractile function, which reduces cardiac output, but the tissue is also stiffer, creating more work for the surrounding functional to work against[6,68].

The properties of this tissue are not only dictated by the change in cell populations but also in the alignment of the collagen fibrils which make up the scar tissue which

forms[69,70]. The alignment of the scar tissue varies between more anisotropic versus more isotropic depending on the regional alignment and local stresses it is subjected to during the healing process[11,71]. This alignment, as well as the overall stiffness of the region, has implications for the cells which repopulate the region and is an important consideration when thinking of strategies to re-functionalize the region. The stiffness also affects the surrounding tissue in what is sometimes referred to as the border zone. In this zone, there is increased wall stress caused by myocardial expansion and the CMs contracting against the scar are affected[72,73]. There is evidence that overtime the CMs undergo remodeling and show changes like hypertrophy and altered contraction to attempt to compensate for the nearby loss[68,74].

The shift in cell population and tissue content also alters electrical properties of the tissue. The injured region fails to repopulate with CMs and therefore has reduced or completely lacks electrical conductive properties[75,76]. There is evidence of abnormal connexin junction localization leading to electrical coupling between CMs, FBs, and MyoFs[77,78]; this can lead to unsynchronized electrical signals. Additionally, the scar region's increased amounts of ECM also lead it to act as an insulator[24,79], reducing conductivity of the electrical signal across the myocardium which can also cause dyssynchronization leading to reentry arrhythmias and sudden death [2,58,80].

### 1.3.3 Long term consequences of cardiac scarring

The presence of this scar leads to reduced cardiac output. Over time with this reduced output, the heart is unable to keep up with the demands of the body for pumping blood. This inadequate pumping leads to fluid back up into the lungs and the rest of the body, a condition known as congestive heart failure[81]. Heart failure causes many symptoms in patients, including shortness of breath, edema, and fatigue. The long-term stress on the

heart also paves the way for electrical abnormalities, leading these patients to have a higher incidence of arrhythmias and sudden cardiac death[76,80].

### 1.3.4 Challenges in re-functionalization of the myocardium

These long-term consequences have led to the exploration of many strategies aimed at regaining cardiac function in the recent years. Most of these studies have been performed in vivo animal models. The studies range from the simple delivery of factors to promote CM regeneration or reduce fibrosis, for example follistatin-like 1[82] and various microRNAs[83–85], to more complex strategies such as systemic and localized delivery of stem cells[86,87] or stem cell factors[88]. Patches are also being developed which either simply provide mechanical reinforcement or composed of cardiac cells[89–92] grown in vitro then applied to the epicardial surface. Unfortunately, a lot of these studies fail on the way to clinical application because in vivo success in animal models does not always yield success in humans[86,93]. The causes of these failures are still not well understood, therefore identification of the ways in which these therapies fail and solutions to these challenges would provide improvements to clinical efficacy.

## 1.4 In vivo models

Current information about injury and fibrosis response in the heart is primarily derived from the study of various animal models. These models include studies in both rodents, including mouse and rat models, and larger animals, including dogs, sheep, pigs, non-human primates. A majority of studies have been performed in rodent models due to simplicity and the ability to breed various genetically altered lines. In many ways, rodent models have been key in identifying majority of the pathways involved in the injury responses. However, the heart tissues of these animals have significantly different electrophysiological properties and different molecular structures[94,95]. For

example, a mouse heart beats approximately 8x as fast as a human heart. The primary myosins (α and β) in mice are also reversed compared to humans[96]. Of high relevance to this thesis is the much higher regenerative capacity that rodent hearts also have compared to that of human hearts[88]. Due to these differences, there are a lot of challenges when attempting to translate findings in rodent models to clinical applications[97–99]. Though many proteins and pathways have been identified to play roles in fibrosis and remodeling in the heart, the poor translation to clinics means there is a strong need for systems which better represent human to investigate these potential therapies. Due to this, larger animal models are often used since their physiological parameters are closer to those of humans[98,99]. Their use is limited, though, due to high costs and impracticalities of large sample sizes. Therefore, these systems are not ideal for high throughput experimentation. This, in combination with the poor representation of human physiology from rodents, creates a space for the development of in vitro platforms which are equipped to probe cardiac injury within a human context.

## 1.5 In vitro models

In order to study cardiovascular function at a cellular level, studies have also employed the use of in vitro models. These types of models enable much more control compared to in vivo systems, and enable the isolation of components (cells, ECM, molecules) to be able to study direct effects while minimizing complexities from an entire living system which can confound our understanding.

### 1.5.1 Cell sources

Due to the non-regenerative characteristic of cardiomyocytes, in vitro studies are challenging as these cells are unable to proliferate[63–67]. Therefore, to study CMs in vitro, cells must be freshly isolated, typically from rodents, and can only be maintained in culture

on the scale of days for neonatal isolates and just hours for adult isolates. For these reasons, the study of human cardiac cells was especially limited until the advent of stem cell technologies. Since the development of stem cell technologies, various protocols have been developed and optimized to differentiate both embryonic stem cells and induced pluripotent stem cells efficiently into CMs[100,101]. These advances enabling the study of human CMs have created multiple new fields of study. The disadvantages of these cells are that they are still in a relatively immature or neonatal-like stage compared to adult CMs, particularly in 2D culture[102,103]. This is an important consideration when using these cells as models.

### 1.5.2 Engineered Heart Tissues

To enable the study of these cells within a tissue context, there has been a rapidly growing field of engineered heart tissues (EHTs) where these iPSC-derived CMs are combined with other stromal populations, such as MSCs or fibroblasts, and placed within a hydrogel matrix[104–107]. This enables the formation of functional tissues and thus the study of CMs within the context of both surrounding ECM as well as various cell-cell interactions. These tissues are being investigated for multiple uses including disease modeling and tissue replacements. Over the last 10 years, these models have developed and enabled us to study various important functions of cardiac tissue including force dynamics, electrical signaling, and calcium handling[104,106,108,109]. In particular, the ability to study the response of CMs under the context of both fibroblasts and ECM remodeling is important when looking to model cardiac injury and healing.

One large challenge that remains in the field is vascularization of these EHTs[19]. The incorporation of endothelial cells into these tissues and their formation into functional vasculature is important particularly to support nutrient and oxygen demands as these

tissues are scaled larger for implantation[19,110]. As previously mentioned, these cells also have an important role post-MI in the re-functionalization of the infarcted region. After the initial injury response, endothelial cells are some of the first cells to migrate into the region, building new capillaries to support the tissue regrowth and providing signaling for surrounding cells[27,62,111]. In the engineered heart tissue (EHT) field, one of the largest challenges has been determining the correct in vitro conditions that can support both CM and endothelial vasculature together[110]. With many unknowns including the optimal cell sources, culture medium, and necessary local cell signaling which enables the co-habitation of these cell types.

### 1.5.3 In vitro injury models

The field of EHTs is rapidly developing[96,112–115]. Since the development of reliable protocols to differentiate iPSCs into CMs[116], massive strides have been made in using these cells to create functional tissues for a variety of applications, from in vitro mechanistic, drug efficacy, and drug safety studies to in vivo implantations on ischemic hearts. There have been a few studies which have used these EHTs to study the effect of hypoxia, reperfusion injury, and fibrosis[117–122]. Hypoxia studies, however, are limited in that they require the entire tissue to be subjected to a hypoxic environment[123,124]. In this manner, they are unable to capture how regions of injured tissue are interacting with adjacent healthy regions, and how the coupling of an injured region affects the function of this neighboring healthy tissue. A similar limitation arises with models systems which induce a fibrotic phenotype by adding a fibrosis-inducing factor like TGFβ1 to the culture system[125–127]. Other models which have achieved this injured-healthy coupling, fuse together a healthy population with a scar-like population which is modeled by an increased fibroblast population[128,129]. While this enables the study of interactions between the two regions, these models do not recapitulate the cell

death element of ischemia, nor do they enable the study of the evolution of damaged and surrounding regions as the tissue remodels to compensates for the acute damage. One organoid model successfully induced region hypoxia through stimulation of norepinephrine and showed it could recapitulate hallmarks of MI including various infarct zones and a fibrotic response[130].

### 1.6 Overview of Thesis

The work throughout this thesis looks to address the need for better models and techniques to study the response that occurs after cardiac injury with the long-term goal to enable the development of new therapies to treat and improve heart function. Utilizing human cells in highly tunable environments enables the modeling of specific human biological process to identify translatable mechanisms and pathways for therapy development. In this work, we show the development of human, cell based, in vitro models of cardiac injury and tools to enable the functional analysis of these systems. We then demonstrate the utility of such models to recapitulate disease processes and probe biological questions within the cardiac repair field.

In Chapter 2, we show the development of an EHT cardiac injury model which uses targeted damage from a high-powered laser to create regional cell death within an EHT. This regional damage enables the in vitro study of both the injured tissue response, but also the surrounding healthy tissue, like what is found within the border zone in vivo. The focus of the chapter is on the electrical and mechanical functional assessments of different zones within these EHTs following injury and their recovery response, demonstrating the ability to study the functional changes which occur over time post-MIT in such models and the potential for use as a system to test new interventions.

Next, in Chapter 3, we explored the development of better technologies to study the electrical properties of heart function. Most EHT models that look at the electrical function of EHTs utilize calcium dyes and sensors as proxies for APs, however APs carry important information of importance to many disease processes. Therefore, we explored to utility of a recent genetically encoded voltage sensor developed in the neuroscience field and adapted it for use within iPSC-CMs and EHTs[131]. This sensor has the advantage over prior sensors of fast kinetics, high signal-to-noise, and repeatability due to no toxicity.

In Chapter 4, we focus in on the injury response driven solely by the fibroblasts in tissues. As myocardial tissue is highly aligned, we investigate the role that such alignment has on the early healing stage of provisional matrix synthesis, an important process which lays the foundation for new cells to invade a damaged tissue. Using a similar engineered tissue model, we study fibroblasts' response to injury and the effect on provisional matrix building of fibroblasts from isotropic and anisotropic tissues[132].

Finally, Chapter 5 contains a compilation of early-stage projects which looks to address some of the challenges within the EHT and cardiac regeneration field. It includes work that studies the genetic profile of cells within EHTs over time, the incorporation of endothelial cells into EHTs and their assembly into vascular networks for the future purpose of perturbing cell-cell interactions and the scale up and implantation of EHTs, and finally, brief work demonstrating the use of EHT to study questions for the optimization of CM engraftment.

# Chapter 2: Mechanical adaptation of cardiomyocytes in response to acute localized injury in engineered heart tissues

The work in the chapter shows the development of a cardiac injury model using EHTs. Using local injury via a high-powered laser, we are able to capture the acute effects of injury and repair of a damaged region and study the functional changes within that region and in adjacent regions of tissue.

## 2.1 Introduction

Myocardial scarring, caused by acute insult to the tissue but also caused long term by genetic or disease cardiac pathologies, creates disturbances to heart function[6,11,26]. Myocardial infarctions account for the majority of myocardial scarring[133]. After an ischemic event, the affected region undergoes a focal fibrotic response leading to heterogeneity within the myocardium – a fibrotic-scarred region surrounded by healthy myocardium[4,5,11,134]. While the presence of this scar is important for preventing rupture[6,11,51], the excessive ECM alters the mechanical and electrical properties of this tissue, not only affecting function of the region but also the surrounding myocardium and overall heart function[6,81]. Regions directly adjacent to the scar experience what is known as non-ischemic infarct expansion, wherein the scar region is stretched and enlarges due to collagen degradation and causes increased stresses in the edge of the tissue region[68,72,73]. Regions more distally adjacent are known to undergo hypertrophy[68,135,136], and over time become thinner and dilated contributing in the long-term to heart failure[8,9,81,137].

The emergence and advancement of human engineered heart tissues (EHTs) in the last decade provide an ideal system to study cardiac fibrotic processes under the human context given the highly controlled environments and ability to model both mechanical and electrical properties

of heart tissue[104–106,108,138,139]. The 3D nature of these tissue models enables the incorporation of ECM and ability to study tissue remodeling, an important process in injury and healing. To date, several EHT models which have studied cardiac injury or fibrosis have been reported[59,120,124–130,138–140]. Models which induce cell death via hypoxia[124,130,138,139], enable the study of acute cell death and reperfusion injury are limited to study of the injury region as the whole tissue is generally subjected the hypoxia. Other models demonstrate cardiac fibrosis by the addition of factors such as TGF-β1[120,125–127,141], or induce fibrosis and even focal fibrosis through modulation of cell populations[128,129]; however, these do not capture the acute response to the cell death and local function loss as seen during an MI and cannot model how this damage affects the surrounding tissue.

Here we present a model for myocardial injury which uses a high-power pulsed laser to regionally damage an EHT. This results in an injured region within the center of the tissue where the surrounding myocardium maintains its function, enabling the study of both the effect of acute cell death of a region and its progression into fibrosis and the effect this has on the surrounding tissue.

## 2.2 Material and Methods

### 2.2.1 Cell Source

A previously reported hiPSC line derived from the Personal Genome Project (PGP1) containing fluorescently tagged GFP the Z-disc protein titin (TTN-GFP) were used for these studies[142]. Adult human ventricular cardiac fibroblasts (Cell Applications) were from a 26-year-old male.

### 2.2.2 Cell Preparation and Culture

iPSCs were maintained in complete mTeSR1 medium (Stem Cell) and differentiated into monolayers following small molecule protocol[100]. Briefly, cells were differentiated using RPMI 1640 Medium, GlutaMAX (Gibco) supplemented with B-27 Supplement, minus insulin (Gibco).12 μM CHIR99021 (Tocris) was added for 24 hours on Day 0 of differentiation, then 5 μM IWP4 (Tocris) was added for Days 2 and 3. On Day 9, cells were switched to RPMI 1640 Medium, GlutaMAX containing standard B-27 Supplement (Gibco). After two days, CMs were metabolically selected using glucose free, RPMI 1640 Medium (Gibco) supplemented with 4mM of DL-lactate (Sigma) for four days. Following selection, CMs were replated onto fibronectin (10 μg/ml; Corning) coated plates and maintained in RPMI 1640, supplemented with B-27. CMs were used within 7 days of re-plating. Cardiac fibroblasts were maintained in HCF Growth Medium (Cell Applications) and used at Passage 4.

### 2.2.3 Microtissue Seeding

Polydimethylsiloxane (PDMS) microtissue devices with wells containing two cylindrical micropillars with spherical caps were cast from 3D printed molds (Protolabs). Two days prior to seeding, devices were plasma-treated for 60 s, treated for 2 hours with 0.01% poly-L-lysine (ScienCell), then for 15 min with 0.1% glutaraldehyde (EMS). PDMS devices were then washed and then soaked in DI water at 4°C until use. Before seeding, devices were briefly soaked in 70% ethanol, dried, then sterilized under ultraviolet for 15 min. Then to prevent cell attachment to bottom of wells, wells were treated with 2% Pluronic F-127 (Sigma) for 30 min, then dried.

To make each tissue, 60,000 cells (90% iPSC-CMs and 10% human cardiac fibroblasts) suspended in 7.5 μl of an ECM solution consisting of human fibrinogen (4

mg/ml; Sigma-Aldrich), 10% Matrigel (Corning), 0.4 U of thrombin (Sigma-Aldrich) per mg of fibrinogen, 5 μM Y-27632 (Tocris), and aprotinin (0.033 mg/ml; Sigma-Aldrich) were added to each well. After allowing for gel polymerization for 10 minutes, tissue maintenance medium containing high-glucose Dulbecco's modified Eagle's medium (Thermo Fisher Scientific) supplemented with 10% fetal bovine serum (Sigma-Aldrich), 1% penicillin-streptomycin (Thermo Fisher Scientific), 1% nonessential amino acids (Thermo Fisher Scientific), 1% GlutaMAX (Thermo Fisher Scientific), 5 μM Y-27632, and aprotinin (0.033 mg/ml) was added. After 2 days, Y-27632 was removed, and after 7 days the aprotinin concentration was decreased to 0.016 mg/ml.

### 2.2.4 Laser injury

After seven days of tissue formation, tissues were damaged using a 1064 nm Pulsed Nd:YAG Laser (Minilite, Continuum). 12 pulses at 1 mJ were delivered in a 3 x 4 grid pattern to the center region of each microtissue.

### 2.2.5 Apoptosis Staining and Confocal Microscopy

One hour after laser injury, microtissues were stained with Apoptosis/Necrosis Assay Kit (abcam) following the manufacturer's protocol. Samples were then fixed in 4% paraformaldehyde for 20 minutes washed x3 in PBS. Prior to imaging, samples were stained with 1:1000 DAPI for 1 hour at RT. Z-stacks of samples were imaged on a Leica SP8 confocal microscope with a Leica 25x water objective and Leica LAS X imaging software. For DAPI analysis, 150μm by 250 μm regions in the center of the tissue were taken of the maximum projections of acquired stacks, then the median intensity value in the these was measured.

### 2.2.6 Sarcomere Analysis

In this code, we segment "myofibril-like" structures from fluorescent z-stack images. A 150 μm x 250 μm region of interest in the center of stacks was selected to represent injury region. Then for each slice, Laplacian filter was applied to detect the steep gradient in brightness found at the edges of the myofibrils[143]. Then a multi-dimensional Gaussian filter with a standard deviation of 2 was applied to the resulting Laplacian filtered image[144], followed by the application of a Otsu threshold[145]. Speckle noise (present in a small subset of images) was then removed by multiplying the resulting binary image by a binary mask created by applying an Otsu threshold to the original image after a median filter with size 3 is applied[144]. The resulting segmented region in the binary image were identified using the scikit-image "regionprops" function[145]. To reduce noise and select for fibril structures, minimum segment length of 6 μm was implemented and all segmented regions with a major axis length longer than 6 microns were saved and the total length summed.

### 2.2.7 Mechanical Property Characterization

The mechanical properties of the tissues were characterized using nanoindentation (Piuma, Optics 1l) equipped with a probe (Piuma) possessing a 55 μm bead diameter and a spring constant of 0.18 $Nm^{-1}$. The Young's Modulus was averaged from at least four indentations at the center of each tissue that were averaged for each individual sample (n = 2, 3, or 4) for each of four experimental repeats. Curves were fitted to a Hertz contact model fitted to the loading curve assuming a Poisson ratio of 0.5. All measurements were taken with tissues submerged in tissue maintenance medium and performed on Day 0 after injury and on Day 7.

### 2.2.8 Calcium Imaging

Immediately after injury (Day 0) and on Day 7 after injury, Rhod-3 Calcium Imaging Kit (Invitrogen) was applied to injured and control tissues according to the manufacturer's protocol. Briefly, microtissues were incubated with dye solution at RT for 45 minutes, washed and incubated another 45 minutes at RT to allow for ester cleavage. Samples were imaged in Tyrode's Salts with sodium bicarbonate (Sigma). Time-lapse videos of the microtissue's spontaneous contractions were acquired at either 30 or 15 frames per second, depending on the imaging day on a Nikon Eclipse Ti with a 4x objective with an Evolve EMCCD Camera under both temperature and CO2 control.

### 2.2.9 Force Measurements

Time-lapse videos of the microtissue's spontaneous contractions were taken before laser injury, 30 minutes after laser injury, and then subsequently on Days 1, 3, 5, and 7 post-injury to quantify changes in force over time. Videos were acquired at 30 frames per second on a Nikon Eclipse Ti (Nixon Instrument's, Inc.) with a 4x objective with an Evolve EMCCD Camera (Photometrics). Microscope was equipped with a temperature and CO2 equilibrated environmental chamber.

Maximum contractile force, stress, and contraction kinetics were calculated using a custom Matlab Script based on the deflection of the pillars and the measured pillar spring constant of 2.68 μN/μm, as described previously[146].

### 2.2.10 Strain Analysis

In this code, we compute the average strain in manually defined regions of interest (ROIs) in timelapse images (as described in Section 2.3.9) of microtissues. A center region ROI (299 μm x 199 μm) and an adjacent region ROI (139 μm x 299 μm) were selected for each tissue. Then the original 16-bit channel TIFF image was converted to an 8-bit single

channel image where the maximum and minimum brightness found in the defined ROIs is used for scaling[145,147]. Then Shi-Tomasi corner points in both ROIs were detected[143,148], and tracked using the iterative Lucas-Kanade method with pyramids[143,149]. The absolute displacement of all corner points in each frame was computer and the absolute displacement peaks were detected with the scipy "signal.find_peaks" algorithm[144]. Temporal reference points were defined as all points half way between each peak. For n peaks, there was n-1 temporal reference points, and then n-2 temporal periods between these temporal reference points to consider. The strains were then computed with respect to frame number in each temporal reference period. For each temporal reference period, the center and edge ROIs were treated separately and re-compute the Shi-Tomasi corner points were re-computed and tracking was performed for the duration of the temporal period. Then, for each ROI and temporal period we used the change in position of each corner point to compute the average deformation gradient of the ROI with respect to frame number[150]. Then, the average deformation gradient was transformed into the Green-Lagrange strain tensor and the maximum strain in the xx direction (defined by the axis connecting the two microtissue posts, maximum refers to maximum magnitude as contractile strain will be negative) was computed. For each timelapse image, the final output is then the maximum contractile strain in the xx direction ($E_{xx}$) averaged over all temporal periods detected in the timelapse for both the center and edge ROIs.

### 2.2.11 Statistical Analysis

Graphpad Prism 9 was used to perform all statistical analysis. A two-way ANOVA statistical test was used to determine significance for multiple repeat experiments across conditions with the exception of Figure 2b,c where a Student's t-test was used. Across all figures: *: $p < 0.05$, **: $p < 0.01$, ***: $p < 0.001$, ****: $p < 0.0001$.

## 2.3 Results

### 2.3.1 Injury to engineered cardiac engineered tissues leads to regional cell death

A myocardial infarction (MI) causes cell death to a region of the heart, this cell death is responsible for a fibrotic response which results a region of tissue that has a different cellular composition as well as different mechanical and electrical properties compared to the rest of the myocardium[6,11,26,47–49]. To capture this phenomenon, we sought to develop a platform which could target injury to a region of an engineered heart tissue (EHT) to enable to study of such an insult on the region and on adjacent tissue. We used two different methods to create such an injury. First, we used a small microdissection knife to cut a hole in the center of the tissue. Due to the nature of fibroblasts, these cells spontaneously migrated to close the gap. The cardiomyocytes however, as non-migratory cells did not move into this region. The result was a region within the center of the tissue which was populated with fibroblasts but not cardiomyocytes (Figure 2.S1). This was visualized by using GFP-tagged fibroblasts and staining for α-actinin to mark cardiomyocytes. Since this type of full thickness wound is rare in the heart, we wanted to explore alternative methods to lead to cell death without disrupting the integrity throughout the tissue.

Lasers have been demonstrated in medical applications for the ablation of various tissues types[151–156]. Laser light is highly tunable and has a high degree of spatial control, making it an ideal tool to deliver highly-targeted regional cell damage to EHTs. Lasers cause damage to tissues via a few mechanisms, two of which are 1) photothermal where damage is caused from absorbed laser energy which causes heat generation and vaporization of tissue and 2) photodisruption where the rapid exposure to the high energy of the laser causes rapid expansion of water molecules leading to a mechanical disruption and ablation of tissue[155,157]. The advantage of this method is it minimizes thermal damage to surrounding

tissue. The mechanism by which lasers lead to ablation has been shown to be dependent on their wavelength. Lower wavelength of laser such as 532 nm ablation occurs more through photothermal ablation, while a 1064 nm wavelength was demonstrated to ablate through the photodisruptive mechanism[151]. To minimize heat damage we used a 1064 nm nanosecond pulsed laser to damage our EHTs. To do this, EHTs were seeded from a combination of human induced pluripotent stem cell-derived cardiomyocytes with GFP-tagged titin (CMs) and primary human cardiac fibroblasts (CFs). Then after allowing tissue to form for 7 days, EHTs were regionally damaged to induce cell death using a Nd:YAG nanosecond pulsed laser (Figure 1a).

To avoid tissue ablation, the energy of the laser pulse was set to 1.0 mJ to cause cell death without creating a full thickness hole in the microtissue (Figure 1a). As indicated in Figure 1a, laser injury was targeted to center region of tissue to create injury to only a portion of the tissue. After an MI, cells die from a combination of apoptotic and necrotic processes[47–49]. To characterize the cell death caused by the laser, tissue samples were fixed 2 hours after injury and stained for markers of both apoptosis and necrosis, phosphatidylserine and DCS1, respectively (Figure 1b). While there was a baseline level of both apoptosis and necrosis in the uninjured controls, there was a significant increase in both of these markers in the injured conditions (Figure 1c, d). In particular, this cell death was seen directly within the injury region and more diffusely in adjacent tissue, thus demonstrating that laser ablation could be used to regionally induce cell death as observed in acute heart injury. It was interesting to observe that the damage caused by the laser was less controlled than expected. While injured tissues consistently showed damage, there was some variation between tissues for the total amount as well as the distribution of the damage. For example, damage was not only found in the targeted laser zone but there was also diffuse damage in

surrounding regions. This diffuse may have been caused by heat damage effects from the laser which affected neighboring tissue, or by the release of reactive oxygen species triggered by the laser. Alternatively, the cell death in these regions may have been caused from paracrine signaling from the directly damaged regions leading to the activation of inflammatory and cell death pathways more distally. Differences in total damage were likely due to user control of z-plane for the laser and variations in thickness of the PDMS base of which the laser had to pass through.

To visualize how the laser affected cell number in injured tissue, nuclei were stained and imaged (Figure 1e). This revealed the loss of overall nuclei in the region of the laser ablation as well as the presence of pyknotic nuclei in the injured condition (Figure 1e, f). As a characteristic of cardiac injury is the loss of mechanical function to the damaged region of the heart, we wanted to specifically look at the effect of laser induced injury on CMs. Therefore, the GFP tagged sarcomeres of the CMs were imaged and total myofibril length in the center region was measured (Figure 1e). In injured regions of the tissues there was significant loss of myofibrils as well as some loss more diffusely to the edges, while in the non-injured tissues there were aligned myofibrils throughout (Figure 1g). Overall, this shows that a laser can be utilized to regionally induce cell death via both apoptosis and necrosis within an EHT, creating regional loss of sarcomere structures.

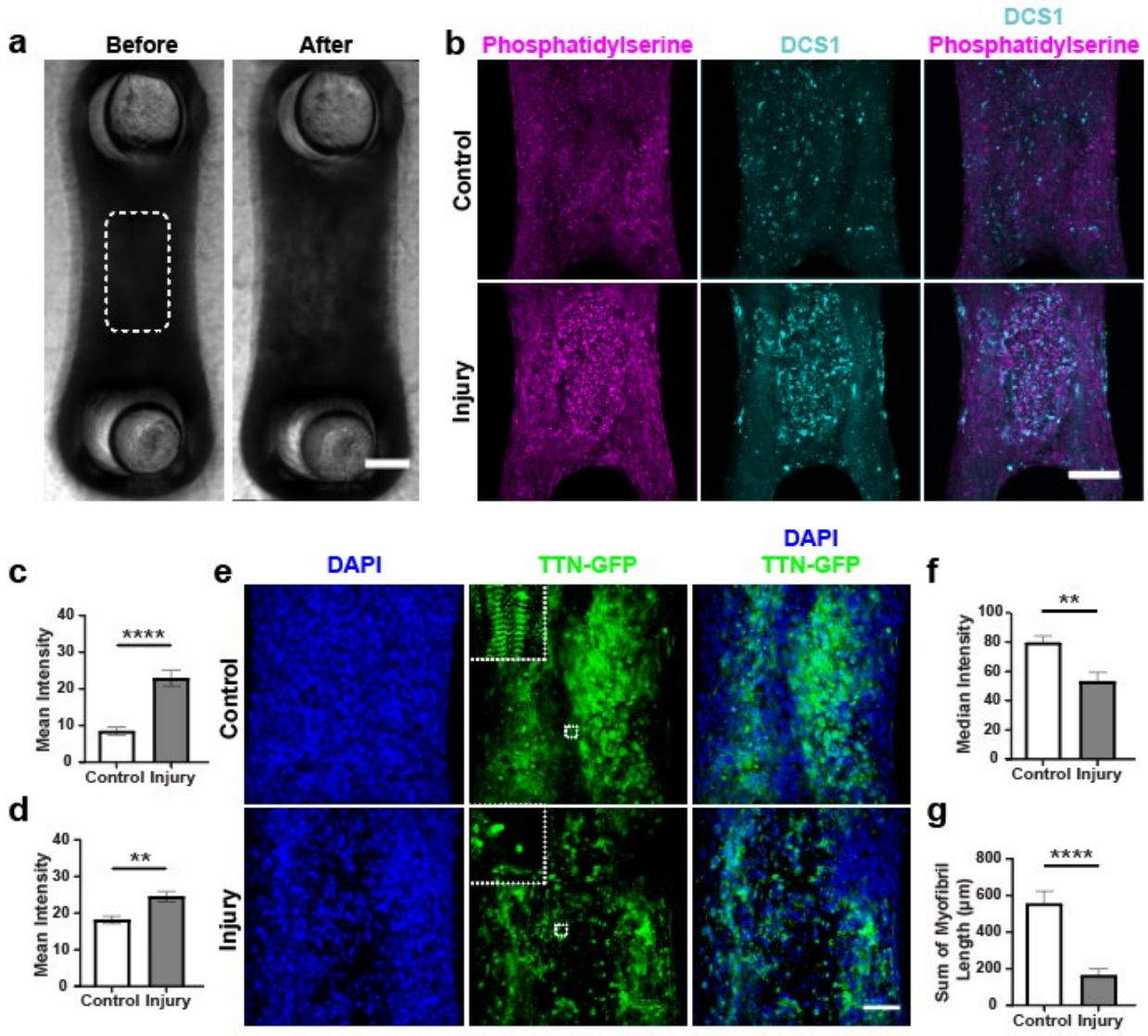


**Figure 2.1 Laser injury to engineered cardiac engineered tissues leads to regional cell death.** **a)** Brightfield images of engineered heart tissue (EHT) seven days post-seeding before (left) and after (right) laser ablation. White dashed box indicates region of targeted laser injury. Scale bar = 200 µm. **b)** Maximum projections of fluorescence images for phosphatidylserine (apoptosis, magenta), and DCS1 (necrosis, cyan) of control (top) and injury (bottom) conditions 2 hours after injury. Scale bar = 200 µm. **c)** Mean intensity of phosphatidylserine of z-stacks in center region of tissues, ****: $p < 0.0001$, n = 18,19. **d)** Mean intensity of DCS1 of z-stacks in center region of tissues, **: $p < 0.01$, n = 18,19. **e)** Maximum projections of fluorescence imaging of DAPI (blue) and TTN-GFP (green) of control (top) and injury (bottom) tissues 2 hours after injury. Insets indicated by white dashed boxes are 25 µm x 25 µm. Scale bar = 100 µm. **f)** Median intensity of DAPI of z-stacks in center region of tissues, **: $p < 0.01$, n = 14,15. **g)** Average of sum of myofibril length over slices from z-stacks of center region of tissues, ****: $p < 0.0001$, n = 13,15. Bar plots represent means and error bars represent SEM.

### 2.3.2 Injured tissues demonstrate focal fibrosis and have increased ECM production over time

After a hypoxic event to the heart, the tissue undergoes an inflammatory and fibrotic process which leads to a change in the cell composition and ECM. Due to the inability of CMs to migrate and repopulation the region, the population of the region shifts towards fibroblasts[5,11,25,26]. Additionally, the fibrotic response leads to the increased deposition of extracellular matrix such as fibronectin and collagen type I[6,11,26]. To characterize the response over time within this system, EHTs were fixed 7 days after injury and immunofluorescence staining of vimentin and fibronectin was done to characterize the fibroblast and ECM responses, respectively. Vimentin staining showed a region in the injury targeted area void of CMs but with high vimentin expression, indicative of a scar-like region (Figure 1a). Overall within the injury zone of the tissue there was a significant 8x fold increase in vimentin expression. (Figure 2b). To evaluate increases in ECM deposition, fibronectin was stained for and showed a significant 4x increase from the injury to control, with much of the fibronectin co-localizing with vimentin (Figure 2a, c). Together, these data indicate that the laser injury is causing an activation of fibroblasts, particularly in the region of the injury leading to increased ECM like that is seen in replacement fibrosis which occurs in vivo.

Another hallmark of scar tissue post-MI is an increase in stiffness[31,60,70]. Therefore, to understand if the increased ECM production affected the mechanical properties of the tissue, we measured the Young's modulus in the injured region of the tissue. First, to ensure the laser injury was not affecting the mechanical property of the tissue, the stiffness was measured in tissues both after the injury (Day 0), and 7 days later (Figure 2d). After injury, both tissues had similar stiffnesses of 1.4 ± 0.1 kPa (mean ± SEM) and 1.4 ± 0.1 kPa (mean ±

SEM) for control and injury, respectively. At Day 7, while not significant different ($p$ = 0.0795), the stiffness in the injured tissues does trend higher than the control, 2.6 ± 0.2 kPa (mean ± SEM) to 2.2 ± 0.1 kPa (mean ± SEM). But comparing both conditions demonstrated significant increases in stiffness from Day 0 to Day 7.This data shows that over time the laser injury can induce aspects of replacement fibrosis in an EHT.

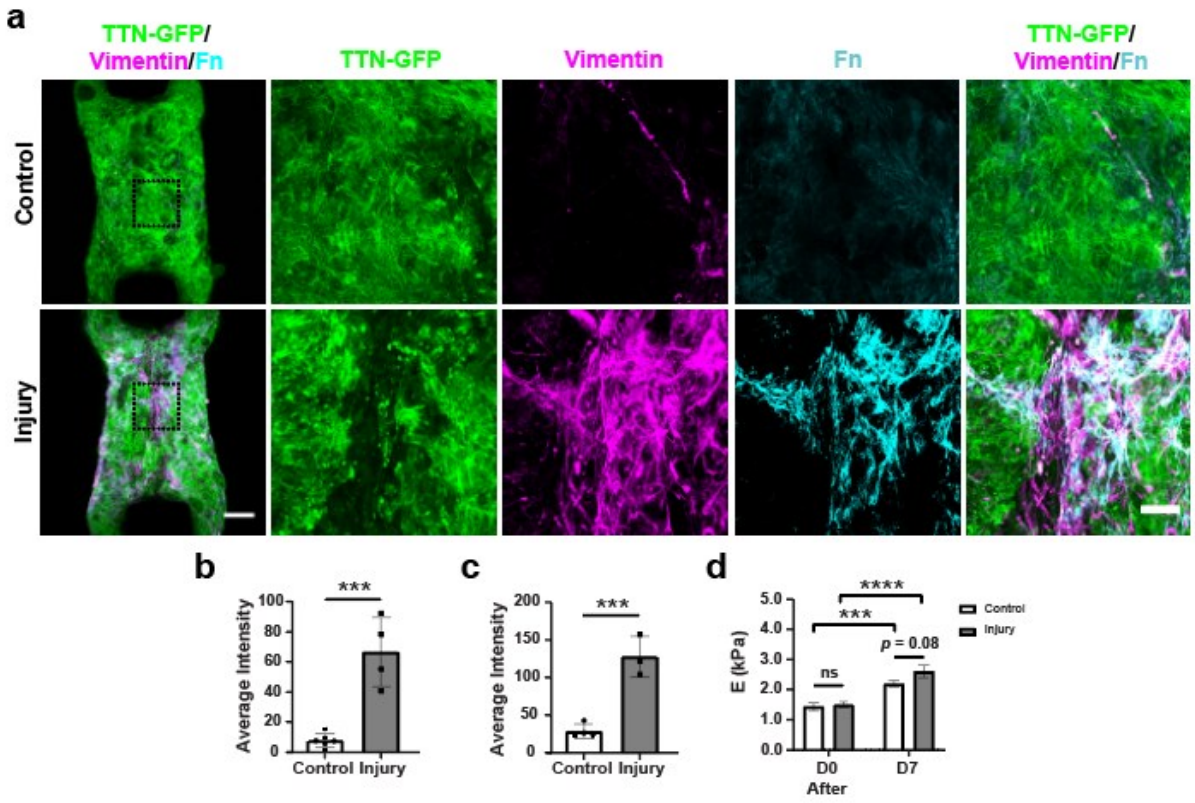


**Figure 2.2 Injured tissues demonstrate focal fibrosis and have increased ECM production over time. a)** Maximum projections of EHT on Day 7 post-injury with TTN-GFP (green), vimentin (magenta), and fibronectin (cyan); low magnification (left), scale bar = 200 μm, black dashed boxes indicate corresponding high magnification images (right), scale bar = 50 μm. **b)** Mean intensity of vimentin for sum of z-stacks in center region of tissues, ***: $p < 0.001$, n = 6, 4. Bar plots represent means and error bars represent SD. **c)** Mean intensity of fibronectin for sum of z-stacks in center region of tissues, ***: $p < 0.001$, n = 4, 3. Bar plots represent means and error bars represent SD. **d)** Young's modulus measured in the center region of the tissue at Day 0 after injury and Day 7 after injury, ***: $p < 0.001$, ****: $p < 0.0001$, n = 9-11. Bar plots represent means and error bars represent SEM.

### 2.3.3 Electrical function is regained in adjacent tissue but not in the region of injury

As CMs are the primary conductors of electrical signals through the myocardium, the loss of CMs after an MI also changes the electrical properties of the region. The affected region becomes electrically inactive, acting as an insulator[24,79]. This is an important characteristic clinically as the presence of such tissue can lead to electrical disturbances and

arrhythmias[11,58,80]. Therefore, after observing the loss of CMs and changes to the center region of the tissue, we evaluated the affect the injury had on the electrical activity of the tissue. To do this, Rhod-3 dye was used and the calcium dynamics were measured in the region of injury and in the adjacent tissue to determine how the electrical activity was affected both locally and more distantly (Videos 2.S1-2.S4). After the injury, at Day 0, there were reduced calcium dynamics in both the center and adjacent regions compared to the control tissue (Figure 3b,c). While the dynamics in the center of injury, decreased by 69 ± 8% (mean ± SEM) to the control, the adjacent region while still significantly decreased, was reduced by only 49 ± 10% (mean ± SEM). This shows that while the injury had the largest effect directly on the region of injury, the electrical activity was still affected in neighboring regions.

To understand if this effect lasted long-term, calcium dynamics were measured again in the same regions in tissues at Day 7 post-injury. While the dynamics in the control and in the center of the injury was overall unchanged from the Day 0 measurements, the adjacent region of the injured condition regained calcium dynamics similar to that of the control (Figure 3d,e). This is interesting as it indicates that after the initial injury there is a transient effect on the injured tissue as a whole, but over time the adjacent regions, which we have shown still have cardiomyocytes, have regained normal electrical function, while the injured region fails to recover. This lack of recovery of electrical activity in the region is like that seen in in vivo scar regions where there it can cause arrhythmias.

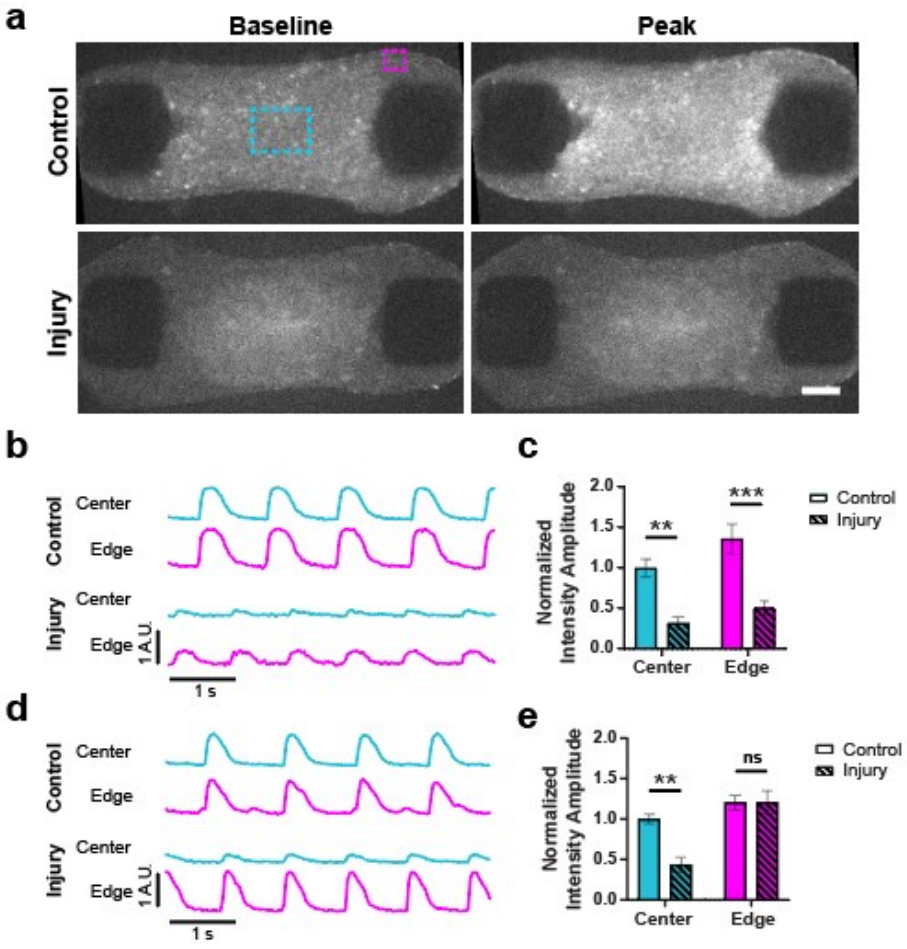


**Figure 2.3 Electrical function is regained in adjacent tissue but not in the region of injury**
**a)** Widefield fluorescence images of control (top) and injured (bottom) EHTs stained with Rhod-3 Calcium Dye 2 hours post-injury showing baseline (left) and peak (right) signal. Dashed boxes indicate regions of interest for traces and analysis in Figure 3b, c, d, e. Center region (cyan), and edge region (magenta). Scale bar = 200 μm. **b)** Example traces for a control and an injury tissue at Day 0 after injury in center (cyan) and edge (magenta) regions indicated in Figure 1a. All traces are normalized to control center region trace. **c)** Normalized intensity amplitudes for traces at Day 0 after injury. Normalized to control center region, **: $p < 0.01$, ***: $p < 0.001$, n = 9-10. **b)** Example traces for a control and an injury tissue at Day 7 after injury in center (cyan) and edge (magenta) regions indicated in Figure 1a. All traces are normalized to control center region trace. **c)** Normalized intensity amplitudes for traces at Day 7 after injury. Normalized to control center region, **: $p < 0.01$, n = 10. Bar plots represent means and error bars represent SEM.

### 2.3.4 Force recovery over time corresponds with increased contraction in regions adjacent to injury

In addition to causing electrical disturbances, the injury and scarring response also changes the mechanical properties of the region, leading it become stiffer and lose its contractile ability[6,11]. These changes are known to have important consequences for overall cardiac contractility[70,81]; therefore, we evaluated the changes in contractile function in this model from the laser-induced injury (Videos 2.S5-2.S8). To do this, the twitch force generation was measured by tracking the deflection of the flexible pillars microtissues are attached to. These measurements showed that injury to the tissues caused a 39 ± 3% (mean ± SEM) reduction in total force generation compared to the baseline (Figure 4a). Twitch force for the same tissues was then tracked over the next 7 days (Videos 2.S9, 2.S10). While in the controls the force generation remained close to baseline, over time the twitch force of the injured tissues increased, returning close to the baseline level for these tissues (Figure 4a).

In vivo studies of the mechanics of scar tissue in the heart show that not only does the scar region stop contracting, but it also begins to be cyclically stretched. This stretching phenomenon negatively impacts overall pumping function[158]. Since we show we are able to recapitulate a similar heterogeneity within the tissue, we wanted to more closely investigate the mechanics of the scar-like and adjacent tissue over time. To do this, $E_{xx}$ strain was measured in the directly injured region as well as the adjacent tissue before injury, after injury, and at Day 7 post-injury (Figure 4b). Before injury, the center of the region had average strains of -1.4 ± 0.2%, similar to the -1.9 ± 0.4% (mean ± SEM) of the control. After injury, this region lost its contraction and rather began to be stretched indicated by a switch to a strain of +0.6 ± 0.2% (mean ± SEM), compared to the control which maintained a strain

of -1.4 ± 0.4% (Figure 4c, d). This lack of contraction was also present through Day 7 (+0.02 ± 0.4%) (mean ± SEM), indicating this region does not regain contractile function and therefore is not contributing to the overall twitch force recovery.

Next, we looked at the effect of the injury on the mechanical function of the adjacent tissue. In contrast to the center region of the tissue, the injury did not reduce the contractile function of the adjacent region. Right after injury, there was slight, but non-significant reduction in the strain magnitude, but overall contractile function was maintained (Figure e, f,). Interestingly, at Day 7, the magnitude of $E_{xx}$ in the injured condition is 2x more the control at -5.5 ± 1.3% (mean ± SEM) compared to -2.8 ± 0.4% (mean ± SEM). This suggest that the CMs in the adjacent regions may be increasing in contractile function over time to compensate for the loss from injury. This would explain the force recovery seen in Figure 4a, and indicates functional myocardium adjacent to the scar is affected by having the scar-like region as a boundary condition. This presents an interesting context to enable to study the mechanics of cardiac scars in an in vitro setting.

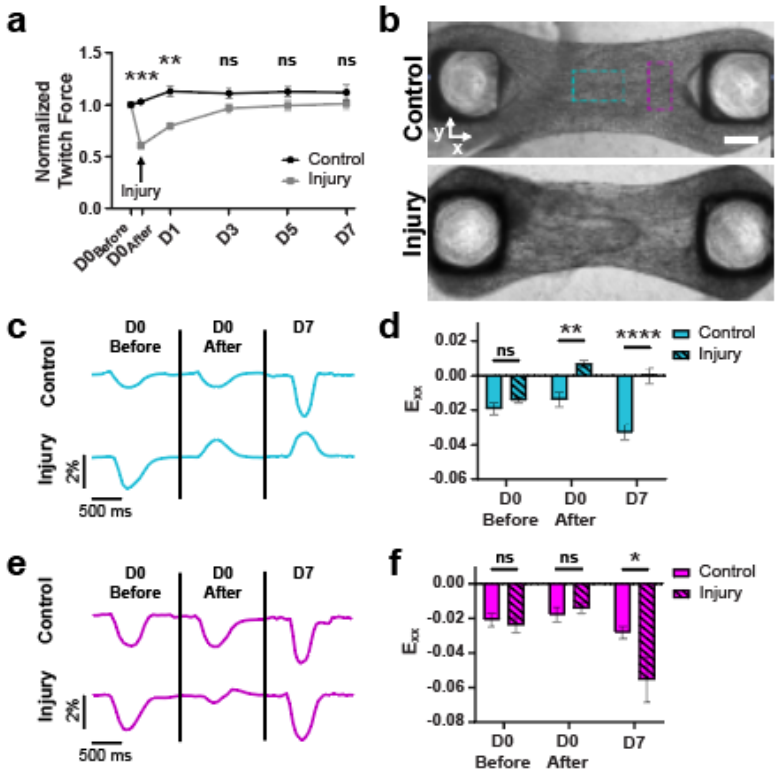


**Figure 2.4 Force recovery over time corresponds with increased contraction in regions adjacent to injury. a)** Normalized twitch force before injury and over time after injury for control (black) and injured (gray) tissues normalized to before injury force for each tissue, ***: $p < 0.001$, **: $p < 0.01$, n = 26 (injury), 25 (control). **b)** Brightfield images of control (top) and injured (bottom) EHT post-injury. Dashed boxes indicate regions of interest for traces and analysis in Figure 4c, d, e, f. Center region (cyan), and adjacent region (magenta). Scale bar = 200 μm. **c)** Example traces of $E_{xx}$ for the same control (top) and injury (bottom) tissues over time in center region indicated in Figure 4b (cyan) at Day 0 before injury, Day 0 after injury, and Day 7 after injury. **d)** $E_{xx}$ in center regions as defined in Figure 4b (cyan) for control and injury tissues at Day 0 before injury, Day 0 after injury, and Day 7 after injury, **: $p < 0.01$, ****: $p < 0.0001$, n = 6-11. **e)** Example traces of $E_{xx}$ for the same control (top) and injury (bottom) tissues over time in adjacent region indicated in Figure 4b (magenta) at Day 0 before injury, Day 0 after injury, and Day 7 after injury. **f)** $E_{xx}$ in adjacent regions as defined in Figure 4b (magenta) for control and injury tissues at Day 0 before injury, Day 0 after injury, and Day 7 after injury, *: $p < 0.05$, n = 6-11. Bar plots represent means and error bars represent SEM.

## 2.4 Discussion

After an acute local injury to the heart, local tissue remodels to adapt to the sudden loss of CMs in a region. In the first few days of this remodeling, starting just hours after insult, the infarct zone undergoes what is known as infarct expansion, where degradation of ECM leads to wall thinning, and dilation, causing increased wall stress[68,72,73]. These changes induce compensatory mechanisms in the nonischemic regions which show increased contractility or shortening, however despite this hyperkinesis, much of this effect is expended in the stretching of the infarct zone during contraction, a process known as systolic bulging[74,136,159,160]. Then in the longer term, after these initial few days, larger scale remodeling occurs, including myocyte hypertrophy and changes in the ventricular architecture to better distribute the increased wall stresses[68,74,135]. Overtime these remodeling changes which seek to help compensate, lead to progressive dilation, scar expansion, and decreased function, together leading to heart failure. Here, we demonstrate the creation of a focal cardiac fibrosis model through acute localized injury in an EHT. The acute damage by a high-power laser subjects only a region of functional tissue to a sudden cell loss. By inducing injury acutely, the model captures the loss of function from injury as well as enables the study of the subsequent injury response and compensatory recovery mechanisms at the site of injury. Importantly, the uninjured cells in neighboring regions that are adjacent to the injury, are affected by this loss and adapt.

This phenomenon is similar that which is seen after an acute MI, where a region of the heart that undergoes hypoxia experiences a large cell loss and the surrounding viable tissue must adapt[68,74]. Following the injury we observe a loss in the contractility of the injured region, and even stretching of this region, potentially representing a similar phenomenon to systolic bulging found in vivo[74,160]. Investigating the contractility in the injury-adjacent regions, we found increased shortening during contraction, mirroring the hyperkinesis observed in the border zone and

surrounding regions in in vivo infarcts[74,159]. This ability to capture regional compensatory mechanism provides an opportunity to better understand the loading and stress responses post-acute injury.

In vivo after an acute hypoxic event, the replacement fibrosis of the region is first led by an extensive immune response characterized by recruitment of neutrophils and macrophages to the hypoxic region and subsequent fibroblast activation and fibrosis[161–163]. Interestingly, in this model, we are able to capture signs of a fibrotic response as evidenced by notable increases in both vimentin and ECM even in the absence of immune cells, suggesting that the compensatory changes in cardiac tissue may be driven simply by the increased density of fibroblasts in the region owing to their ability to migrate, proliferate, and replace areas experiencing CM loss. One potential mechanism for this process could be that the induced apoptotic and necrotic cell death in our the model may elicit a non-immune cell inflammatory response which activates the fibroblasts to deposit ECM and increase vimentin expression[164–167], and warrants further investigation.

The ability to use an in vitro model to study acute focal damage to cardiac tissue is a powerful tool to better understand the processes occurring following acute cardiac injury. While in vitro models of focal cardiac fibrosis exist[128–130], this model is uniquely able to capture the response to injury and loss of CMs for CMs and CFs in surrounding regions. With this approach, we have high levels of control over the tissue architecture and composition and the damage, enabling the study of acute local injuries of different magnitudes or at different regions of the heart, and response of the remaining tissue. In the future, we propose that this model could be used to perturb functional interventions to reveal new targets which prevent the progressive deterioration of cardiac function seen in vivo. As EHT models become more sophisticated, this model could be expanded to study other processes associated with cardiac repair, such as immune cell activation or re-vascularization of injured tissues.

## 2.5 Supplemental Data

**Video 2.S1.** Video of calcium imaging of control cardiac microtissue spontaneously beating at Day 0 before injury. Related to Figure 2.3b.

**Video 2.S2.** Video of calcium imaging of injured cardiac microtissue spontaneously beating at Day 0 after injury. Related to Figure 2.3b.

**Video 2.S3.** Video of calcium imaging of control cardiac microtissue spontaneously beating at Day 7 post-injury. Related to Figure 2.3d.

**Video 2.S4.** Video of calcium imaging of injured cardiac microtissue spontaneously beating at Day 7 post-injury. Related to Figure 2.3d.

**Video 2.S5.** Video of control cardiac microtissue spontaneously beating at Day 0 before injury.

**Video 2.S6**. Video of control cardiac microtissue spontaneously beating at Day 0 after injury.

**Video 2.S7.** Video of control cardiac microtissue spontaneously beating at Day 7 post-injury.

**Video 2.S8.** Video of injured cardiac microtissue spontaneously beating at Day 0 before injury.

**Video 2.S9.** Video of injured cardiac microtissue spontaneously beating at Day 0 after injury.

**Video 2.S10.** Video of injured cardiac microtissue spontaneously beating at Day 7 post-injury.

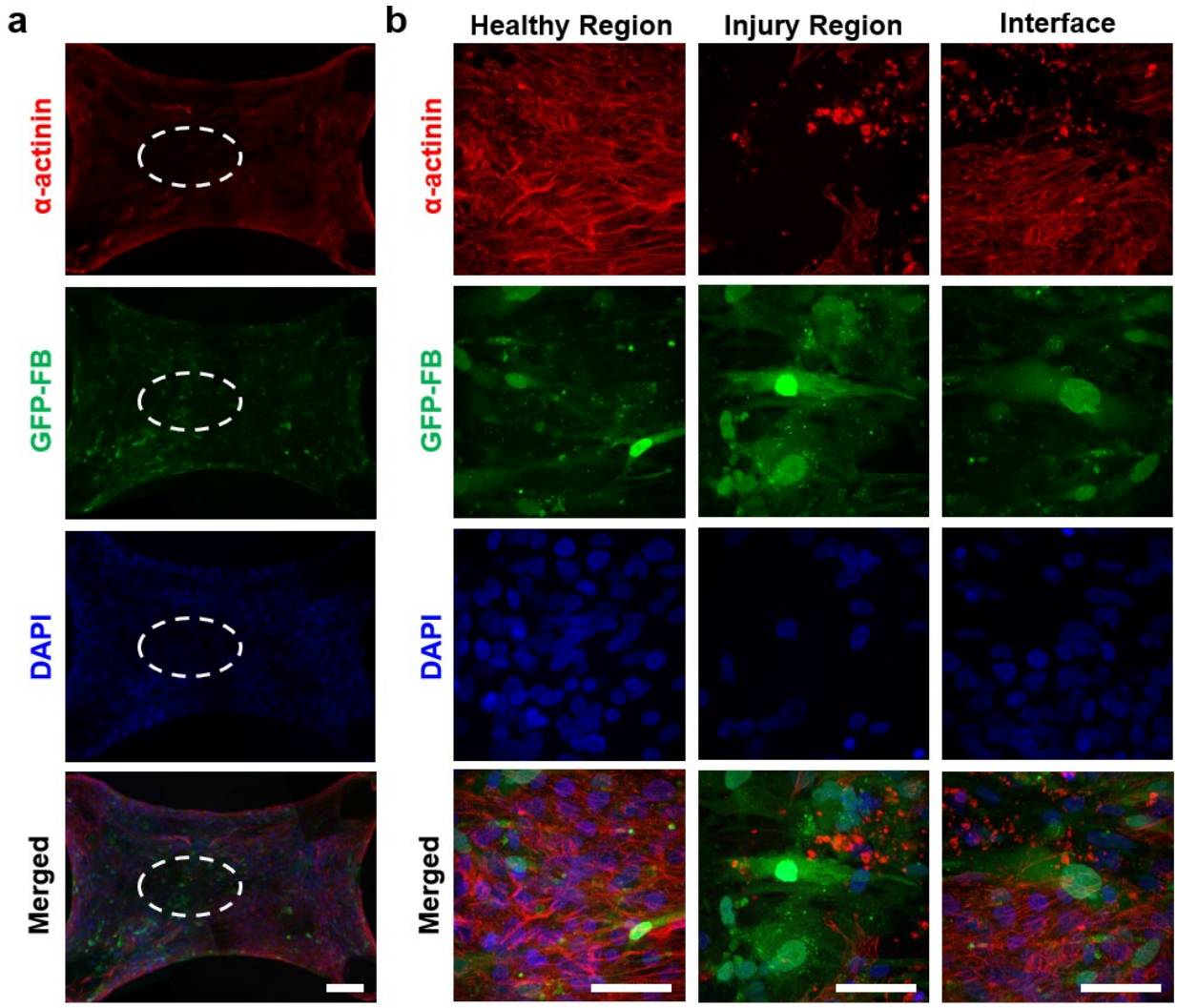


**Figure 2.S1.** Microdissection knife can be used to create local changes to cell populations in cardiac microtissues. a) Low magnification maximum projection of z-stack of cardiac microtissue after healing from incision injury by microdissection knife showing α-actinin (red), GFP-tagged cardiac fibroblasts (green), DAPI (blue). White dashed oval indicates original incision. Scale bar = 100 μm. b) High magnification maximum projections of z-stacks of different regions of a cardiac microtissue: healthy region (left), injury region (center), interface (right) showing α-actinin (red), GFP-tagged cardiac fibroblasts (green), DAPI (blue). Scale bar = 50 μm.

# Chapter 3: Voltage imaging of cardiac cells and tissue using the genetically encoded voltage sensor Archon1

The work described in this chapter is already published in a peer-reviewed journal. It is the result of collaborative work between myself and a collaborator, as co-first authors. Myself and my collaborator worked together on all parts of this manuscript, with my contributions including design, preparation, and execution of all experiments, imaging, data analysis, and the preparation and writing of the publication. https://doi.org/10.1016/j.isci.2020.100974

## 3.1 Abstract

Precise measurement of action potentials (APs) is needed to observe electrical activity and cellular communication within cardiac tissue. Voltage-sensitive dyes (VSDs) are traditionally used to measure cardiac APs, however they require acute chemical addition that lacks specificity towards the plasma membrane and prevents chronic imaging. Genetically encoded voltage indicators (GEVIs) enable long-term studies of APs without the need of chemical additions, but current GEVIs used in cardiac cells and tissue exhibit poor kinetics and/or low signal-to-noise (SNR). Here, we demonstrate the use of Archon1, a recently developed GEVI, in hiPSC-derived cardiomyocytes (CMs). When expressed in CMs, Archon1 demonstrated fast kinetics comparable to that achieved via patch-clamp electrophysiology, and high SNR significantly greater than the VSD Di-8-ANEPPS. Additionally, Archon1 enabled monitoring of APs across multiple cells simultaneously in 3D cardiac tissues. These results highlight Archon1's capability to investigate the electrical activity of CMs in a variety of applications, and its potential to probe functionally-complex *in vitro* models, as well as *in vivo* systems.

## 3.2 Introduction

The measurement of electrical potential and conduction in the heart are important for understanding how electrical signals propagate through cardiac tissue in both healthy and diseased conditions. Although numerous methods exist for monitoring whole-heart voltage (EKG, EPS, etc), few techniques examine the properties at the individual cell level within cardiac tissue. Intracellular calcium release, triggered by action potentials (APs), has long been used to study mechanisms such as excitation-contraction coupling, and as a proximal measurement for signal propagation[168–171]. However, calcium does not provide insight into membrane voltage dynamics and individual AP waveforms, which may be altered in biological, pharmacological, or pathological states[172–180]. Recent attempts to study cardiac membrane potential have made use of voltage-sensitive dyes (VSDs) such as the ANEPPS series or the PGH series[181–186]. Although many of these VSDs have the time resolution necessary to capture AP dynamics of cardiac cells, they often suffer from poor signal-to-noise ratio (SNR) and membrane localization, and are often cytotoxic[182,187]. In addition, by nature, VSDs are transient and must be reapplied to samples, which hinders long term studies; they also lack the ability to label specific subpopulations.

Genetically encoded voltage indicators (GEVIs), which have been successfully utilized in a similarly electrically-excitable cell population, neurons[188–200], have recently been deployed in cardiac tissue to overcome the shortcomings of VSDs[173,187,201]. Although GEVIs such as ArcLight, Mermaid, or the VSFP series have been successfully applied to study arrhythmias, as well as aid in cellular phenotyping, these GEVIs lack the time resolution, sensitivity, and SNR to capture voltage dynamics under various conditions[173,202–205]. For example, ArcLight, a commonly used GEVI, has slow kinetics which hinders its ability to capture the characteristic upstroke morphology of cardiac APs and any perturbations to this upstroke such as those caused by diseases or drugs[173,206–208]. In contrast, the GEVI VSFP3.1 has relatively fast kinetics (activation time ~ 1.3ms) but displays

fluorescence changes of only 0.5% per 100mV which impedes monitoring of subthreshold fluctuations and contributes to a very low SNR[209,210]. Many of these GEVIs thus suffer from this dichotomy between superior kinetics and sensitivity.

Recently, Piatkevich et. al. developed a high-performance GEVI called Archon1, a far-red fluorescent plasma transmembrane protein evolved from the Arch3 opsin, with fluorescence emission linearly dependent on membrane voltage[197]. Archon1 exhibits high temporal resolution, sensitivity, and brightness under simple one-photon widefield microscopy which enabled imaging of neural activity in mouse cortical brain slices, whole zebrafish, and *C. elegans*[197]. Archon1's fast kinetics and linear fluorescence-voltage relationship resulted in fluorescence traces which closely matched simultaneously recorded electrophysiology. Since Archon1 does not need chemical cofactors, the sensor showed no phototoxicity and retained photostability for up to 800 seconds in cultured mouse neurons[197] . In addition, Archon1 demonstrated excellent membrane localization and did not alter membrane resistance, capacitance, or resting potential as compared to non-expressing cells. Its far-red excitation is also compatible with blue-light driven optogenetics enabling all-optical electrophysiology[197,211]. These features of Archon1, along with its easily adaptable one-photon widefield imaging setup, make it an ideal GEVI candidate to deploy in other electrically-dependent systems. Here, we demonstrate Archon1's utility for monitoring cardiac APs in both 2D cell culture and 3D tissue environments under a variety of biologically -relevant conditions.

## 3.3 Methods

### 3.3.1 Cell Source Details

iPSC cells I.D. Personal Genome Project (PGP1) were isolated from male, 53 years of age, fibroblasts. hMSCs were isolated from purchased Human Bone Marrow Mononuclear Cells (Lonza), cells were from a male 39.

### 3.3.2 Cell Preparation and Culture

iPSCs were screened for copy number variants and virtual karyotyping using Illumina HumanOmniExpress-12v1 arrays. iPSCs were maintained in complete mTeSR1 medium (Stem Cell) and differentiated in monolayers into CMs using RPMI 1640 Medium, GlutaMAX (Gibco) supplemented with B-27 Supplement, minus insulin (Gibco). CHIR99021 (12μM, Tocris) was added on Day 1 of differentiation to activate Wnt pathway, and IWP4 (5μM, Tocris) was added for Days 3 and 4 to inhibit Wnt pathway. Cells were switched to RPMI 1640 Medium, GlutaMAX containing standard B-27 Supplement (Gibco) on Day 10. Once spontaneous beating was observed, CMs were metabolically selected using glucose free, RPMI 1640 Medium (Gibco) supplemented with 4mM of DL-lactate (Sigma) for two days. Following selection, CMs were maintained in RPMI 1640, GlutaMAX supplemented with B-27 Supplement. hMSCs were maintained in DMEM, low glucose medium (Gibco) with 10% Fetal Bovine Serum (Sigma) and 1% Penicillin-Streptomycin (Gibco) and used between passages 6 – 9. All cells were maintained at 37°C with 5.0% $CO_2$.

### 3.3.3 Cardiomyocyte Transduction

CMs were replated onto Fibronectin, human (Corning) coated plates. 24 hours after replating, CAG-FLEX-Archon1-KGC-EGFP-ER2 rAAV2 (Archon1) (MOI: 2000-3000) and CMV-Cre AAV9 (Addgene) (MOI: 4000-6000) were added. After 2 days, viruses were

washed out and CMs were maintained in RPMI 1640 supplemented with B27. Experiments were performed between days 7 and 14 post-transduction.

### 3.3.4 Engineered Cardiac Tissue Seeding

Engineered cardiac tissues were prepared as previously described[108]. Briefly, Polydimethylsiloxane micro-fabricated tissue gauges (μTUGs) were prepared by molding from SU-8 masters. μTUG devices were UV light sterilized then treated with 0.05% Pluronic F127 (Sigma) for 30 minutes to prevent cell and extracellular adhesion. CMs and hMSCs were dissociated and suspended together (8.4% CMs expressing Archon1, 75.6% non-expressing CMs, 16% hMSCs, total 1.2 million cells/ml) in a hydrogel consisting of 2.25mg/ml Collagen I, Rat Tail (Corning) and 0.5mg/ml human plasma fibrinogen (Sigma). The cell suspension was centrifuged into device microwells and excess was removed by dewetting. Hydrogels were polymerized at 37°C for 20 minutes and then tissues were maintained in DMEM (Corning) 10% Fetal Bovine Serum (Sigma), 1% Penicillin-Streptomycin (Gibco), GlutaMAX Supplement (Gibco), MEM Non-Essential Amino Acid Solution (Gibco). Tissues were imaged on Day 6-9 after seeding. 5μM MYK-461 (Cayman Chemical) was used to inhibit CM contraction during multi-cell imaging.

### 3.3.5 Electrophysiology

Two-photon microscopy was used for visually guided patch clamp recordings of CMs. CMs were visualized using the EGFP fluorescent marker bound to Archon1, and the electrode pipette was visualized by adding the orange fluorescent dye Alexa Fluor 568 hydrazide (Thermo Fisher Scientific) to the intracellular electrode solution (50μM). Imaging was performed using a two-photon microscope (Thorlabs) using a 20X, NA 1.0 (Olympus) objective lens. A mode-locked Ti:Sapphire laser (Chameleon Ultra II; Coherent) set to a wavelength of 900 nm was used to excite both the Alexa Fluor 568 and EGFP.

Fluorescence was detected using two photo-multiplier tubes (Hamamatsu) equipped with 525/25nm and 607/35nm filters to separate emission from EGFP and Alexa Fluor 568, respectively.

Electrical recordings acquired simultaneously with optical recordings used the same imaging setup described in detail in the "Microscopy" section for the visualization of the patching process. The electrode pipette was visualized by adding the green fluorescent dye Alexa Fluor 488 hydrazide (Thermo Fisher Scientific) to the intracellular electrode solution (50μM). The electrode was placed in the on-cell configuration using 470 nm LED excitation, before switching to the far-red imaging of Archon1 and proceeding with the electrical recordings.

To verify that Archon1 does not alter CMs electrically, cells expressing Archon1 and non-expressing control cells were patched within the same monolayer. Differential interference contrast (DIC) microscopy (Olympus BX51W1) was used for visualizing the CMs and patch pipettes. CMs expressing Archron1 were identified using the EGFP tag.

CM monolayers on coverslips were immersed in the bath solution (140mM NaCl, 5.4mM KCl, 1mM $MgCL_2$, 10mM D-glucose, 1.8mM $CaCl_2$, 10mM HEPES; pH 7.4 with NaOH) (Yazawa, 2018). A silver-chloride wire placed inside the bath was used as the ground electrode. Intracellular membrane voltage recordings were carried out using patch clamp electrodes with resistance values between 8 MΩ and 12 MΩ. Electrodes were pulled using a horizontal puller (Sutter Instruments) using filamented, thin-wall glass (Sutter Instruments) and filled with the intracellular solution (120mM potassium D-gluconate, 15mM KCl, 4mM Na2ATP, 2mM trisGTP, 4mM ditrisphosphocreatine, 10mM EGTA, 1mM $CaCl_2$, 10mM HEPES) (Yazawa, 2018). Electrodes were lowered into the bath approximately 200 μm above the coverslip surface using a micromanipulator (Sutter Instruments) and

then slowly lowered to a cell. A small amount of positive pressure was used to push away debris and prevent clogging of the pipette tip. A 10 mV voltage step was used to measure seal resistance and the capacitance associated with the glass electrode. Upon seal formation (> 1GΩ) in the on-cell (i.e. cell-attached) configuration, capacitance compensation was used to eliminate the pipette capacitance. Small amounts of transient negative pressure were used to break the seal and establish whole cell recordings. The membrane voltage was recorded in current clamp with full bridge balance compensation and no injected current. Trace signals were amplified and low-pass filtered at 10 kHz before being digitized at 20 kHz. All electrophysiology was carried out using a Multiclamp 700B (Molecular Devices) and a Digidata 1440A (Molecular Devices).

### 3.3.6 Di-8-ANEPPS

Di-8-ANEPPS (Santa Cruz) was dissolved in Dimethyl Sulfoxide (DMSO, Thermo Fisher). CMs transduced with Archon1 were incubated with 10μM Di-8-ANEPPS, RPMI 1640, no phenol red medium (Gibco)and 0.05% F127 Pluronics for 15 minutes. After incubation, samples were washed 3x with RPMI 1640, no phenol red medium before imaging. Imaging was done both with spontaneously beating and electrically paced (0.5 - 3 Hz) cells. Cells with Di-8-ANEPPS were imaged using a 470 nm LED (ThorLabs Inc., M470L3) with a 570 nm LP dichroic (Olympus, OCT49005BX3) and a 620/60 nm (Olympus, OCT49005BX3 bandpass emission filter.

### 3.3.7 Ion Channel Inhibitors

E-4031 dihydrochloride (Abcam) and Nifedipine (Abcam) were dissolved in DMSO at 50mM and 100mM, respectively. Drug solutions were made by diluting stock solutions with RPMI, no phenol red medium to 20x the final drug treatment concentration. For all

samples, 10 cells were imaged prior to drug treatment. Then, concentrated drug solution was added to samples to make final concentrations of 10nM, 30nM, and 100nM for E-4031 and 30nM, 100nM, and 300nM for Nifedipine. DMSO concentrations for all samples were 0.0003% or less, DMSO control was performed using 0.0003% DMSO. Samples were incubated at 37°C for 20 minutes with drug, and the 10 same cells were imaged. All cells were paced at 1Hz.

### 3.3.8 Microscopy

All optical recordings were acquired using a conventional one-photon widefield fluorescence microscope equipped with an ORCA Flash 4.0 V3 Digital CMOS camera (Hamamatsu Photonics K.K., C13440-20CU) or Hamamatsu ORCA Fusion Digital CMOS camera (Hamamatsu Photonics K.K., C14440-20UP), 10x NA0.3 CFI Plan Fluorite water immersion objective (Nikon), 40x NA0.8 CFI APO NIR water immersion objective (Nikon). ArchonI's green GFP fluorescence was imaged using a 470 nm LED (ThorLabs Inc., M470L3) with 470/25 nm bandpass excitation filter, 495 nm dichroic, and a 525/50 nm bandpass emission filter (Olympus, OCT49002BX3). ArchonI's far-red fluorescence was imaged using a 140 mW 637 nm laser (Coherent Obis 637-140X), 635 nm laser dichroic filter, and a 664 nm long pass emission filter (Olympus, OCT49006BX3) with 1x1 or 2x2 binning. Optical recordings were acquired at 50 or 100 Hz with HCImage Live (Hamamatsu Photonics K.K.) HC Image Live data were stored as multi-TIFF files and further analyzed offline in Fiji/ImageJ and MATLAB (Mathworks Inc.). Sample were maintained at 37°C throughout imaging using a heated stage. Samples were paced using an Ionoptix C-Pace EM using carbon electrodes made from carbon rods (Ladd Research) attached to platinum wires (Sigma) submerged in medium. Pacing was performed at 20V, with a 10ms duration, at indicated frequencies.

### 3.3.9 ROI identification

Images were imported into Fiji/ImageJ and ROIs were manually segmented by examining each time-series to identify areas with clear cell borders. Voltage traces for each ROI were extracted in Fiji/ImageJ and used for subsequent analyses.

### 3.3.10 Voltage trace processing

Before analysis, we pre-processed the fluorescence traces per the following: Di-8-ANEPPS traces were first inverted by multiplying -1 so that increases of membrane potential corresponded to increases in the trace value. The traces were then detrended using the MATLAB function "detrend" and rescaled so that the maximum intensity equaled 100 while the minimum intensity equaled zero. After rescaling, the Archon1 and Di-8-ANEPPS traces were resampled at 20kHz to match the sampling rate of electrophysiological recordings.

### 3.3.11 Rise time calculation

To calculate rise time, we first identified the peaks and valleys of each waveform. The peaks of each waveform were identified using the MATLAB function "findpeaks", and the valleys were defined as the first data point before the peak with negative slope and with rescaled intensity value less than 50. To ensure that we captured the whole waveform, we excluded any peak that occurred within the first 0.5 seconds or within the last 1.5 seconds of recording. The rise time was defined as the duration between the take off point (10% above the valley) to 90% of the peak.

### 3.3.12 APD90 and APD50 calculation

To obtain the ADP90 for each waveform, we first calculated a threshold at 10% of the amplitude (the intensity difference between the peak and its prior valley) above the valley. We then identified two time points: the time point right before the intensity

increased over the threshold during the rising phase, and the time point right after the intensity decreased below the threshold during the falling phase. The ADP90 was defined as the duration between these two time points. A similar calculation was conducted for determination of APD50 values, except with a threshold set at 50% of the amplitude above the valley.

### 3.3.13 Signal to noise ratio (SNR) calculation

To calculate the SNR, we divided the amplitude of each waveform (signal) by the noise, which we defined as the standard deviation of the 10 Hz high-pass-filtered trace.

## 3.4 Results

### 3.4.1 Demonstration of Archon1 for monitoring action potentials of iPSC-derived cardiomyocytes

Archon1 was expressed in 2D monolayers of human induced pluripotent stem cell (iPSC)-derived cardiomyocytes (CMs) using both Cre-dependent CAG-Archon1-KGC-EGFP-ER2 (Archon1) and CMV-Cre AAV (Figure 3.1A), 5-7 days after spontaneous beating was observed. CM membrane potential was recorded optically at 100Hz using a scientific cMOS camera ($l_{ex}$=637nm). Archon1 fluorescence changes exhibited typical cardiac AP waveforms with clearly identifiable phases (Figure 3.1B,C; i: resting potential, ii: peak depolarization, iii: end of repolarization; Video 3.S1). Changes in intensity were not due to motion from cellular contraction as indicated by lack of fluorescence changes in the GFP channel (Video 3.S2), as compared to the Archon1 channel (Video 3.S1). In order to quantify AP duration, we calculated rise time ($t_{rise}$; defined by 10% to 90% of the valley peak duration), APD50 (AP duration at 50% repolarization), and APD90 (AP duration at 90%

repolarization) (Figure 3.1D, see Methods). Without electrical stimulation, APD90 values ranged from 345-1210ms (n = 31 cells, 880±218ms, mean±standard deviation, Figure 3.1C right). We then evoked APs by electrically pacing CMs at 0.5 Hz, 1Hz, and 2 Hz, and found that Archon1 fluorescence faithfully followed electrical stimulation (Figure 3.1E; respective APD90 distributions, Figure 3.1F). Together, these results demonstrate that Archon1 can robustly capture AP dynamics and waveform morphology, and this capability is maintained at higher frequencies.

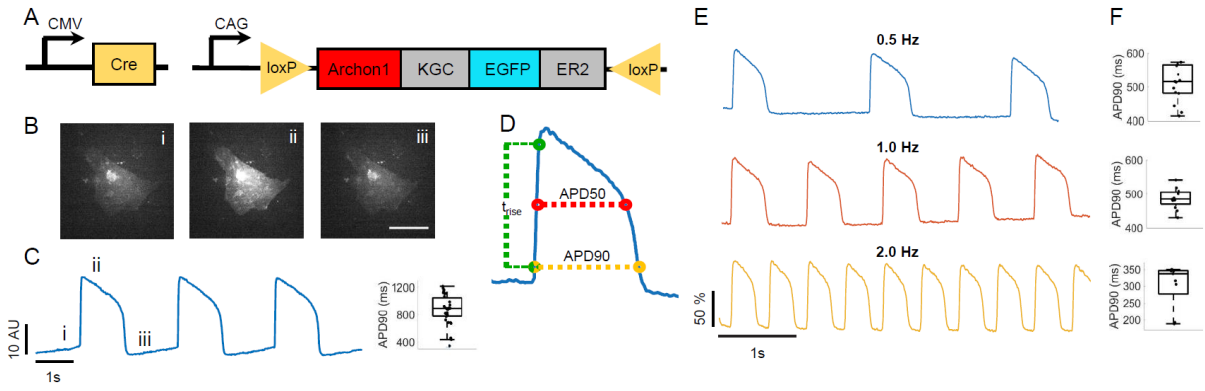


**Figure 3.1. Demonstration of Archon1 for monitoring action potentials of iPSC-derived cardiomyocytes**. (**A**) Diagrams of cre-recombinase AAV system used to infect CMs with Archon1. KGC: linker, ER2: ER export trafficking sequence. (**B**) Single frame images of CM expressing Archon1 at different phases of an AP as shown in **C**. Scale bar, 50 μm. (**C**) Left, optically recorded raw voltage trace for cell shown in **B**. Right, quantification of APD90, as defined in **D**, per voltage trace for unpaced CMs (n= 31 cells). (**D**) An example AP waveform with APD90, APD50, and rise time ($t_{rise}$) defined. (**E**) Representative normalized fluorescence voltage traces from CM electrically paced at 0.5 Hz (blue), 1 Hz (orange), and 2 Hz (yellow). (**F**) Corresponding APD90 box plot for each pacing shown in E (from n = 15, 12, 9, cells, respectively).

### 3.4.2 Characterization of Archon1 in iPSC-derived Cardiomyocyte Monolayers

To quantify Archon1 performance, we conducted patch-clamp electrophysiology while simultaneously optically recording Archon1 fluorescence of CMs. We found that membrane voltage recorded via Archon1 fluorescence matched well with that recorded via electrophysiology (representative overlay in Figure 3.2A). Archon1 fluorescence was linearly correlated with electrically recorded membrane potential (Figure 3.2B; example corresponding to 3.2A; Least Squares Regression Line: $y = 0.009x - 0.584$; $R^2 = 0.996$) for all simultaneously recorded cells (n = 4 cells, Figure 3.2C; Least Squares Regression Line: $y = 0.926x - 0.048$; $R^2 = 0.989$). In addition, Archon1 expression did not alter CM properties such as resting membrane potential, beat amplitude, membrane resistance, rise time, APD90, and beat period (Figure 3.S1).

To further characterize the performance of Archon1, rise times were calculated across all CMs recorded with electrophysiology and Archon1 (n = 17 cells for electrophysiology, 67 cells for Archon1; Figure 3.2D). The rise time of Archon1 (29.8±13.2ms, mean±standard deviation) was slightly longer than that of electrophysiology (15.9±5.6ms, mean±standard deviation; Ephys ↔ Archon1: $p$=5.8E-05; two-tailed student t-test). To examine how these kinetic measures are influenced by the the difference in data acquisition rates, 10-20kHz for electrophysiology vs. 100Hz for Archon1, we down sampled the same electrophysiology data to 100Hz to match the optical imaging frame rate. We obtained a rise time of 23.3±9.4ms (mean±standard deviation) for down-sampled electrophysiology traces, which is no longer significantly different from Archon1 ($p$=0.06, two-tailed student t-test; Figure 3.2D).

We also compared Archon1 with a widely used red membrane-targeted voltage dye, Di-8-ANEPPS ($I_{ex}$=470nm; Figure 3.2E, Video 3.S3). APD90 values were also compared per

cell between Di-8-ANEPPS and Archon1, and showed a nearly 1:1 correlation (Least Squares Regression Line: y = 1.001x – 0.003, $R^2$ = 0.954; Figure 3.2F; n = 29 cells). To compare performances across electrophysiology, Di-8-ANEPPS, and Archon1, we calculated the corresponding SNR (defined as the valley-to-peak amplitude divided by the standard deviation of the noise) for each method (n = 17, 29, 67 cells, respectively; Figure 3.2G). SNR was significantly different between all groups, with Archon1's SNR (Archon1: 30.7±9.3, mean±standard deviation) significantly higher than that of Di-8-ANEPPS (Di-8-ANEPPS: 20.2±6.1, mean±standard deviation; Archon1 ↔ Di-8-ANEPPS: $p$=4.87E-08; two-tailed student t-test), but significantly lower than that of electrophysiology (Ephys: 40.36±13.5, mean±standard deviation; Ephys ↔ Archon1: $p$ = 8.3E-04). Together, these results demonstrate that Archon1 voltage imaging exhibited comparable kinetics to that achieved via patch-clamp electrophysiology, and SNR significantly better than the VSD Di-8-ANEPPS.

Because Archon1 is genetically encoded and optical voltage imaging does not incur mechanical damage to the cell membrane, as with electrophysiology, Archon1 should allow repeated imaging of the same cells. To demonstrate Archon1's robustness over time, CMs expressing Archon1 were imaged repeatedly at three time points: (t = 0, 1, and 3 hrs) (n =14 cells, Figure 3.2H, example in Figure 3.S2A-C). Over repeated recordings, SNR remained constant (36.0±17.7, 34.1±17.1, 35.1±15.6 mean±standard deviation for t = 0,1,3 hrs respectively; $p$ = 0.96, repeated measures one-way ANOVA). We also found that Archon1 was highly photostable over 5 minutes of continuous imaging with SNR remaining stable across the recording (Figure 3.S2D-F; SNR: 24.67±0.659, 24.72±0.475, 24.56±0.816, mean±standard deviation, for t = 0-20s, 100-120s, 280-300s, respectively; $p$ = 0.82, repeated measures one-way ANOVA). Further, CMs expressing Archon1 retained expression months

post-infection (see Video 3.S4 for video of Archon1-expressing CM at day 62 after infection). Archon1 is thus capable of monitoring CM APs over extended periods of time, with high fidelity as compared to currently available methods, in cultured 2D monolayers.

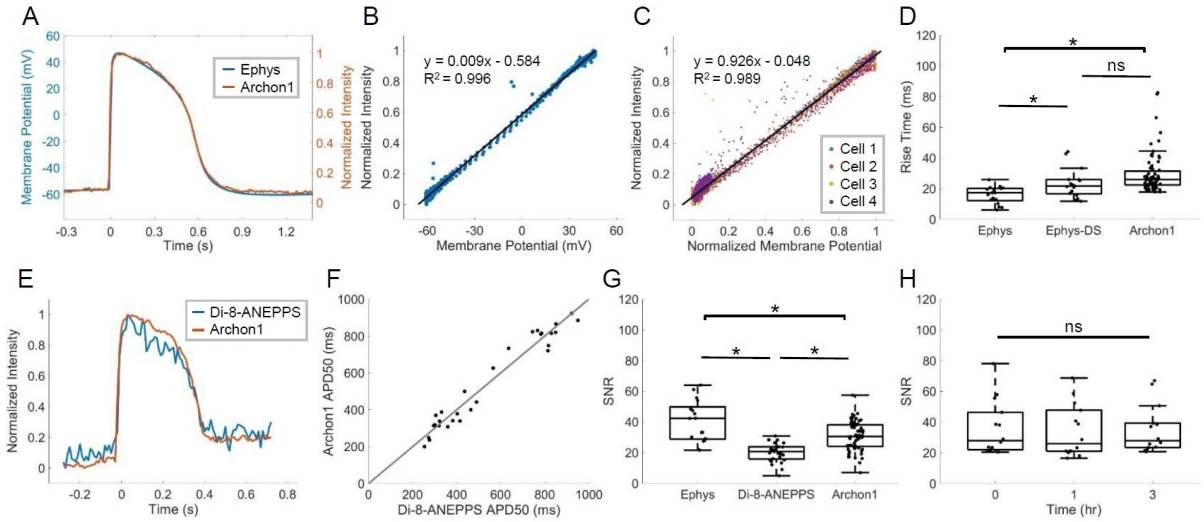


**Figure 3.2. Characterization of Archon1 in iPSC-derived cardiomyocyte monolayers**. (**A**) Representative overlay of single AP waveform simultaneously measured using patch-clamp electrophysiology (blue) and Archon1 fluorescence (orange). (**B**) Normalized intensity Archon1 fluorescence trace vs. membrane potential recorded via electrophysiology for cell simultaneously recorded in **A.** Trendline equation and $R^2$ value shown on chart. (**C**) Normalized intensity Archon1 fluorescence traces vs. normalized membrane potential from all simultaneously recorded cells (n = 4). Trendline equation and $R^2$ value shown on chart. (**D**) Quantification of rise time, as defined in **1D**, per cell for patch-clamp electrophysiology (*Ephys*; acquired at 10-20kHz), down-sampled electrophysiology (*Ephys-DS*; same electrophysiology data downsampled to 100Hz to match the acquisition rate of Archon1) and Archon1 (*Archon1;* acquired at 100Hz) from n = 17, 17, and 67, cells, respectively. *: $p < 0.05$ in two-tailed student t-test, ns: $p > 0.05$ in two-tailed t-test. (**E**) Representative overlay of single AP waveform measured with Di-8-ANEPPS (blue) vs. Archon1 (orange). (**F**) APD50 values per cell for Archon1 vs. Di-8-ANEPPS. Trendline equation and $R^2$ value shown on chart. (**G**) Quantification of SNR (defined in Methods) per cell for patch-clamp electrophysiology, Di-8-ANEPPS, and Archon1 (from n = 17, 29, 67, cells, respectively). *, $p < 0.05$ in two-tailed student t-test. (**H**) Quantification of SNR per cell recorded repeatedly with Archon1 at t = 0, 1hr, and 3hrs (n = 14 cells). ns: $p > 0.05$ in two-tailed t-test. Box plots represent 25$^{th}$ to 75$^{th}$ percentiles, with whiskers extending 1.5x the interquartile range, horizontal line represents median. All optical traces obtained at image acquisition rate of 100Hz; patch clamp electrophysiology acquisition rate, 10-20kHz.

### 3.4.3 Archon1 can reliably detect pharmacologically-induced changes in AP waveforms

To examine the sensitivity of Archon1 for detecting changes in AP waveforms, we recorded Archon1-expressing CMs upon the application of two well characterized ion channel inhibitors, E-4031 and Nifedipine. E-4031 is a hERG K+ ion channel inhibitor that prolongs the refractory period of the cardiac AP[175,177]. Nifedipine, on the other hand, is a Ca2+ ion channel inhibitor which shortens the AP plateau and overall AP duration and is commonly used to treat hypertension and angina[174]. Archon1 fluorescence was imaged from the same cells before and after inhibitor treatment. Treated groups were compared to a DMSO control group (Figure 3.3A). E-4031 treatment of 2D monolayers at increasing concentrations (3nM, 10nM, 30nM) showed concentration-dependent prolongation of APs. (Figure 3.3B). We compared the mean APD90 before and after E-4031 treatment for all concentrations and observed increasing %ΔAPD90 with increasing E-4031 concentration (mean±standard deviation, n=10; 3nM: 25.2±12.2%, 10nM: 43.2±8.9%, 30nM: 55.2±8.1%) in comparison to the %ΔAPD90 of the DMSO control (n=10, 1.7%±3.6%), consistent with previous studies[175,183,212–214] (Figure 3.3D). Nifedipine treatment of 2D monolayers at increasing concentrations (10nM, 30nM, 100nM) also showed the expected concentration-dependent shortening of AP length (Figure 3.3C). Comparison of the mean APD50 before and after treatments for all three concentrations showed an inverse relationship between %ΔAPD50 and Nifedipine concentration (n=10; 10nM: -7.3±2.0%, 30nM: -11.4±1.9%, 100nM: -25.0±4.4%, n=10), compared to the DMSO control (n=10, 1.9±4.3%) (Figure 3.3E), consistent with previous studies which have performed similar measurements[183,213–215]. Thus, Archon1 is capable of capturing changes in AP waveform morphology in 2D monolayers.

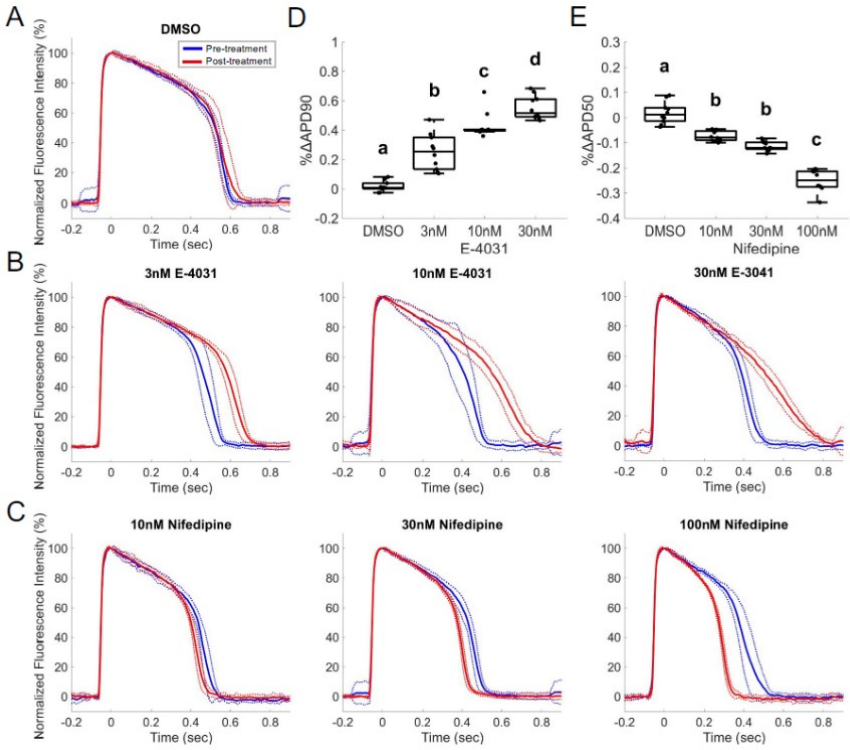


**Figure 3.3. Archon1 can reliably detect changes in AP waveforms induced by K+ and Ca2+ ion channel inhibitors**. E-4031 ($K^+$ Channel Blocker) and Nifedipine (Nif; $Ca^{2+}$ Channel Blocker) compared to DMSO control; electrically paced at 1Hz. (**A**) Average normalized Archon1 fluorescence intensity traces for DMSO control (n = 10 cells), (**B**) E-4031 (10nM, 30nM, 100nM; n = 10 cells, and (**C**) Nifedipine (30nM, 100nM, 300nM; n = 10 cells) before (blue) and after (red) drugs, SD (dotted lines). (**D**) %ΔAPD90 for E-4031 APs from pre-drug condition (**E**) %ΔAPD50 for Nifedipine APs from pre-drug condition where *a, b, c,* and *d* represent different statistical groups (all pairs Tukey HSD test).

### 3.4.4 Archon1 enables monitoring of action potentials within cardiac tissues

Engineered cardiac tissues can provide an optical, structural, and functional context which is more similar to *in vivo* tissue. The use of engineered cardiac tissues, particularly with iPSC-derived CMs, has been shown to increase both the structural and functional maturity of CMs, providing better models compared to more simple 2D monolayer

systems[216–219]. To demonstrate Archon1's ability to measure the APs of single cells embedded within a tissue, we constructed engineered cardiac tissues containing Archon1-expressing CMs alongside a stromal cell population (Figure 3.4A left, Video 3.S5; see Methods). The same Cre-recombinase system (Figure 3.1A) was used for controlled stochastic labeling of CMs to enable optical isolation of individual cells within the engineered tissues. Single CMs expressing Archon1 within the tissues were optically identified via EGFP fluorescence and their APs recorded in the far-red Archon1 fluorescence channel (Figure 3.4A right, 3.4B).

Across 3 unpaced tissues, APD90 ranged from 360-890 ms (mean±standard deviation: 655±143ms; range: 530ms), with cells from individual tissues more closely clustered (range: 321, 379, 442ms and n = 5, 7, 4 cells for Tissue 1, 2, 3, respectively; Figure 3.4C) demonstrating expected within-tissue homogeneity compared to between-tissue heterogeneity. The SNR and rise time across the three tissues (mean±standard deviation: 45.7±9.6, and 35ms±4.3 ms, for SNR and rise time, respectively; Figure 3.4D,E) were comparable to those of 2D monolayers (Figure 3.2D,G), demonstrating that Archon1 is as capable of measuring high fidelity APs in complex 3D environments, and highlighting its potential for use in future *in vivo* studies.

In order to investigate how CMs interact and synchronize in the tissue, we simultaneously recorded two cells in the same field of view in an unpaced tissue (Figure 3.4F,G). MYK-461, a cardiac-specific myosin ATPase inhibitor was used to prevent tissue contraction and associated movement related optical artifacts[220]. We found that the two cells' APs were highly synchronized (Figure 3.4G, gray lines), suggesting that they are likely electrically coupled within the tissue, even in the absence of externally-applied electrical pacing. In addition, by overlaying normalized single AP waveforms from these two cells, we found that the AP waveform morphology was largely similar, further highlighting their

intercellular synchrony (Figure 3.4H). The ability to simultaneously record APs from multiple CMs with single-cell precision enables the monitoring of intercellular conductance and/or whole tissue synchrony. Such measurements, when combined with high speed and ultra-large field of view imaging, could enable future studies to examine how individual cell APs contribute to population dynamics in complex 3D environments and *in vivo* systems.

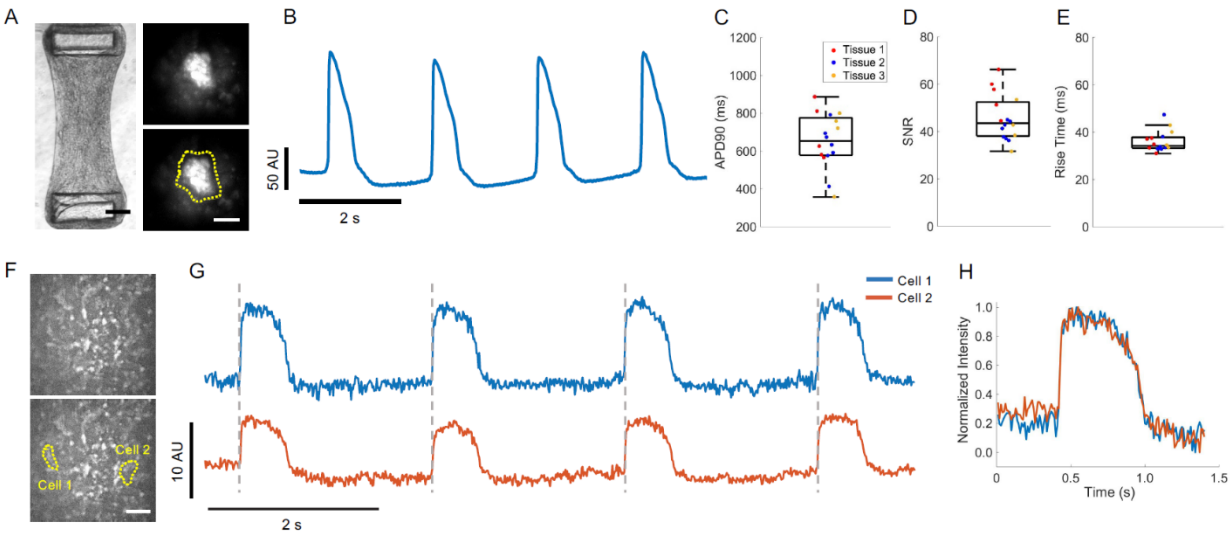


**Figure 3.4. Archon1 enables monitoring of APs in µTUG hMSC-cardiomyocyte tissues**. (**A**) Brightfield image of µTUG fibroblast-CM tissues (left). Scale bar, 250µm. Maximum minus minimum projection image of CM within µTUG tissue expressing Archon1 (top right), with corresponding ROI overlaid (bottom right). Scale bar, 20µm. (**B**) Optically recorded voltage trace for the cell shown in **A**. Image acquisition rate, 50Hz. (**C**) Quantification of APD90 for CMs within tissues (n = 5, 7, 4, cells for Tissue 1 (red), 2 (blue), 3 (yellow), respectively). (**D**) Quantification of SNR for CMs within tissues (n = 5, 7, 4, cells for Tissue 1 (red), 2 (blue), 3 (yellow), respectively). Tissues are colored as in **C**. (**E**) Quantification of rise time for CMs within tissues (n = 5, 7, 4, cells for Tissue 1 (red), 2 (blue), 3 (yellow), respectively). Tissues are colored as in **C**. Box plots displayed as described in **Figure 3.1**, image acquisition rate: 50Hz. (**F**) Max projection image of µTUG tissue (top), with cells expressing Archon1 identified in yellow (bottom). Scale bar, 50 µm. (**G**) Corresponding optically recorded voltage traces for cells identified in **F**, with gray dashed vertical lines demonstrating AP synchrony. Image acquisition rate, 100Hz. (**H**) Overlay of representative normalized AP from two traces shown in **G** highlighting waveform consistency.

### 3.5 Discussion

Here, we demonstrate the use of a high-performance GEVI, Archon1, to monitor cardiac action potentials in iPSC-derived cardiomyocytes in 2D monolayers and engineered 3D tissues. Our results demonstrate that Archon1 is capable of robustly reporting AP dynamics under a variety of conditions, including when exposed to electrical pacing and ion channel inhibitors, and has comparable sensitivity and time resolution to patch-clamp electrophysiology—the technically challenging but current gold standard in the field for measuring membrane potential. In addition, Archon1 outperformed the commonly used VSD, Di-8-ANEPPS, in SNR. In contrast to VSDs, Archon1 is fully genetically encoded, which enabled long-term studies and has the potential for cell-type specific labelling in *in vivo* models. Furthermore, the Cre-recombinase system used here enabled optical isolation of CMs within a complex 3D tissue environment, which can be easily translatable to imaging of whole heart slices or cardiac tissue in Cre-transgenic animals. Finally, Archon1 is capable of reporting membrane potential of multiple cells simultaneously, including in 3D tissue environments. This enables population studies, while retaining single-cell precision, allowing measurement of conduction velocity and AP propagation, as well as intercellular phase-locking or phase delay. Future studies could examine changes in individual cell voltage dynamics or intercellular propagation around and distal from injury or diseased sites within tissues.

Although we did not take advantage of this utility here, as Archon1 is a far-red indicator, it is compatible with blue light-driven optogenetic molecules such as channelrhodopsins[211]. These molecules could be paired to provide simultaneous control and monitoring of cardiac membrane potential. Similarly, Archon1 can be used together with the genetically encoded calcium indicator, GCaMP6, for simultaneous, multicolor imaging of voltage and calcium dynamics[180,221]. This could enable studies of diseases like Timothy syndrome or heart failure which affect both voltage dynamics and calcium handling[222–225]. Furthermore, the far-red spectrum of Archon1 enables

deeper penetration into tissues than those operating at shorter wavelengths, facilitating future *in vivo* applications.

The genetically encoded nature of Archon1 makes it a useful tool for longer duration studies of disease mechanisms, such as detecting arrhythmias, which are known to affect AP waveforms or for phenotyping atrial, ventricular, or nodal cells based on waveform morphology[173,178,180]. In particular, Archon1 could be used to follow the development of these cell types through differentiation, maturation, etc or during disease progression[173,180]. In addition, while we currently transduce CMs with AAVs expressing Archon1, lentiviral particles could additionally be used to create stable cell lines expressing Archon1 for characterization through iPSC-differentiation, development, or integration into living tissue.

Finally, Archon1's capability to monitor CMs in both 2D and 3D environments could assist in the development and evaluation of more functionally mature, biologically-relevant engineered cardiac tissues.

### 3.6 Limitations of the Study

Photobleaching is often a concern for all optical imaging techniques that deploy fluorescent indicators. However, under 5 minutes of continuous imaging, Archon1 demonstrated robust monitoring of membrane voltage with no change in SNR, which we expect could extend to tens of minutes. For experiments requiring hours of continuous monitoring, periodic imaging of short durations may be necessary. As GEVIs are engineered to become more sensitive, less light illumination power will be needed to achieve the same SNR and longer imaging studies could be conducted.

In addition, due to current limitations in camera speed, in order to capture an entire CM (typically ~50-100μm across) within the field of view, the acquisition rate must be limited to

~100Hz. We have previously shown that Archon1 and its variants can follow millisecond time scale events, such as neuron APs, with high temporal precision at acquisition rates up to 1kHz[197,211]. As camera technology continues to improve, we hope to be able to conduct such high speed imaging of larger fields of view containing populations of CMs. Like all non-ratiometric GEVIs or VSDs, Archon1 does not report absolute values of membrane potential, and SNR may vary due to GEVIs expression levels across individual cells. However, relative membrane potential is still valuable for comparing AP dynamics between different biological states.

In conclusion, Archon1, with its the diverse functionality and its simple one-photon widefield imaging setup, can be easily adapted for investigating a variety of avenues in cardiac biology and relevant pathology.

### 3.7 Supplemental Data

**Video 3.S1.** Video of iPSC-derived CM expressing Archon1 spontaneously beating. Scale bar, 25μm. Related to Figure 3. 1B, C.

**Video 3.S2.** Video of iPSC-derived CM expressing Archon1 spontaneously beating imaged in GFP channel. Scale bar, 25μm. Related to Figure 3.1B,C.

**Video 3.S3.** Video of Di-8-ANEPPS treated iPSC-derived CM, paced at 0.5Hz. Scale bar, 25μm. Related to Figure 3.1H.

**Video 3.S4.** Video of iPSC-derived CM expressing Archon1 on Day 62 post-infection, paced 1.0Hz. Scale bar, 25μm. Related to Figure 3. 1.

**Video 3.S5.** Video of Engineered Cardiac Tissue spontaneously beating. Scale bar, 250μm. Related to Figure 3.3A (left).

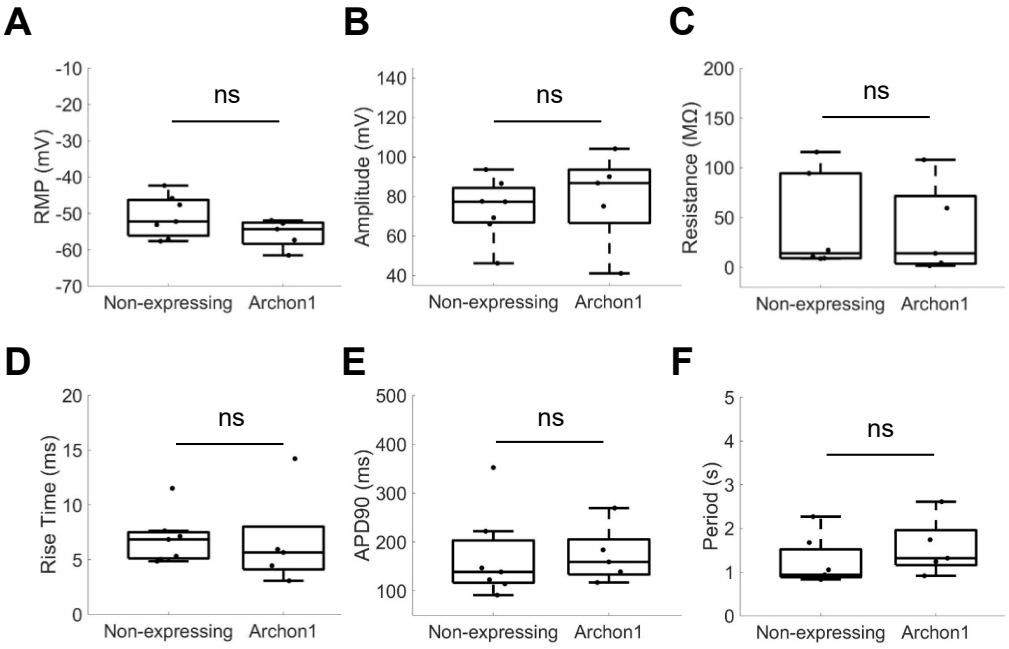


**Figure 3.S1.** Quantification of electrophysiological properties of non-expressing CMs compared to Archon1-expressing CMs. Related to **Figure 3.2**. (**A**) Resting membrane potential (RMP, n = 7, 5 cells, respectively), ns, $p > 0.05$ in two-tailed t-test. (**B**) Action potential amplitude (n = 7, 5 cells, respectively), ns, $p > 0.05$ in two-tailed t-test. (**C**) Resistance (n = 6, 5 cells, respectively), ns, $p > 0.05$ in two-tailed t-test. (**D**) Rise time (n = 7, 5 cells, respectively), ns, $p > 0.05$ in two-tailed t-test. (**E**) APD90 (n = 7, 5 cells, respectively), ns, $p > 0.05$ in two-tailed t-test. (**F**) Beat period (n = 7, 5 cells, respectively), ns, $p > 0.05$ in two-tailed t-test. Box plots represent 25$^{th}$ to 75$^{th}$ percentiles, with whiskers extending 1.5x the interquartile range, horizontal line represents median, each dot represents data from a single cell.

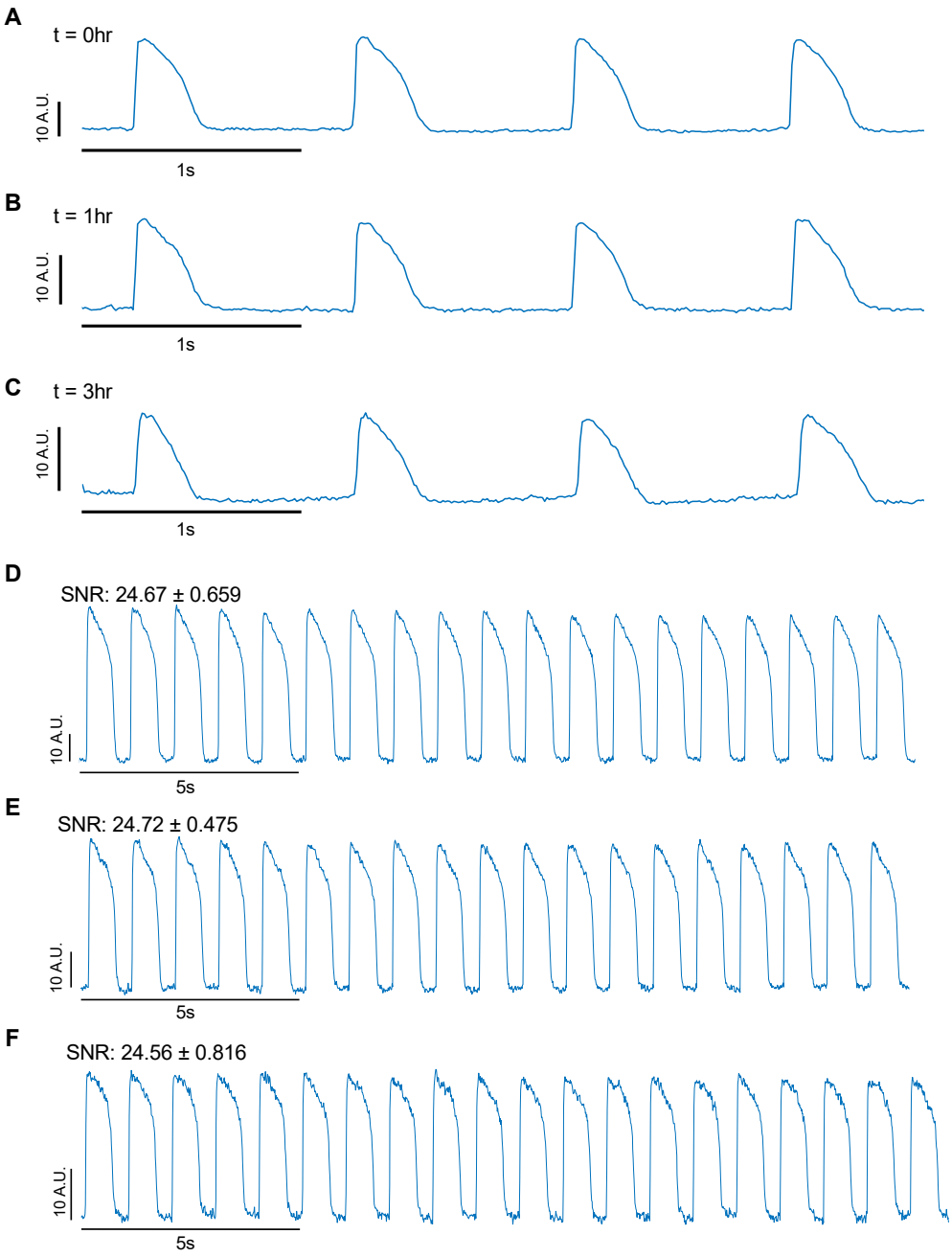


**Figure 3.S2.** Archon1 allows for robust measurement of action potentials under repeated and long-duration imaging. Related to **Figure 3.2H**. (**A-C**) Representative optical voltage trace for an example CM recorded repeatedly at (**A**) t = 0hr, (**B**) t = 1hr, (**C**) t = 3hr. Electrically paced at 1Hz. Quantification of SNR for all repeatedly recorded cells in **Figure 3.2H**. (**D-F**) Archon1 optical voltage trace for CM recorded for 5 minutes continuously, electrically paced at 1Hz. (**D**) 0-20s; SNR: 24.67±0.659, mean±standard deviation, (**E**) 100-120s; SNR: 24.72 ±0.475, mean±standard deviation, (**F**) 280-300s; SNR: 24.56 ±0.816, mean±standard deviation. $p = 0.734$, one-way ANOVA. All optical traces obtained at Image acquisition rate of 100Hz.

# Chapter 4: Extracellular matrix alignment directs provisional matrix assembly and 3D fibrous tissue closure

The work in this chapter represents a published article in a peer reviewed journal of which I am the first author. In this Chapter of the thesis, I removed the complexities of the cardiac system and simply studied the response of fibroblasts during injury on both highly aligned and non-aligned ECM in an engineered tissue system. https://doi.org/10.1089/ten.tea.2020.0332

## 4.1 Abstract

Gap closure is a dynamic process in wound healing in which a wound contracts and a provisional matrix is laid down to restore structural integrity to injured tissues. The efficiency of wound closure has been found to depend on the shape of a wound, and this shape dependence has been echoed in various in vitro studies. While wound shape itself appears to contribute to this effect, it remains unclear whether the alignment of the surrounding extracellular matrix (ECM) may also contribute. In this study, we investigate the role both wound curvature and ECM alignment have on gap closure in a 3D culture model of fibrous tissue. Using microfabricated flexible micropillars positioned in rectangular and octagonal arrangements, seeded 3T3 fibroblasts embedded in a collagen matrix formed microtissues with different ECM alignments. Wounding these microtissues with a microsurgical knife resulted in wounds with different shapes and curvatures that closed at different rates. Observing different regions around the wounds, we noted local wound curvature did not impact the rate of production of provisional fibronectin matrix assembled by the fibroblasts. Instead the rate of provisional matrix assembly was lowest emerging from regions of high fibronectin alignment and highest in the areas of low matrix alignment. Our data suggest that the underlying ECM structure affects the shape of the wound as well as the ability

of fibroblasts to build provisional matrix – an important step in the process of tissue closure and restoration of tissue architecture. The study highlights an important interplay between ECM alignment, wound shape, and tissue healing that has not been previously recognized and may inform approaches to engineer tissues.

**Keywords:** provisional matrix assembly, fibronectin, ECM alignment, wound closure, tissue repair

#### 4.1.1 Impact Statement

Current models of tissue growth have identified a role for curvature in driving provisional matrix assembly. However, most tissue repair occurs in fibrous tissues with different levels of ECM alignment. Here we show how this underlying ECM alignment may affect the ability of fibroblasts to build new provisional matrix, with implications for in vivo wound healing and providing insight for engineering of new tissues.

## 4.2 Introduction

The assembly of provisional matrix is a critical step in wound closure and the formation of tissue de novo. During the repair of full-thickness wounds, fibroblasts first migrate into the wound area and deposit extracellular matrix (ECM) proteins such as fibronectin. These proteins serve as a template for other cell types including endothelial cells and immune cells to migrate on[44–46,226]. Later, epithelial cells use this provisional matrix or granulation tissue as a substrate to migrate over and cover the wound bed to complete closure[227–229]. While it has been reported that insufficient or delayed formation of granulation tissue can lead to impaired gap closure and delayed re-epithelialization[229,230], the factors that drive the rate of granulation tissue formation remain elusive. Understanding how to modulate this rate of tissue assembly is not only important in the context of wound healing, but also in the biomanufacturing of engineered tissues.

In clinical settings, wound closure rates correlate with the shape of a wound, an observation that has been echoed in several studies of re-epithelization[231–233]. For example, in epithelial monolayers, pre-patterned gaps with concave shapes close faster compared to those with convex shapes[234,235]. The increased rate of closure in regions of high curvature stems from the emergence of contractile actomyosin rings spanning multiple epithelial cells that pull the wound margins closer[236–238]. Curvature also has also been suggested to control new matrix formation by fibroblasts, which lack these multicellular contractile rings, in models of tissue growth into pores[239–241].

While curvature of the wound edge has been associated with wound closure rates, wound shape and healing rate are also dependent on the local organization of the underlying ECM. For example, in surgical settings, incisions made across the natural orientation of collagen fibers in the dermis results in wide open gaps that heal poorly, whereas by cutting along the direction of natural ECM alignment, incisions gape less, leading to faster healing and less scarring[232,242]. Although the mechanism underlying this clinical practice is not well understood, there is a clear evidence that ECM alignment guides migratory and contractile processes of fibroblasts that are crucial for wound closure[34,36,38,243]. However, how this ECM alignment and curvature affect the assembly of new tissue, such as granulation tissue or the generation of new tissue, remains to be explored.

To study how curvature and ECM alignment may influence tissue closure by fibroblasts, we use a previously established model of 3D stromal gap closure, wherein fibroblasts in engineered collagen-based microtissues[244] are injured and then assemble a provisional fibronectin template to close the gap. Here, we use an approach to change the shape of the microtissues, to either rectangular or octagonal, to affect the alignment of the ECM[245,246], and show that ECM alignment may locally act as a negative regulator of provisional matrix assembly and thus modulating the rate of new tissue formation.

## 4.3 Materials and Methods

### 4.3.1 Cell Preparation and Culture

NIH 3T3 cells (ATCC) were maintained in high glucose DMEM (Corning) containing 10% Bovine Serum and 1% Penicillin Streptomycin solution (Gibco). Cells were used between passages 5 and 15.

### 4.3.2 Microtissue Seeding

Rectangular and octagonal microtissues were prepared as previously described[146,245]. Briefly, polydimethylsiloxane micro-fabricated tissues gauges (μTUGs) were prepared by molding from SU-8 masters[146,245]. μTUG devices were UV sterilized, then treated with 0.02% Pluronic F127 (Sigma) for 15 minutes to prevent cell and extracellular attachments. 3T3 cells were dissociated from cell culture plates and suspended in a 2mg/ml Collagen I, Rat Tail (Corning) hydrogel solution at a concentration of 1million/ml. Cell suspensions were centrifuged into devices and excess was removed before polymerization at 37°C for 10 minutes. Microtissues were maintained in high glucose DMEM containing 10% Bovine Serum and 1% Penicillin Streptomycin solution.

To visualize collagen matrix of microtissues, 5% (w/w) Alexa Fluor 555 conjugated Collagen I, (Thermo Fisher), was added to the cell suspension before device seeding. To visualize fibronectin matrix within microtissues, 8 μg/ml of Alexa Fluor 488 (Thermo Fisher) conjugated human fibronectin (isolated from human plasma) was added to media during the first 24 hrs of tissue formation. 24 hrs after devices were seeded, a diamond dissecting knife (type MDL, Electron Microscopy Systems, #72029) mounted on a XYZ micromanipulator was used to create full-thickness incisions in the centers of the microtissues. Incisions were oriented from top to bottom.

### 4.3.3 Time-lapse Microscopy and Closure Rate Measurements

For wide-field time-lapse imaging, phase contrast and fluorescent images were captured every 30 minutes for over 16 to 20 hrs. They were recorded with a Photometrics Evolve 16-bit electron-multiplying CCD camera (Photometrics) and an A-Plan 10x objective mounted on a Nikon Ti Eclipse (Nikon Instruments, Inc.) microscope maintained at 37°C at 5% $CO_2$. Phase contrast images were used to measuring gap area every 2 hrs over the indicated time, and closure rates were calculated using the slope from a Least Squares Regression Line that was fitted through the data for each individual tissue. The data were truncated if closure completed before the indicated time, or if the tissue ruptured or tore. Ellipsoidal shapes were fitted to the wound boundaries in ImageJ. The major and minor axes of these ellipses were used to parametrize the wounds' shapes, and the ellipses were also used for calculations of the wounds' curvature and eccentricity.

### 4.3.4 Confocal Microscopy

To visualize ECM, microtissues with Alexa-555 tagged collagen and Alexa-488 fibronectin were imaged on a Leica SP8 confocal microscope with a Leica 40x water objective and Leica LAS X imaging software. For fiber analysis, z stacks of microtissues with Alexa-488 tagged fibronectin were imaged on a Yokogawa CSU-21-Zeiss Axiovert 200M inverted spinning-disk microscope with a Zeiss 40x water objective and Evolve EMCCD camera (Photometrics). ImageJ and the Pairwise Stitching plugin[247] were used to stitch images together and then maximum projections were used for analysis.

### 4.3.5 Fiber Analysis

Analysis of fibronectin fibers was performed using an established MATLAB code[245] based on the FibrilTool method[248] to measure fiber orientation and anisotropy. Analysis was

performed on 30 μm x 30 μm regions tangent to the top and side edge of the bulk tissue adjacent to the wound edge.

### 4.3.6 Computational Model

Computational modeling was performed using FEniCS[249,250], an open source finite element analysis computing platform. The microtissue was approximated as a random fiber network. The random fiber network finite element mesh was initialized with the Gmsh mesh generator[251]. Each domain contained approximately 1,100-1,400 fibers of length 100 μm with initial fiber angle sampled from a uniform distribution. In the rectangular geometry, a 10 μm by 300 μm rectangular wound was initialized in the center of the domain. In the octagonal geometry, a 10 μm by 150 μm rectangular wound was initialized in the center of the domain. In both domains, the micropillar attachment sites were simulated as Dirichlet boundary conditions. The microtissue fibers were approximated as a homogeneously contracting Neo-Hookean material where homogeneous volumetric contraction was applied up to a dimensionless shrinkage of 0.6 following the standard multiplicative decomposition model for biological tissue growth(and shrinkage)[252]. Geometry set up and subsequent simulation analysis and plotting were performed with Python[253], Numpy[254], and Matplotlib[255]. For post processing, anisotropy was computed directly from the deformed geometry of the finite element mesh[248] using 50 μm square ROIs adjacent to the wound edge. To account for the effect of different random fiber distributions, one hundred simulations were performed and analyzed for each geometry.

### 4.3.7 Statistical Analysis

Two-tailed Student's t-tests were used for all statistical analysis, unless where otherwise indicated. For statistical comparisons within the same tissue, a paired t-test was

used, while between different tissues, an unpaired t-test was used. Significance values are indicated as *p≤0.05, **p≤0.01, ***p≤0.001.

## 4.4 Results

### 4.4.1 Closure of elliptical gaps in fibrous microtissues

To investigate fibrous tissue closure in highly aligned matrices, we generated microtissues composed of NIH 3T3 fibroblasts in a collagen type I matrix formed around flexible polydimethylsiloxane (PDMS) pillars that were spaced in a rectangular pattern with a 4 to 1 aspect ratio[245] (Figure 4.1a). After the tissue was compacted around the pillars (18-24 hr after seeding), an incision was cut in the center of the tissue using a microdissection knife. Upon injury, the incision opened to form an elliptical shaped gap (Figure 4.1b, left). Over the next 20 hrs, this gap spontaneously closed in a linear fashion (Figure 4.1b, c) with a constant rate of change in gap area of -627 ± 34 $\mu m^2$/hr (mean ± SEM) (Figure 4.1c, Video 4.S1) and had a slight increase in eccentricity between the start and 10 hrs into healing from 0.958 ± 0.003 to 0.968 ± 0.003 (mean ± SEM, $p = 3.0 \times 10^{-4}$, Figure 4.1d). To investigate how the elongated shape of the tissue and elliptical gap affect the dynamics of tissue closure, we measured the change in length of the major and minor axes of the gap over time and calculated their rates of change. We found that closure rate of the major axis was 9.3 ± 0.7 μm/hr (mean ± SEM), 3.4x faster than the closure rate of the minor axis (2.7 ± 0.1 μm/hr, mean ± SEM, $p = 1.1 \times 10^{-12}$, Figure 4.1e, f). These data suggest that the overall tissue structure dictates the gap closure process, with significantly faster closure rates along the major axis.

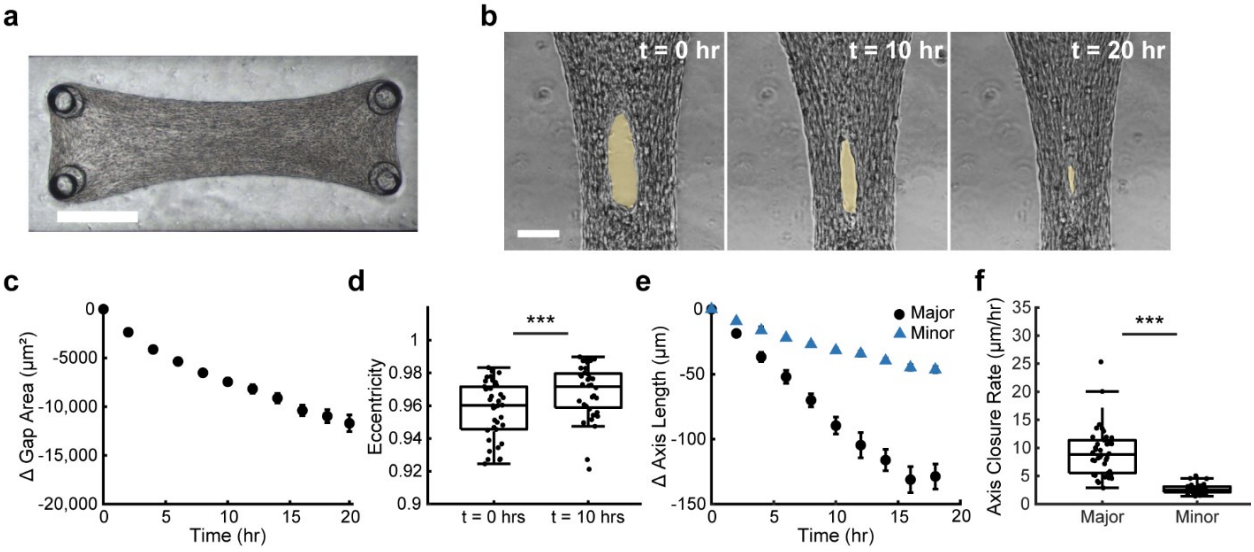


**Figure 4.1. Closure of elliptical gaps in fibrous microtissues.** a) NIH 3T3 microtissue 24 hours post-seeding, before injury (Scale bar = 300 μm). b) Injured microtissue spontaneously closing over time at 0, 10, 20 hrs post-injury (Scale bar = 100 μm). Yellow regions indicate open gap. c) Change in gap area over time, averaged over three separate experiments (n = 38 tissues) d) Eccentricity of open gap after injury and 10 hr into healing, ***: $p < 0.001$, n = 36 tissues. e) Change in major (black circles) and minor (blue triangles) axis length of gap over time (n = 38 tissues). f) Linear rate of axes change throughout closure process, ***: $p < 0.001$, n =38 tissues. Box plots represent 25$^{th}$ to 75$^{th}$ percentiles, with whiskers extending 1.5x the interquartile range and horizontal lines showing the medians.

### 4.4.2 Assembly of fibronectin template occurs primarily along the major axis and is not correlated with the curvature of the wound edge

As previously described in Sakar et al[244], gap closure in this model system is driven by two mechanisms: contractility dependent compaction and the building of new provisional fibronectin matrix that fills the gap (Figure 4.2a). To visualize these two processes, fluorescently labeled collagen and fibronectin were added during tissue formation and imaged hourly throughout the healing process. At high magnification (40x), fluorescently labeled collagen and fibronectin were seen in the bulk tissue. Fibronectin populated with cells was also observed within the gap, showing the provisional matrix

assembled by cells during closure (Figure 4.2b, top). Since the field of view was limited at high magnification, we explored whether the provisional matrix could be visualized at lower magnification (10x) to enable quantification of compaction and provisional matrix assembly using images that show the tissue in a larger field of view. At this magnification, the fluorescent signal from fibronectin and collagen in the bulk tissue overlapped, but the faint fibronectin signal from the provisional matrix was not detectable (Figure 4.2b, bottom). Due to this limitation, we used brightfield images as a proxy for total closure instead, and subtracted these images from the fluorescent images showing the bulk tissue. At this magnification, the area of new provisional matrix deposition was identified as new material visible by phase but not detectable in the fluorescent imaging (Figure 4.2c). Thus, the boundaries for these regions could be calculated (Figure 4.2c, yellow dotted line bounding the fluorescently tagged collagen; green region showing area of new provisional matrix). Using this method, we tracked compaction of the original tissue boundary and new provisional matrix over time (Figure 4.2d, e). Given the differences in major and minor axis closure rates previously observed, we also compared the rates of compaction and new matrix assembly specifically in these regions (Figure 4.2f). The total axis closure rate was significantly different between the major and minor axes, 19.1 ± 1.0 μm/hr and 4.1 ± 0.2 μm/hr, respectively (mean ± SEM, $p = 1.2 \times 10^{-7}$). We note these rates are higher than in Figure 4.1f, we believe this may be a result of the addition of the tagged fibronectin during the formation process. Separating the contributions from compaction and fibronectin matrix growth, we observed that while compaction between both axes was not significantly different (Major: 4.2 ± 0.9 μm/hr, Minor: 2.6 ± 0.2 μm/hr, mean ± SEM, $p = 0.074$), fibronectin matrix growth was higher in the major axis compared to the minor axis (Major: 14.9 ± 0.9 μm/hr, Minor: 1.6 ± 0.2 μm/hr, mean ± SEM, $p = 2.5 \times 10^{-7}$). These data suggest

the difference seen in total closure was due to regional differences in provisional matrix, rather than compaction of the tissue. Therefore, moving forward, we focused on understanding the drivers for differential growth of the fibronectin matrix in our model system.

As studies have highlighted the role of curvature on the rate of provisional matrix growth[239–241,256], we investigated if curvature could be used to explain the rates found in this model. Since the point of maximum curvature occurs where the major axis crosses the wound edge, we analyzed the curvature and the provisional matrix growth over time in this region, heretofore referred to as "Top" (Figure 4.2g). Over the course of closure, curvature increased at a rate of 0.29 $\mu m^{-1} hr^{-1}$ (from Least Squares Regression Line: $y = 0.029x + 0.05$, $R^2 = 0.98$), while the rate of provisional matrix growth from the point of maximum curvature remained constant. Given this weak correlation between curvature and provisional fibronectin matrix growth, we set out to investigate other parameters that may explain the axial difference in assembly of the provisional fibronectin matrix in this model of tissue closure.

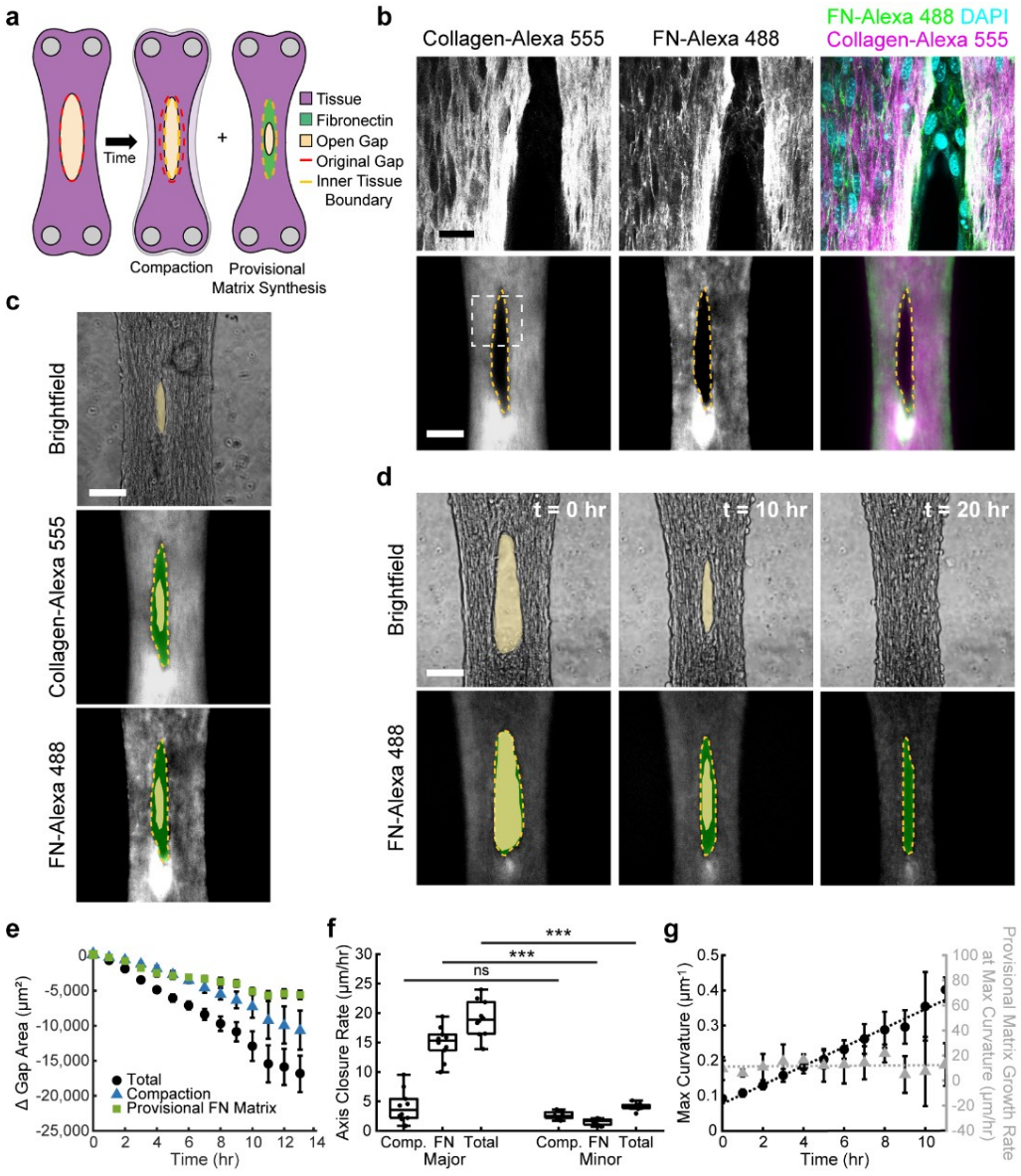


**Figure 4.2. Assembly of fibronectin template occurs primarily along the major axis and is not correlated with the curvature of the wound edge.** a) Schematic of contributions of both tissue compaction and provisional fibronectin matrix to closure process. b) Tissue at 10 hrs post-injury labeled with Collagen-Alexa 555 (magenta), Fn-Alexa 488 (green), nuclei (cyan) at 40x confocal (top, scale bar = 25 μm) and 10x widefield (bottom, scale bar = 100 μm). Dashed yellow line indicates the inner tissue boundary. White dashed box indicates 40x field of view. c) Widefield image of microtissues 10 hours post-injury. Brightfield (top) with yellow region indicating open gap. Collagen-Alexa 555 (middle) and Fn-Alexa 488 (bottom) with yellow region overlaid. Dashed yellow line indicates inner tissue boundary, green region indicates provisional fibronectin matrix. d) Widefield imaging of tissue with FN-Alexa 488 after injury at t = 0, 10, 20 hrs. Brightfield (top) with yellow region indication total gap, Fn-Alexa 488 (bottom), with yellow region overlaid. Dashed yellow line indicates inner tissue boundary, green region indicates provisional fibronectin matrix. e) Change in gap area over time; total (black circles) broken down into the contribution of

compaction (blue triangles) and fibronectin provisional matrix (green squares) (n = 10). f) Major and minor axes linear closure rates broken down into the contribution of compaction and fibronectin, ***: $p < 0.001$, *ns*: $p > 0.05$, n = 10. Box plots represent 25$^{th}$ to 75$^{th}$ percentiles, with whiskers extending 1.5x the interquartile range and horizontal lines showing the medians. g) Maximum curvature of gap over time (left axis, black circles, Least Squares Regression Line: y = 0.029x + 0.05, $R^2$ = 0.98) and provisional matrix growth rate at point of maximum curvature over time (right axis, gray squares, Least Squares Regression Line: y = 0.1082x + 11.27, $R^2$ = 0.0067).

### 4.4.3 Local fibronectin alignment at gap edge correlates with the assembly of fibronectin provisional matrix

Given that fibroblast-fibronectin interactions are critical for closure in this model system[244], we tested whether ECM alignment is correlated with the deposition of provisional matrix in the gap area. Using a MATLAB code developed based on the FibrilTool algorithm[245,248], we measured fiber orientation and anisotropy (degree of alignment), in the Top region and the region where the minor axis crosses the wound edge (heretofore referred to as the "Side" of the wound). Due to artifacts from excess tissue material from the incision (Figure 4.3a, white arrowhead), only the top edge and one side of the gap were analyzed. For both regions, 0° is defined as the tangent line to the wound edge for the angle of orientation measurements. Fibronectin fibers were oriented parallel to the wound edge in the side regions, whereas fibronectin fibers in the top regions were oriented perpendicular to the wound edge (Figure 4.3b). The anisotropy of the fibrous matrix was significantly (p = 0.036) lower in the top regions (0.19 ± 0.02, mean ± SEM) compared to the side regions (0.26 ± 0.05, mean ± SEM, Figure 4.3c). Together, these data demonstrate that fibronectin fibers are more aligned at the side edge of the wound compared to the top edge.

To understand how fiber alignment and orientation are fundamentally linked to the tissue shape, we built a computational model of ECM fibers using the Finite Element

Method[252] (Supplemental Figure 4.1). In the stress-free reference configuration, we initialize randomly oriented ECM fibers. Then, we applied homogeneous contraction and observed how ECM fiber alignment emerged in the deformed configuration due to the interaction between tissue contraction, tissue geometry, and boundary conditions. A similar fiber analysis as described above for the microtissues was performed for 100 simulations of the model. Confirming our experimental findings, the simulations showed an increased fiber anisotropy at the side of the gap compared to the top (Anisotropy: Top: 0.46 ± 0.01, Side: 0.55 ± 0.01, mean ± SEM, $p = 3.3 \times 10^{-7}$, Figure 4.3e, f). Not only do these findings validate the computational model, but they also suggest that contractility is sufficient to model ECM alignment in our system. To determine the relationship between fiber anisotropy and provisional matrix growth, we plotted provisional matrix length at 10 hrs as a proxy for provisional matrix growth (derived from experimental data, Figure 4.2d) and local tissue anisotropy (from computational model) as a function of angle around the gap (Figure 4.3g). Interestingly, regions with lower fiber anisotropy showed more provisional matrix growth compared to regions with high fiber anisotropy, therefore, suggesting that provisional matrix assembly in the gap is inversely correlated to how aligned the ECM of the adjacent tissue is.

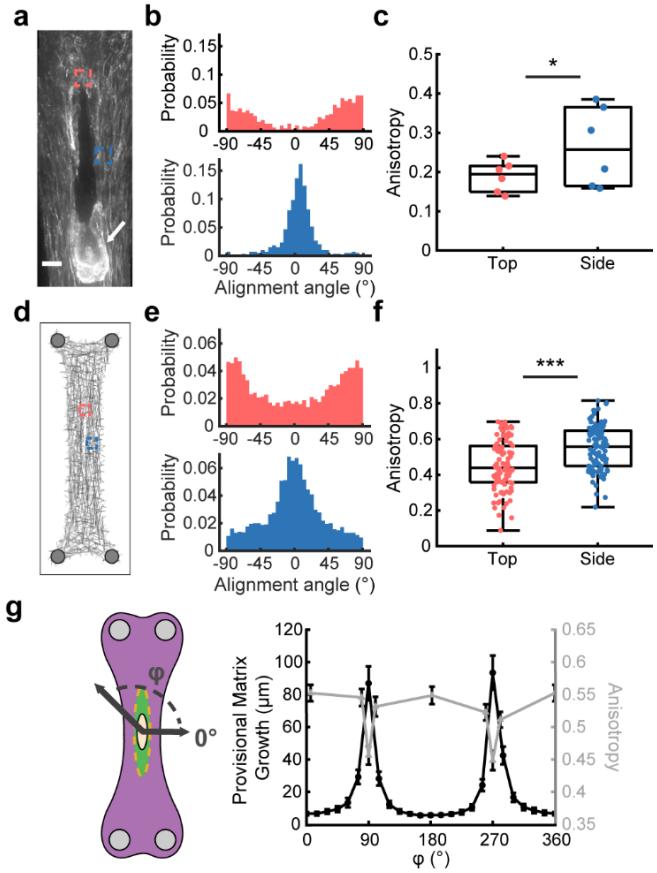


**Figure 4.3. Local fibronectin alignment at gap edge correlates with the assembly of fibronectin provisional matrix.** a) Maximum projection of tissue (40x) with Fn-Alexa 488, fixed 10 hrs post-injury (Scale bar = 30 μm). Regions of analysis (30 μm x 30 μm) and orientations for fibronectin fiber alignment angle and anisotropy (Fig 4.3b,c) are shown for Top (red) and Side (blue) edges. White arrow indicates excess tissue from incision. b) Alignment angle for corresponding regions: top (top) side (bottom) shown in Fig 4.3a (n = 6). c) Average anisotropy for regions shown in 3a, *: $p < 0.05$, n = 6. d) Computational model of injured tissue. Regions of analysis (50 μm x 50 μm) are shown for top (red) and side (blue) edges. e) Fiber alignment angle for regions specified in 3d for 100 simulations. f) Average fiber anisotropy in regions specified in 3d for 100 simulations, ***: $p < 0.001$. g) Radial provisional matrix length at 10 hrs (from experimental data, left axis, black circles) and fiber anisotropy for 8 regions (50 μm by 50 μm) around gap from 100 simulations of model (right axis, gray triangle). The width of bins for histograms in 3b, e is 5°. Box plots represent 25$^{th}$ to 75$^{th}$ percentiles, with whiskers extending 1.5x the interquartile range, and horizontal lines represent medians.

### 4.4.4 Octagonal tissues with reduced matrix alignment exhibit greater and more uniform fibronectin growth around the gap

To elaborate further the hypothesis that ECM anisotropy affects provisional matrix assembly, we investigated wound closure in octagonal microtissues which have an isotropic fiber alignment[245] (Figure 4.4a). Upon incision, the gap opened up in a more circular shape compared to the highly elliptical shape in the rectangular tissues (Figure 4.4b), and closed spontaneously (Figure 4.4c, Video 4.S2). As with the rectangular tissues, we measured the closure rates of the gap axes over time (Figure 4.4d). Having established a wound closure model in isotropic microtissues, we investigated the contribution of compaction and provisional matrix assembly along the horizontal and vertical axes. In contrast to the rectangular microtissues, the horizontal axis closed slightly faster than the vertical axis, 9.1 ± 0.9 μm/hr and 7.8 ± 0.6 μm/hr, respectively (mean ± SEM, $p = 4.9 \times 10^{-3}$, Figure 4.3e). Both compaction and provisional fibronectin matrix growth were significantly different between both axes, but overall the differences were much subtler than in the rectangular tissues (Compaction: Horizontal: 2.8 ± 0.3 μm/hr, Vertical: 3.8 ± 0.6 μm/hr, mean ± SEM, p = 0.042, Fibronectin: Horizontal: 6.3 ± 0.8 μm/hr, Vertical: 4.0 ± 0.4 μm/hr, mean ± SEM, $p = 2.3 \times 10^{-3}$). These differences might be caused by the cutting direction, which introduced some degree of anisotropy into the system.

As anticipated, the orientation of the fibronectin fibers and anisotropy was not as different when comparing the top and side edges of wounds (Figure 4.4 f-h). Although initially oriented isotropically[245], fibronectin fibers tend to align parallel to the wound edge after injury (Figure 4.4g) with similar anisotropy values for top (0.17 ± 0.01, mean ± SEM) and side regions (0.19 ± 0.02, mean ± SEM, p = 0.27, Figure 4.4h). The rearrangement of fibers at the wound edge was also captured by the computational model (Figure 4.4i) with

the top and sides having similar fiber orientations both parallel to the wound edge (Figure 4.4j). In contrast to the experimental model, the computational model predicted a slightly different fiber anisotropy between the top and side regions, 0.37 ± 0.01 and 0.42 ± 0.01, respectively (mean ± SEM, $p = 5.0 \times 10^{-5}$, Figure 4.4k).

However, these anisotropies were both lower than the Side region of the rectangular tissues (Top of octagon to side of rectangle: $p = 1.6 \times 10^{-20}$, Side of octagon to side of rectangle: $p = 5.3 \times 10^{-11}$). To investigate if local ECM anisotropy was also inversely correlated with provisional matrix assembly in octagonal microtissues, provisional matrix length for tissues 10 hrs into healing was plotted vs position around the wound along with fibronectin anisotropy from the model (Figure 4.4l). Unlike rectangular tissues where the length of the provisional template spiked adjacent to regions with low anisotropy, the length of the provisional matrix in octagonal microtissues was more uniform around the gap, with only a drop at 270° corresponding to the bottom of the incision where excess ECM from the incision was present.

Given that the assembly of a fibronectin template occurred uniformly around the gap in octagonal tissues and predominately along the long axis in rectangular tissues, we hypothesized that gap closure depends on the overall tissue geometry. Indeed, in a side-by-side comparison, wounds in octagonal tissues showed higher total area of provisional matrix at 10 hrs into the healing, 8330 ± 710 $\mu m^2$ vs. 5730 ± 926 $\mu m^2$ (mean ± SEM, $p = 0.029$, Figure 4.4m). To compare closure rates, we used the closure rate for the first 10 hours, since after this time point closure slowed down in octagon tissues (Fig 4.4c). Octagons (1400 ± 120 $\mu m^2$/hr) had almost double the closure rate of rectangles (750 ± 49 $\mu m^2$/hr, mean ± SEM, $p = 1.5 \times 10^{-7}$, Figure 4.4n). Together, these data suggest that the lower alignment found in the octagonal tissues enabled more provisional matrix assembly and overall faster healing

rates compared to the rectangular tissues, where highly aligned edges may have impaired the assembly of new provisional matrix.

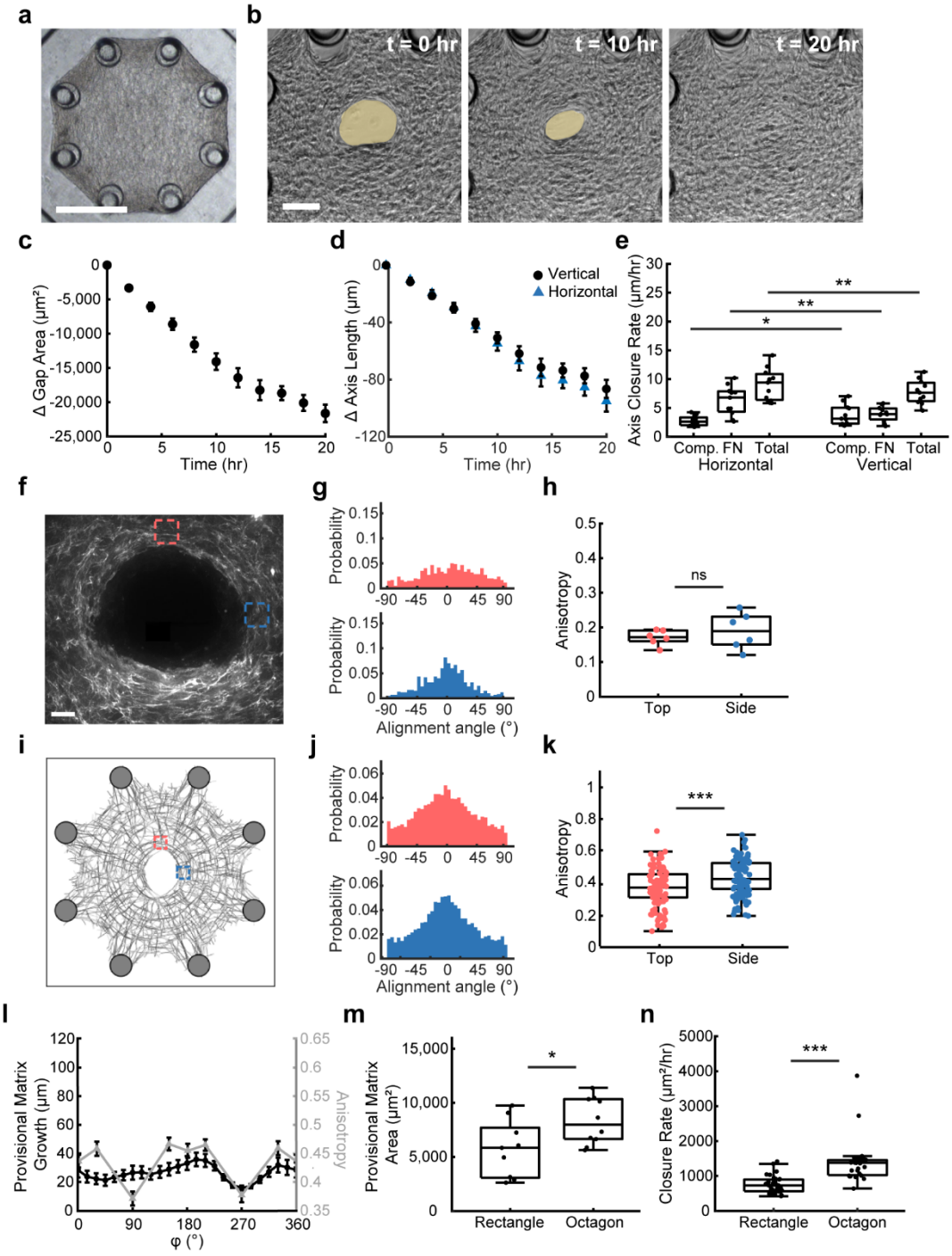


**Figure 4.4. Octagonal tissues with reduced matrix alignment exhibit greater and more uniform fibronectin growth around the gap.** a) Octagonal microtissue 24 hours post-seeding, before injury (Scale bar = 300 μm). b) Injured microtissue spontaneously closing over time at 0, 10, 20 hrs post-injury (Scale bar = 100 μm). Yellow region indicates open gap. c) Change in gap area over time for three separate experiments (n = 27 tissues) d) Change in vertical (black circles) and horizontal (blue triangles) axis length of gap over time (n = 27 tissues). e) Major and minor axes

linear closure rates broken down into the contribution of compaction and fibronectin, **: $p < 0.01$, *: $p < 0.05$, n = 10. f) Maximum projection of tissue (40x) with Fn-Alexa 488, fixed 10 hrs post-injury. Regions of analysis (30 μm x 30 μm) and orientations for fibronectin fiber alignment angle and anisotropy (Fig 4.4g,h) are shown for top (red) and side (blue) edges. (Scale bar = 30 μm) g) Alignment angle for corresponding regions: top (top) side (bottom) shown in Fig 4.4f (n = 6). h) Average anisotropy for regions shown in 4.4f, *ns*: $p > 0.05$, n = 6. i) Computation model of injured tissue. Regions of analysis (50 μm x 50 μm) are shown for top (red) and side (blue) edges. j) Fiber alignment angle for regions specified in 4.4i for 100 simulations. k) Average fiber anisotropy in regions specified in 4.4i for 100 simulations, ***: $p < 0.001$. l) Radial provisional matrix length at 10 hrs (from experimental data, left axis, black circles) and fiber anisotropy for 8 regions (50 μm by 50 μm) around gap from 100 simulations of model (right axis, gray triangle). m) Provisional matrix area at 10 hrs for rectangular and octagonal tissues, *: $p < 0.05$ (n = 9, 10). n) Closure rates for the first 10 hrs for rectangular and octagonal tissues, ***: $p < 0.001$ (n = 38, 27). The width of bins for histograms in 4.4g, j is 5°. Box plots represent 25$^{th}$ to 75$^{th}$ percentiles, with whiskers extending 1.5x the interquartile range, horizontal line represents median.

**4.5 Discussion**

Clinical observations and early studies in rabbit models have shown that wound shape is a critical determinant for closure[231–233,242]. To understand how wound shape affects the cellular and mechanical mechanisms underlying tissue repair, bioengineered in vitro models have been developed wherein gaps with different shapes are patterned in epithelial monolayers using stamping techniques[234,235] or cut with laser light[257]. Recently, 3D scaffolds were used to study tissue growth under tension[256] and fabricated microcontainers with different shapes have been used to study gap closure in 3D[258]. While these methods directly control gap geometry, our model system controls wound shape by changing the overall tissue geometry. Thus, similar to cuts in patients, the shape of the gap in our model system depends on the pre-stress of the tissue matrix, which enables studies of the effects of tissue properties surrounding the wound on gap closure *in vitro*.

Another unique feature of this biomimetic in vitro wound healing model is that closure is strongly dependent on the assembly of a provisional fibronectin template[244]. Assembly of provisional fibronectin matrices has also been described in pore filling models[239,240]. In pores with

different geometries, fibroblasts first assemble provisional matrix to make gaps circular before proceeding to fill the gap uniformly. This observation has led to the idea that minimizing surface tension, and as such minimizing curvature, drives the growth of fibronectin matrices in pores with different geometries[239,256,259]. While minimizing surface tension has also been suggested to drive gap closure in fibrous microtissues[260], our study shows that during healing the eccentricity of the gaps and fibronectin tissue growth in rectangular microtissues remains relatively constant whereas curvature increases. Thus, our data suggest that other factors, such as ECM alignment, may add an additional layer of regulation to provisional matrix assembly and gap closure.

While this study reveals a correlation between ECM alignment and provisional matrix growth in gap closure, the impaired provisional matrix growth along the highly aligned edges of rectangular microtissues could be explained by multiple causes. ECM fibers can provide topological cues to direct cell migration along the aligned fibers[36–38,261,262], therefore hindering cells from moving into the gap. Conversely, cells can migrate randomly in less aligned ECMs, as observed in the top region of gaps in rectangular microtissues and in octagonal microtissues, which may facilitate movement into the gap. Alternatively, matrix alignment is inherently linked to augmented tissue stress that is transmitted through the ECM[263–265]. These stresses have been shown to alter the conformation and state of individual fibronectin fibers[40]. Whereas stretch is required for fibrillogenesis, highly stretched fibronectin shows reduced co-localization to other ECM molecules such as collagen type I[39], which may hamper assembly and ingrowth of a provisional matrix. Given the intricate relationships between ECM alignment, contractility, and tissue stress, parsing out the contribution of each factor separately will be a challenging task. Nevertheless, such mechanistic studies are needed to understand how increased ECM alignment affects the assembly of a provisional matrix in wounds.

Computational models are powerful tools to parse out the effect of multiple factors on wound closure. In this study, we used a mechanical fiber model to gain insight in how contractility of the ECM affects ECM alignment after injury. The model correctly predicted the opening of the wound as well as the fiber rearrangement at the wound margin. Interestingly, the model also predicted slightly different anisotropy values for side versus top regions in both rectangular and octagonal tissues, a finding that was not confirmed experimentally in the case of the octagonal tissues. This was predicted in the model because an anisotropic wound was initialized. We note that in our computational model ECM fibers and fiber crosslinks neither re-form nor break. Therefore, unlike the experimental model system, the computational model does not account for stress relaxation caused by tissue remodeling and viscoelastic properties of the collagen gel. We anticipate that this simplification is the major source of inconsistency between the computational model and experiments. However, there were some differences in overall healing and the contribution of compaction and provisional matrix assembly between the two axes of octagonal tissues. Given the overall symmetry of octagonal microtissues, such differences, albeit modest, were unexpected. We speculate that asymmetry in the closure may be associated with the mode of injury. In our experiments, an incision from top to bottom was made with a microdissection knife, and in this process, ruptured tissue accumulated at the bottom side of the tissue may have affected the closure process.

**4.6 Conclusion**

Using a bioengineered model system, we present here a novel in vitro approach to investigate the role of ECM alignment on wound shape and provisional matrix assembly. Our study suggests that ECM alignment can limit the assembly of a provisional template. Harnessing this principle of tissue growth may one day suggest treatments to disrupt local ECM alignment in situ

as a mechanism to improve healing of highly aligned tissues such as tendons and ligaments, or inform new strategies to direct ECM assembly in tissue engineering applications.

## 4.7 Supplemental Data

**Video 4.S1.** Video of rectangular microtissue closing over 20 hrs, with frames taken every 30 min. Related to Figure 4.1.

**Video 4.S2.** Video of octagon microtissue closing over 20 hrs, with frames taken every 30 min. Related to Figure 4.4.

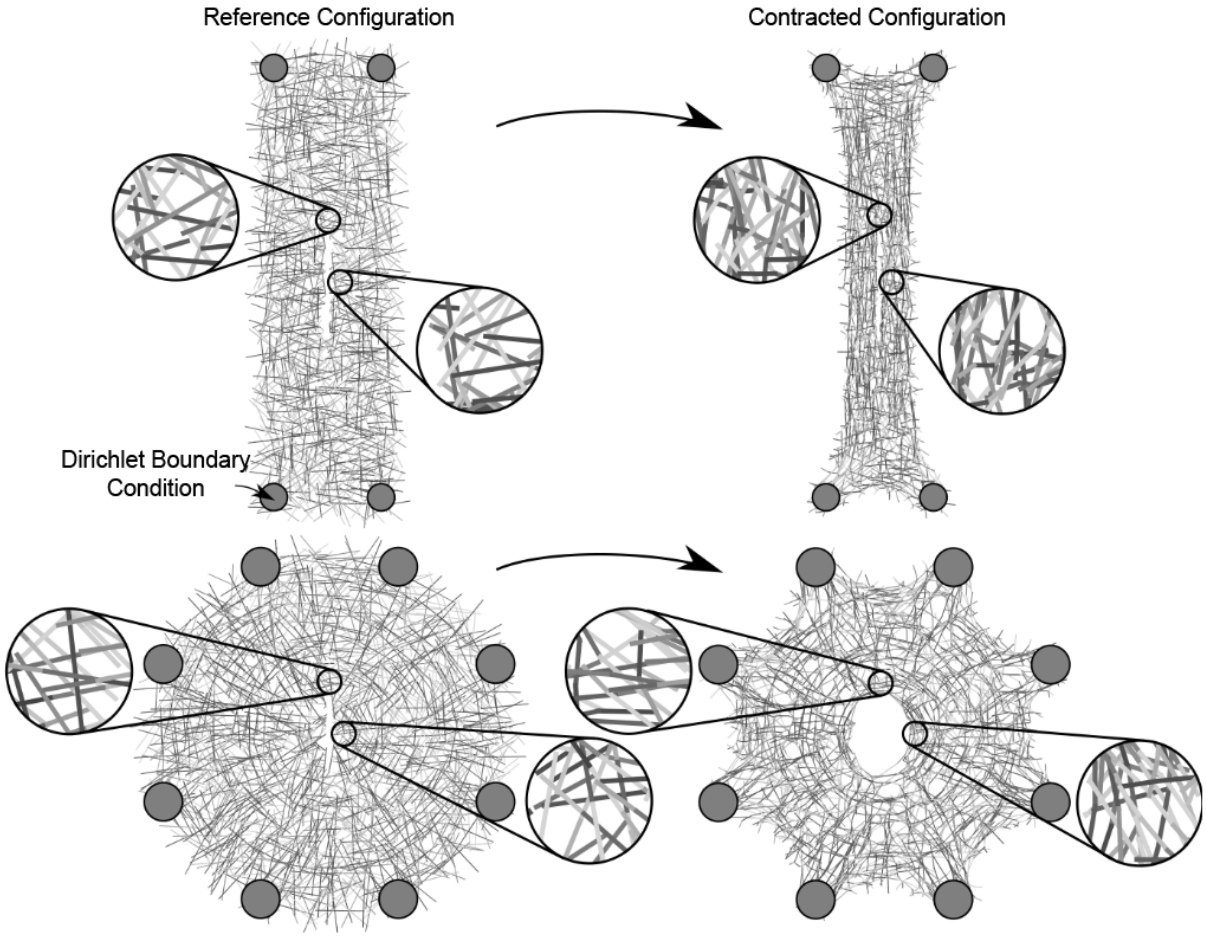


**Figure 4.S1.** Here we show the reference and the contracted (deformed) configurations of representative rectangle (top) and octagon (bottom) domain finite element simulations with injuries. For both domains, the contracted configuration shows a higher degree of fiber alignment than the reference configuration in the area around the wound edge.

# Chapter 5: Investigation into the use of engineered heart tissues to study regeneration

This chapter is a compilation of smaller projects done throughout the course of this dissertation. These early-stage projects both zoom into and build on the complexity of the EHT model presented in Chapter 2 and represent potential future directions of this work. This chapter contains three distinct subchapters which describes preliminary work to 1) track the RNA expression profiles of the cell populations in EHTs over time, 2) vascularize EHTs and 3) utilize EHTs as a system to study the engraftment of new cardiomyocytes for the purpose of heart regeneration.

## 5.1 Single-cell sequencing of engineered heart tissues over time

### 5.1.1 Introduction

To build EHTs which recapitulate *in vivo* tissue and disease processes, characterization of the cell populations within these tissues is necessary. As cells progress through development and disease, the expression profiles of cells within these tissues evolve, furthermore their expression highly impacted by inputs from their surrounding environments (e.g. neighboring cells, mechanical ECM properties, paracine factors, etc). Therefore, when using engineered tissue models to study healthy and diseased tissues it is important to understand the state of the cells within these tissues to contextualize the processes being modeled. For example, in EHT, while the cells and tissues created *in vitro* from iPSCs have many of the characteristics of heart tissue, they are functionally immature compared to those of adult human myocardium, representing more of a neonatal cardiac phenotype[102,103,106]. Another example is the effect of stiffness on fibroblast phenotypes. It has

been shown that when fibroblasts are taken out of tissues and cultured on tissue culture plastic, an environment with a much higher stiffness than tissue ECM, they become activated, expressing contractile proteins like α-SMA[55,56,111]. These changes in cell state need to be recognized when using in vitro models to study disease. Even more importantly, in order to create EHTs with the potential for implantation, it is of upmost importance to characterize the cell phenotypes present within these tissues to ensure that healthy, non-stressed nor diseased tissue is being delivered. Therefore, to characterize the state of the EHTs within this dissertation we performed single cell RNA sequencing over time to understand the transcriptional dynamics of EHTs.

### 5.1.2 Methods

#### 5.1.2.1 Cell Source and Culture

CMs and CFs were sourced, prepared, and cultured according to chapter sections 2.3.1 and 3.3.1.

#### 5.1.2.2 Microtissue Seeding

Microtissues were seeded as described in Chapter 2.3.3

#### 5.1.2.3 Nuclei Extraction and Single Cell RNA Sequencing

Individual nuclei were isolated from frozen (-80 Celsius) control EHT samples cardiac tissue samples frozen at Days 8, 11, and 14 post-seeding. Briefly, nuclei were isolated, and RNA was reverse-transcribed and converted into cDNA libraries using a 10x Chromium Controller and Chromium Single Cell 3' v3.1 reagent kit (10x Genomics). Samples were then labeled using multiplexing technology. Then bar-coded libraries were pooled and sequenced (Illumina NovaSeq 6000) to an average of [insert number] reads per cell for all the samples.

#### 5.1.2.4 RNA Sequencing Analysis

The resulting reads were processed in CellRanger (10x Genomics) then further data analysis and visualization was performed in Seurat V4[266]. All nuclei across conditions were integrated using the single-cell integration function within Seurat. Briefly, this entails processing data for each condition separately and then comparing cell identities between conditions to define anchor points which define cells irrespective of condition.

#### 5.1.2.5 Statistical Analysis

Scatterplots display the average gene expression for each cluster between Day 1 and Day 7, significant genes for both conditions were identified in Seurat by Wilcoxon Rank Sum test, filtering by Bonferroni adjusted p-values of $<0.05$ and log fold-change in expression of $\geq 0.38$.

### 5.1.3 Results and Discussion

To study the changes in RNA expression of CMs and CF in EHTs over time, two batches of samples were acquired for microtissues at Days 8, 11, and 14 following tissue seeding. To have a high enough cell number, microtissues were pooled for each timepoint (between 15 and 16 tissues for Batch 1, and between 8 and 10 tissues for Batch 2). After nuclear extraction, the samples were labeled, and multiplexing technology was applied to different samples for downstream identification and then the bar-coded samples were pooled and sequenced. Shared nearest neighboring clustering identified 18 distinct clusters with 3 distinct cells types 1) CMs, 2) fibroblasts, and 3) a stem population; CMs with expression indicating they were within the cell cycle were separated from general CMs (CC-

CM1 and CC-CM2) (Figure 5.1a). Gene expression analysis of each cluster analysis showed expression of well-established CMs, fibroblasts, and stem cell markers (Figure 5.1b).

We next looked at the breakdown of total cells in each identified cluster by both batch number and sample day (Figure 5.1c). Majority of cells came from the first batch of samples, owing to the increased total cell number input for these samples. Analysis of contribution to clusters by timepoint revealed trends for certain clusters increasing or decreasing progressively. Of note, the CM2 cluster was more predominate at later timepoints. This is interesting as this cluster was most enriched for the hypoxia-inducible factor 1-alpha (H1F1A) gene and signaling pathway (Figure 5.S1, Figure 5.S2). This pathway is usually activated during hypoxia and ischemic injury and is known to be involved in the promotion of angiogenic and vascular remodeling and the activation of glycolytic metabolic pathways during these processes[267]. This indicates that over time these tissues may be undergoing increased levels of metabolic stress. Clusters which decreased overtime included CC-CM1, CC-CM2, Fibro1, Fibro2, SC3, and CM10. The decrease in both cell cycle CMs clusters indicates a loss in proliferative capacity of these cells, which may be evidence of a more matured CM, as adult CMs have low proliferative capability. The decreasing fibroblast clusters, Fibro1 and Fibro2, are enriched for FN1 and COL6A3, respectively, indicating that over time these tissues may stabilize and produce less ECM (Figure 5.S1).

We next compared changes in the levels of gene expression within each cluster (Figure 5.1d), while not all of the clusters showed significant changes, the ones which did are shown. In addition to the increase in the H1F1A expressing CM2 cluster size, the cells in this cluster and CM3 shown higher expression levels of H1F1A at Day 14, supportive of the idea that CM stress in EHTs increases over time. Ankyrin Repeat Domain 1 (ANKRD1) and Myosin Light Chain 7 (MYL7) are also lower in expression at Day 14 compared to Day 8 in

CM1 and CM3 then in CM1 and CM5, respectively, which suggest changes to sarcomere structure over time. Further study of these transcriptional changes over time and their implications for how EHTs develop is essential to accurately utilize EHTs to study healthy and diseased tissues.

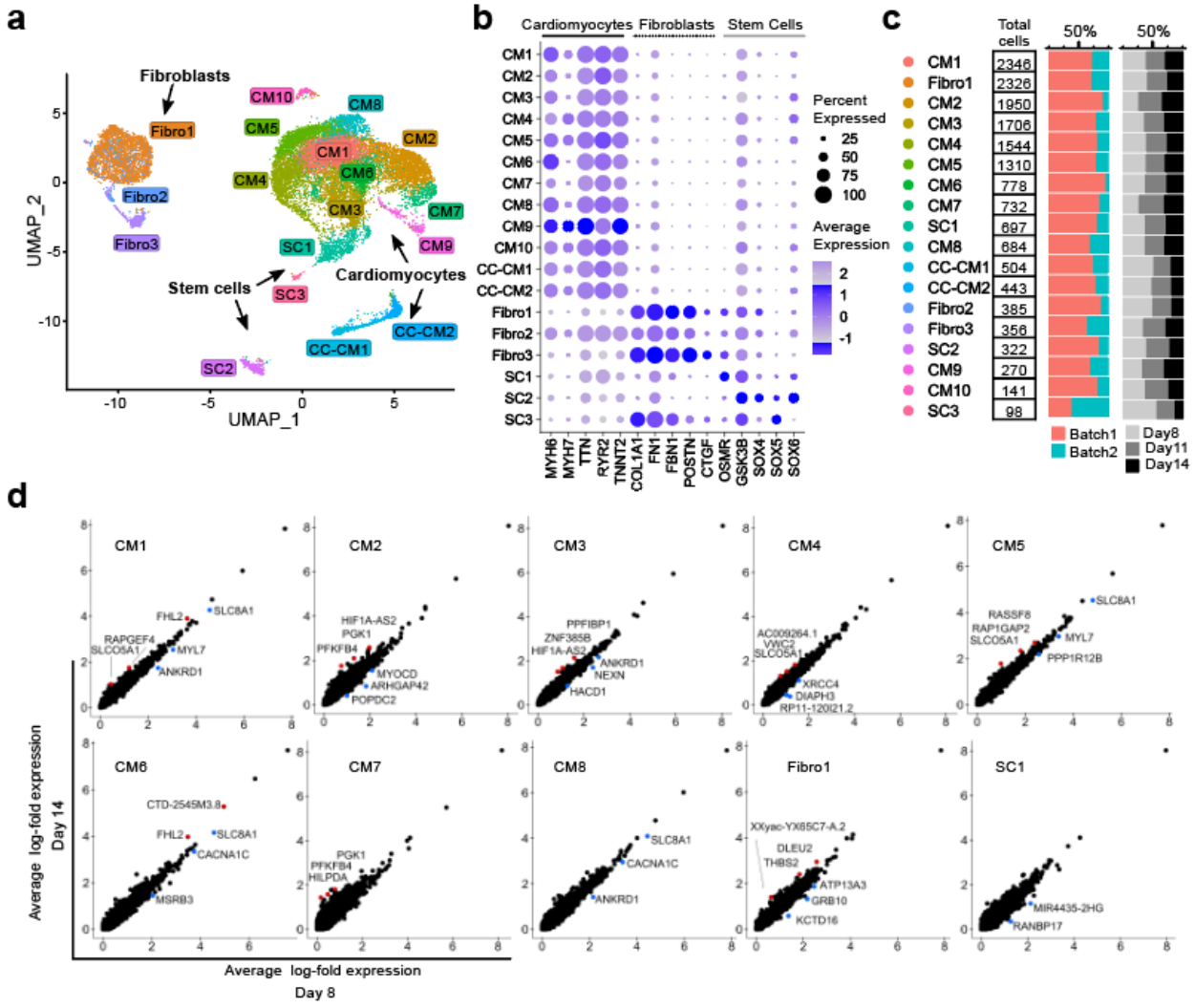


**Figure 5.1. Single-cell sequencing reveals cell population and shifts over time in EHTs.** a) Uniform Manifold Approximation and Projection (UMAP) indicating transcriptome similarities across individual cells and resulting clustering. Different colors and labels indicate the clusters identified by shared nearest neighbor clustering. b) Dot plot showing gene expression of canonical markers for cardiomyocytes, fibroblasts, and stem cells throughout all clusters. c) Total cell counts by identified cluster (left), breakdown of total percentage of cells per cluster from Batch 1 (pink) and Batch 2 (blue), (center), and breakdown of total percentage of cells per cluster from Day 8 (light grey), Day 11 (dark grey), and Day 14 (black). d) Average log-fold expression at Day 14 versus at Day 8 for clusters showing significant gene expression changes (CM1, CM2, CM3, CM4, CM5, CM6, CM7, CM8, Fibro1, SC1). Labeled genes represent the top three significantly enriched genes for Day 8 (blue) and Day 14 (red).

## 5.2 Vascularization of engineered heart tissues

### 5.2.1 Introduction

The vascularization of EHTs remains to be a difficult challenge in the fields of tissue engineering and tissue regeneration[19,110]. Vascularization is an important challenge to address if the field wants to build tissues large enough to augment heart function for a patient. Additionally, vascularization is important when we consider the successful integration of engineered tissues into a host[19]. While some work has been done in the area, robust formation, and persistence of such vascular has not been demonstrated. The work in this sub-chapter is an effort to vascularize the existing EHT system already demonstrated in Chapter 2, to investigate optimal conditions to support tri-cultures between CMs, endothelial cells, and fibroblasts.

### 5.2.2 Methods

#### 5.2.2.1 Cell Source and Culture

Human umbilical vein endothelial cells (HUVECs, Lonza, pooled from four donors) transduced with pLenti.PGK.LifeAct-Ruby.W (Addgene plasmid #51009) were used as previously described[268]. LifeAct-Ruby-HUVECs were maintained in Endothelial Growth Medium-2 (EGM-2, Lonza) and used between Passages 5 and 8. Neonatal human dermal fibroblasts (HDFs, Lonza, single donor) were cultured in Fibroblast Growth Medium-2 (FGM-2, Lonza) and used before P10. Cardiomyocytes were prepared and cultured as described in Chapter 2.3.2.

#### 5.2.2.2 Microtissue Seeding

Microtissues were seeded as described in Chapter 2.3.3 with the following exceptions. To make each tissue, a total of 66,000 cells (54k iPSC-CMs, 6k LifeAct-Ruby-HUVECs, and 6k HDFs) for the tri-cultures condition or 12,000 cells (6k

LifeAct-Ruby-HUVECs, and 6k HDFs) for the co-culture condition. Tissue maintenance media consisted of 50%/50% RPMI/EGM-2 with B27, and aprotinin (0.033 mg/ml), and was changed every day post-seeding. After 7 days, aprotinin was removed from media.

#### 5.2.2.3 Imaging

Prior to imaging, samples were stained with 1:1000 DAPI for 1 hour at RT. Z-stacks of samples were imaged on a Leica SP8 confocal microscope with a Leica 25x and 10x water objectives and Leica LAS X imaging software.

### 5.2.3 Results and Discussion

To address the challenge of vascularizing EHTs, a part of this thesis focused on optimizing the conditions of the co-culture of CMs and ECs. The first optimization which was performed was to determine the media which would enable to survival of both CMs and EC. To do this, HUVECs were passaged and grown under various media conditions including RPMI with B27, EGM-2, EGM-2 with B27, 50%/50% RPMI/EGM-2 with B27, and 50%/50% tissue maintenance media/EGM-2, and evaluated for growth and morphology. HUVECs maintained similar growth and morphology to the control EGM-2 condition in both EGM-2 with B27 and the 50%/50% RPMI/EGM-2 with B27. They showed abnormal morphology and decreased proliferation in 50%/50% tissue maintenance media/EGM-2 (Figure 5.2a). CMs were similarly cultured in 2D with the same media conditions and evaluated based on beating function. CM did not spontaneously beat in conditions only containing EGM-2 medium, but did in the control RPMI with B27 condition as well as the 50%/50% RPMI/EGM-2 with B27 and 50%/50% tissue maintenance media/EGM-2

conditions (data not shown). Based on these media condition results, the media chosen for the tri-culture of HUVECs, CMs, and fibroblasts was 50%/50% RPMI/EGM-2 with B27.

Microtissues were then seeded in a fibrin gel containing mRuby-HUVECs and human dermal fibroblasts (HDFs) in a conditions with and without CMs. Within these conditions, an aligned network of vessels formed within the cardiac microtissue (Figure 5.2b). Figure 5.2c, left highlights the proximity of these vessels to striated CMs and Figure 5.2c, right shows the vessel morphology without the presence of CMs. Additionally, in both of these images, there is evidence of lumen formation (Figure 5.2c). While promising, there were challenges to show robust vessel network formation in vitro (Figure 5.2d). To determine if these constructs would survive upon implantation, seven days after seeding, microtissues were subcutaneously implanted. When harvested 7 days after the implantation, they showed the presence of vascular networks and survival of CMs. Interestingly, some networks which failed to form in vitro and that were subcutaneously implanted were able to form networks in the in vivo setting (Figure 5.2e). This points to potential metabolic needs or paracrine signaling, which in vitro were sometimes but not always being met, evidenced by the occasional successful networks seen in Figure 5.2b,c.

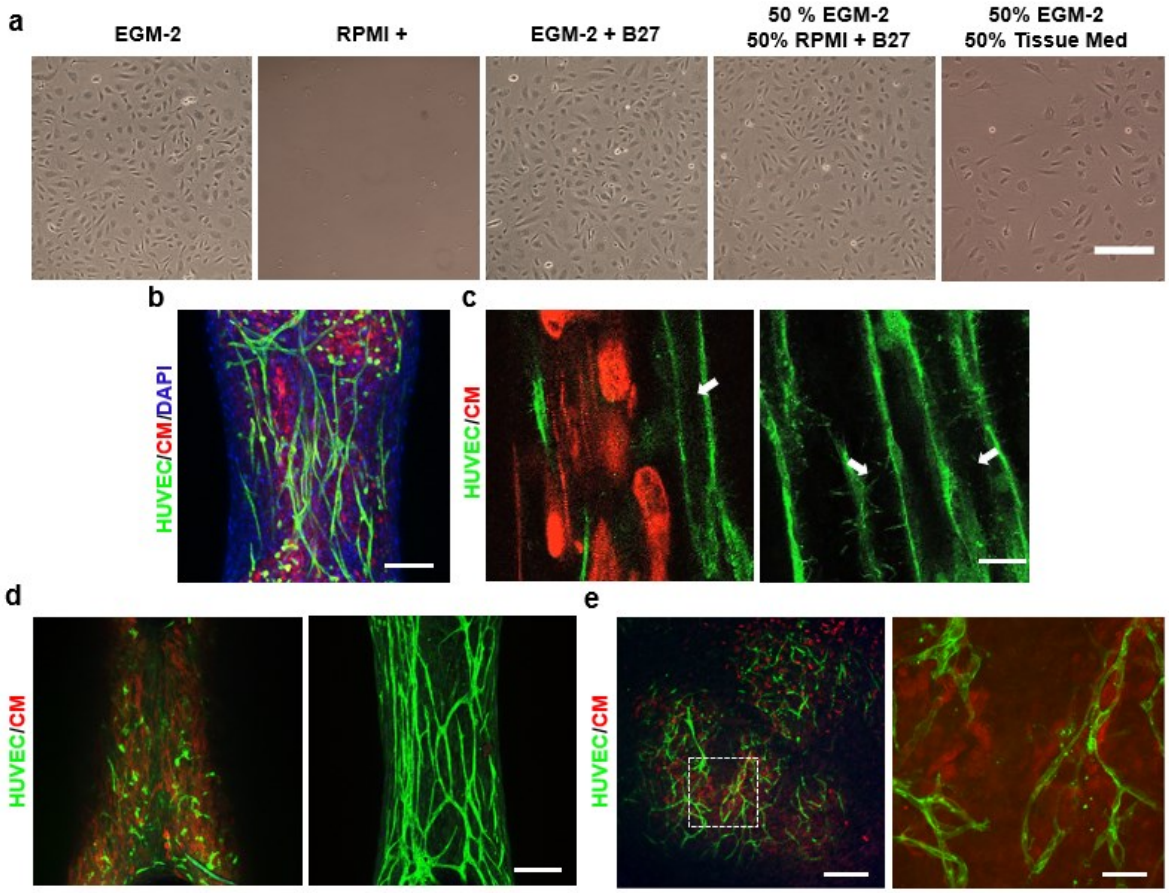


**Figure 5.2. Conditions for vascularization of engineered heart tissues.** a) HUVECs in cell medium conditions. Scale bar = 200 μm. b) Maximum projection of z-stack taken of Day 7 engineered heart tissue with Titin-GFP CMs (Red), m-Ruby HUVECs (Green) with DAPI (blue). Scale bar = 200μm. c) High magnification of microtissue composed of Titin-GFP CMs (Red) and m-Ruby HUVECs (Green) (left) and m-Ruby HUVECs (Green) (right). White arrows point to evidence of lumens. d) Implanted microtissues Day 7 post-implantation, CM (red) and HUVECs (green). Scale bar = 100 μm (left), white dashed lines represents inset of higher magnification region (right).

## 5.3 EHTs as a model system to study cell engraftment

### 5.3.1 Introduction

One method that is being explored in the field to re-functionalize myocardium is the delivery of new cardiomyocytes to infarcted regions. The delivery of new cells to an infarct region has shown some success, however, the two largest challenges are lack of

sufficient engraftment efficiency and effective coupling to the infarcted zone[269–272]. Typically, a fibrosis layer forms between new tissue and the heart preventing efficient coupling leading to concerns of arrhythmia generation[86,273]. It is thought the highly contractile environment of the heart may be a cause of the low efficiency[274], not only for cell delivery but also treatment with acellular-based therapies. Creating solutions to these challenges is difficult due to the difficultly of perturbing certain conditions in animals (i.e. limiting contractions of the heart), as well as the limits on the sample sizes of large animal studies[275,276]. The development of a high-throughput human myocardial injury model would be useful for parsing through various potential treatment conditions and their mechanisms and ultimately lead to determining optimal treatment strategies. Therefore, we sought to evaluate if the EHT model presented in thesis could be used as a platform to parse engraftment strategies. The work presented here focuses on evaluating the delivery of CMs under a few delivery contexts.

### 5.3.2 Methods

#### 5.3.2.1 Cell Source and Culture

CMs and CFs were sourced, prepared, and cultured as according to chapter sections 2.3.1 and 3.3.1.

#### 5.3.2.2 Microtissue Seeding

Microtissues were seeded as described in Chapter 2.3.3 with the exception that iPSC-CMs were sourced from the PGP1 line.

#### 5.3.2.3 Graft Preparation

For the cell suspension condition, TTN-GFP CMs were dissociated from culture dishes between 6 days after replating. CMs were then re-suspended at a

concentration of 9.8 mill cells/ml in tissue maintenance media, including 5 μM Y-27632, and aprotinin (0.033 mg/ml).

For fibrin gel delivery, TTN-GFP CMs were again dissociated from culture between 6 days after replating. CMs were then re-suspended at a concentration of 9.8mill cells/ml in an ECM solution consisting of human fibrinogen (4 mg/ml), 10% Matrigel, 0.4 U of thrombin per mg of fibrinogen, 5 μM Y-27632, and aprotinin (0.033 mg/ml).

For cell sheet preparation, a 2% poly-n-isopropylacrylamide solution in butanol was spin coated onto a glass coverslip at 6000rpm for 1 min. PDMS molds with 35mm diameter holes were affixed to coated glass coverslips and UV sterilized for 15 minutes. Prior to cell seeding, coverslips were coated with a 10μg/ml fibronectin solution for 1 hour. 25k TTN-GFP CMs were then seeded into each PDMS well and cultured for 4 days. Immediately prior to engraftment, wells were removed from incubator and cooled to enable detachment of sheets.

#### 5.3.2.4 Engraftment Process

Six days after microtissue seeding, excess media was removed from tissue wells and either a cell sheet, or 25k CMs were delivered from the cell suspension or fibrin delivery preparations. Then, devices were inverted for 45 minutes to allow for cell attachment and tissue maintenance media was added including 5 μM Y-27632, and aprotinin (0.033 mg/ml). After 2 days, Y-27632 was removed.

#### 5.3.2.5 Imaging

Prior to imaging, samples were stained with 1:1000 DAPI for 1 hour at RT. Z-stacks of samples were imaged on a Leica SP8 confocal microscope with a Leica 25x water objective and Leica LAS X imaging software or Yokogawa CSU-21-Zeiss

Axiovert 200M inverted spinning-disk microscope with a Zeiss 40x water objective and Evolve EMCCD camera.

### 5.3.3 Results and Discussion

Within the cardiac regeneration field, multiple techniques are being utilized to engraft healthy CMs to existing tissue, including the delivery of cells via injection, the delivery of cells within a matrix, or the delivery of cultured cardiac patches to the surface of the heart[90,277,278]. To address the utility of an in vitro model for studying engraftment, we first tested various techniques to deliver CMs to these microtissues including delivery of a CM cell suspension in medium, within a fibrin gel , and a cultured cell sheet, then studied their integration over time (Figure 5.3a). To separate the two population of cells, the host and graft cells, non-fluorescent PGPI-sourced CMs were used to make the host microtissue, then TTN-GFP expressing CMs were used for the graft tissues, this enabled real-time tracking of grafted cells throughout the integration process.

Since low retention of engrafted cells into the host tissue is a challenge in the field, we quantified the amount of engrafted cells which had integrated into the tissue after 4 days of culture to compare the various methods of delivery (Figure 5.3b). The cells delivered in a simple cell suspension, showed minimal retention, while those delivered as a cell sheet showed higher retention (Figure 5.3c). Additionally, in both the sheet and fibrin gel delivery condition, sarcomere structures were present, indicating these cells were functionally engrafting (Figure 5.3b).

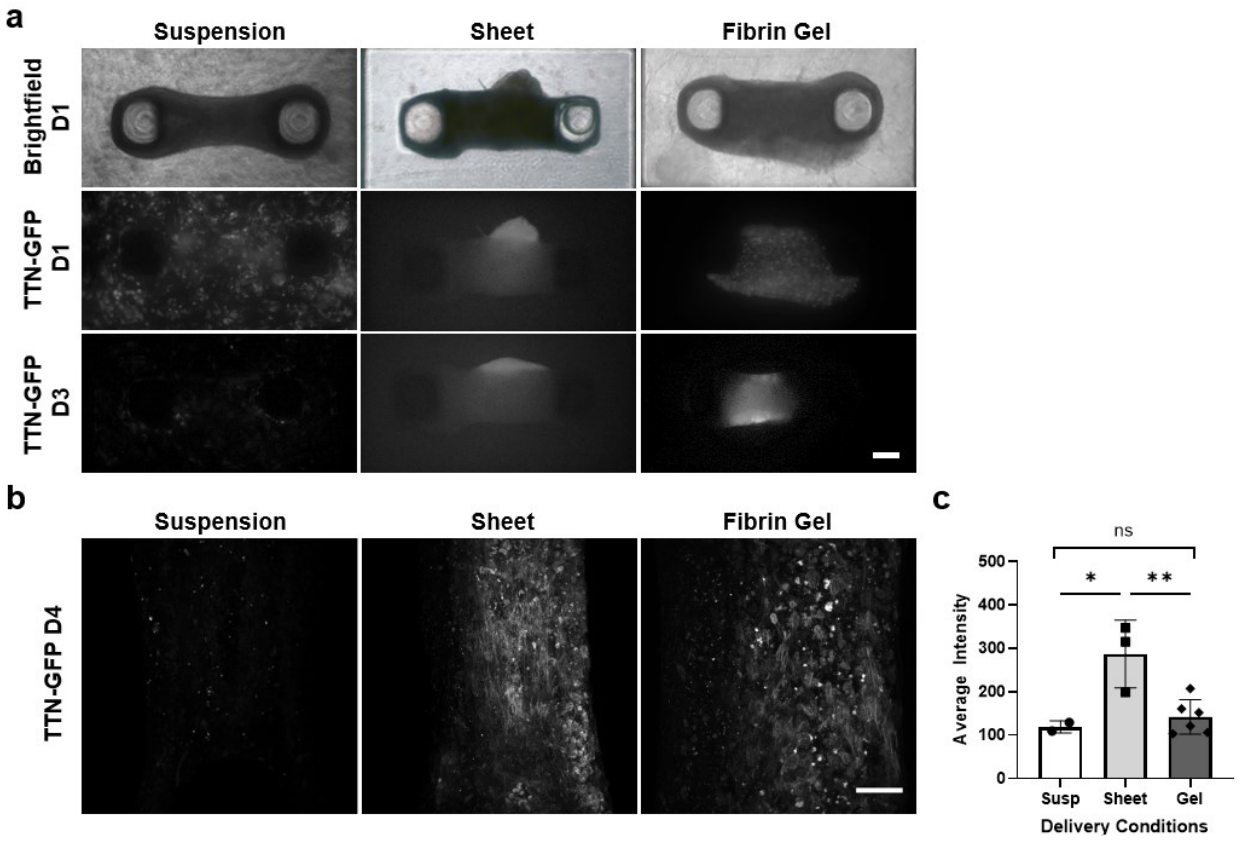


**Figure 5.3. Various delivery methods for cardiomyocytes on engineered heart tissues. a)** Images of microtissues in brightfield and TTN-GFP after on Day 1 (top and middle) and 3 (bottom) post-delivery of cell suspension (left), cell sheet (center), and fibrin gel-encapsulated cells (right). Scale bar = 250 μm. **b)** Fluorescence imaging of engrafted cells (TTN-GFP) on microtissues 4 days after seeding in cell suspension, cell sheet, and fibrin gel conditions. Scale bar = 100 μm. **c)** Average intensity of engrafted cells (TTN-GFP signal) over conditions.

Due to the importance of sarcomere alignment for cardiac function, we were interested in understanding if after engraftment the new cardiomyocytes can align to the existing host tissue. To study this, we used the cell sheet delivery system. First sarcomeres of TTN-GFP CMs were imaged for the cell sheets 4 days after seeding and prior to lifting. The arrangement of sarcomeres in the sheets was random networks (Figure 5.4). Then, 4 days after seeding sarcomeres were imaged again. At this time point the sarcomeres showed more alignment along the length of the tissue compared

to the organization in the sheets, demonstrating the ability of CMs to remodel their alignment structures after the formation of initial cell-cell contacts within the sheets. While a preliminary study, this demonstrates a platform to study cell engraftment onto EHTs and how this platform could be used to study the remodeling and integration processes.

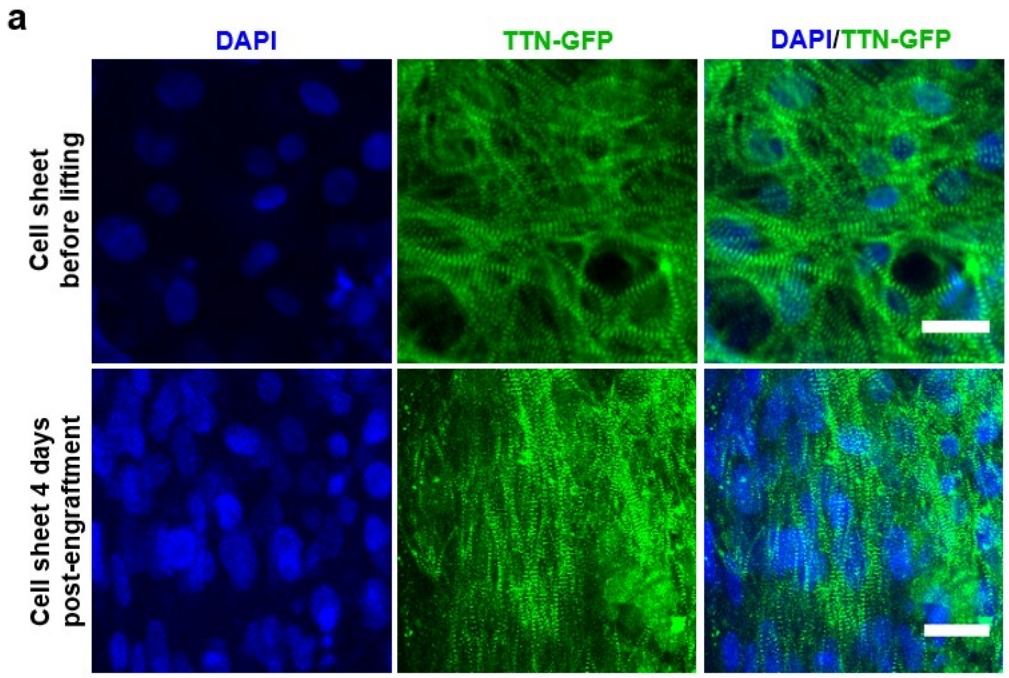


**Figure 5.4. Sarcomere alignment in cell sheet engrafted cells. a)** CM nuclei (blue) and sarcomeres (green) of cell sheets before lifting (top) and 4 days following engraftment of sheets onto microtissues (bottom). Scale bar = 25μm.

## 5.4 Supplemental Data

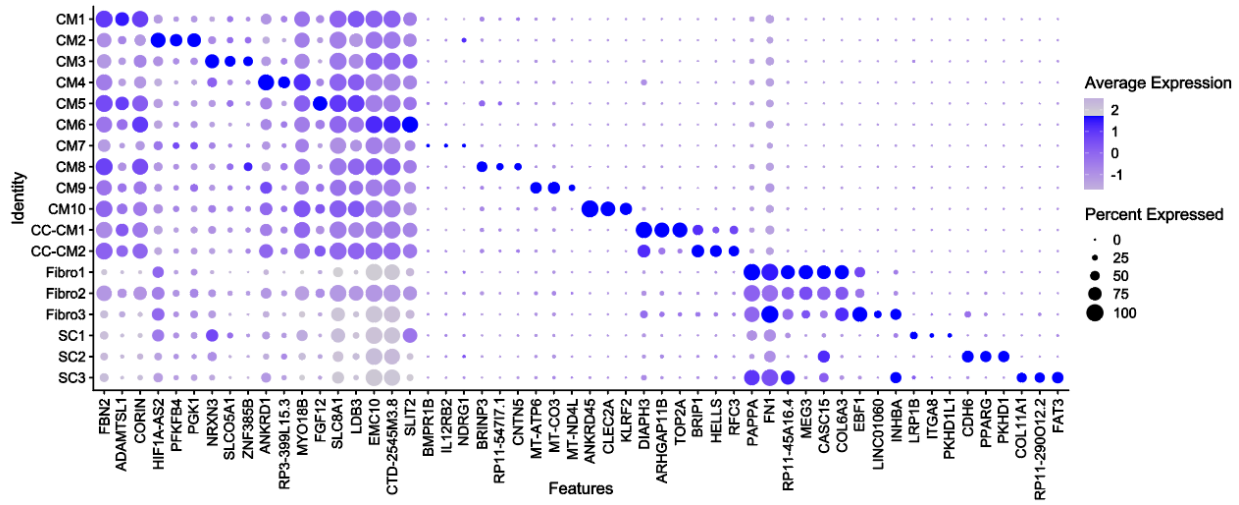


**Figure 5.S1. Dot plot of the top three identifying gene markers for each cluster.**

a

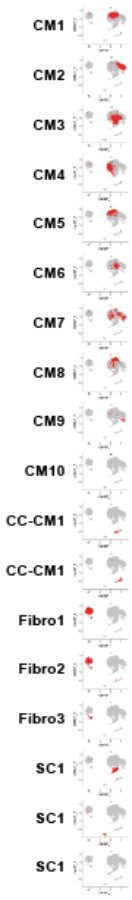


b

| | Fold Enrichment | Adjusted p-value |
|---|---|---|
| cell communication by electrical coupling… | 60.3 | 1.18E-02 |
| cardiac myofibril assembly | 50.3 | 2.21E-02 |
| hypoxia-inducible factor-1alpha signaling pathway | >100 | 2.52E-02 |
| NADH regeneration | 83.1 | 4.04E-03 |
| negative chemotaxis | 24.9 | 2.56E-02 |
| cell-cell adhesion via plasma-membrane adhesion molecules | 8.8 | 2.55E-03 |
| cardiac myofibril assembly | 65 | 3.61E-04 |
| regulation of the force of heart contraction | 54 | 3.79E-05 |
| membrane depolarization during atrial cardiac… | >100 | 1.45E-02 |
| membrane depolarization during AV node cell action potential | >100 | 4.02E-02 |
| membrane depolarization during cardiac muscle cell action potential | 72.1 | 2.24E-04 |
| atrial cardiac muscle cell to AV node cell signaling | 70 | 6.80E-03 |
| protein folding in endoplasmic reticulum | >100 | 9.16E-03 |
| endoplasmic reticulum unfolded protein response | 51.8 | 1.25E-02 |
| cardiac muscle cell development | 23.8 | 3.12E-03 |
| cardiac cell development | 21.9 | 4.95E-03 |
| electron transport coupled proton transport | > 100 | 3.16E-02 |
| energy coupled proton transmembrane transport… | > 100 | 3.16E-02 |
| cardiac myofibril assembly | 63.6 | 4.04E-04 |
| regulation of cardiac muscle contraction… | 54.5 | 7.82E-04 |
| mitotic spindle midzone assembly | > 100 | 2.22E-05 |
| mitotic spindle elongation | > 100 | 2.22E-05 |
| lagging strand elongation | > 100 | 3.26E-02 |
| DNA replication, synthesis of RNA primer | > 100 | 8.91E-04 |
| chondrocyte differentiation | 17.7 | 1.61E-02 |
| cartilage development | 13.9 | 4.22E-05 |
| cartilage development | 11.6 | 5.70E-03 |
| regulation of angiogenesis | 9.1 | 4.42E-04 |
| collagen-activated signaling pathway | 58.4 | 1.26E-02 |
| endodermal cell differentiation | 30.3 | 1.02E-02 |
| regulation of cellular response to growth factor stimulus | 5.7 | 1.21E-03 |
| kidney development | 4.9 | 3.73E-02 |
| regulation of microvillus organization | 42.4 | 3.99E-03 |
| cell-cell junction organization | 9.4 | 1.79E-06 |
| collagen fibril organization | 36.1 | 4.81E-10 |
| chondrocyte differentiation | 23.8 | 3.12E-05 |

**Figure 5.S2. UMAP highlights by cluster and top GO terms.** a) UMAP highlight for each identified cluster. b) Top two GO terms in gene ontology
analysis on genes significantly enriched within each cluster, showing fold enrichment and adjusted p-values.

# Chapter 6: Conclusions and Future Directions

Cardiovascular disease (CVD) represents almost a third of worldwide mortality. Almost half of this CVD is from coronary heart disease[279,280]. The treatments which exist after a coronary artery blockage and subsequent MI, are very limited, particularly for patients who are unable to receive immediate clinical intervention[6,7]. While most patients survive the initial infarct event, the consequences of the long-term presence of a scar leads to high risk for arrhythmias and heart failure. These long-term consequences are massive burdens for both patients and hospital systems. While current treatments based on existing models help many patients, there are still large gaps in our understanding of CVD. By closing these gaps, better therapies could be developed to reduce the long-term impact of an infarct. Therefore, there is an urgent need for improved models to study the cardiac injury response. While most of the research in this area is built upon *in vivo* animal models, in this dissertation, we demonstrate the use of human *in vitro* models based off iPSC and EHT technologies as systems to study the acute cardiac injury process. We show how these models are able to capture many aspects of the post-injury cardiac tissue dysfunction and demonstrate their potential to study further questions surrounding cardiac recovery and regeneration.

In Chapter 2, we show how an EHT can be acutely damaged and display similar functional disturbances to those seen in *in vivo* MI models. Furthermore, we demonstrate the model's ability to capture remodeling events including local changes in contractility of both injured and surrounding tissue regions. The ability to capture many of these processes in an EHT model enables a high-throughput system which could be used to probe new therapeutic targets to minimize the long-term effects of an infarct.

In Chapter 3, we show the adaption of Archon1, a far-red genetically-encoded voltage sensor used in the neuroscience field, to study cell specific action potentials (APs) within both monolayers

of iPSC-CMs and EHTs[131]. The ability to genetically encode a sensor with fast kinetics and high signal-to-noise, comparable to that of patch clamp electrophysiology, demonstrates a non-invasive and non-toxic method to measure the electrical properties, which could be utilized *in vivo*. This technology can enable us to study the effects of cardiac injury and disease on AP dynamics. The ability to measure multiple cells at once also allows for the study of cardiac synchrony between cells, an important challenge for therapies based on the engraftment of new cells to a host damaged tissue.

In Chapter 4, we demonstrate the advantage of using *in vitro* systems by removing the complexity of contractile CMs to look specifically at the effect of ECM alignment on the initial stages of wound healing performed by fibroblasts. We find that fibronectin alignment is highly important for the building of new provisional matrix after an injury, and that regions of higher fibronectin anisotropy impede provisional matrix growth[132]. This has implications for treatments which can utilize or modify local alignment to promote faster healing after tissue injury.

Finally in Chapter 5, we address some of the future directions of this work, briefly demonstrating ways that EHT models could be built and expanded upon to address additional research questions and gaps in the field including 1) analysis of single cell gene expression in EHTs, 2) incorporation of vascular cells into EHTs, and 3) EHTs as a model for cell engraftment.

To understand the types of biological processes that these cells model, we evaluated the RNA expression states of cells within EHTs . This is an important consideration for both building EHT for implantation and disease modeling. While having many of the characteristics of human myocardium, it's important to remember that engineered systems only recapitulate a handful of elements that are involved in maintaining a healthy homeostatic state in *in vivo* tissue. In a way, the biggest advantage of *in vitro* systems, the ability to dissect out complexity, is also its largest disadvantage, the loss of complexity. Additionally, the longevity of these models is an important

limitation. Many diseases which the field seeks to model with EHTs progress on time scales magnitudes longer than the culture time of EHTs. In the case of myocardial scarring from an MI, as modelled here, the scarring process occurs over weeks and months, not days as modeled here. Genetic diseases are on an even more dramatic time scale, which can take years to manifest disease. For this reason, it has been challenging to induce many of the long-term effects of fibrotic diseases *in vitro*. Therefore, the correct contextualization of *in vitro* models and validation in in vivo models is very important as the use of these systems increase.

While the simplicity of EHTs enables the study of direct interactions, a majority of current EHTs are composed of only CMs and a fibroblast population. As we know, there are many more cell types which make up cardiac tissue, and to study these cells we will need to develop models which can support these various co-cultures. As endothelial cells are the most abundant cell type in the myocardium besides CMs and CFs, we demonstrated the creation of a model which could enable the study of the interactions between CMs, CFs, and endothelial cells. As the field looks toward creating large scale EHTs for implantation to improve heart function, there will be a strong need for the integration of endothelial cells into EHTs[19]. Another important consideration is the sources of these cells. While in this system we use primary CFs and HUVECs, over the last few years, technologies have been developed to enable the creation of these cell types from iPSCs. While further characterization of the maturity and phenotype of these cells must be done, they have the advantage of being able to be sourced directly from a patient, avoiding immune rejection seen when introducing allografts. Therefore, as models are developed in the future, specifical consideration should be made regarding the sources of various cell types depending on the goals of the model.

*In vitro* cardiac models are also used as high throughput testbeds in drug development[130,281]. As the field as grown over the recent years, there is increasing evidence that iPSC-derived CMs and EHT can be used to predict drug efficacy and safety, providing an accurate, cost-effective method

compared animal studies. In addition to testing the delivery of molecules to cardiac tissue, these systems could also be used to test new cell therapies or other mechanical techniques which are under development to re-functionalization or prevent the progression of myocardial scars after an MI. In Chapter 5 we show a study which demonstrates the utility of an EHT model to study challenges in the engraftment of CMs to a host tissue. While preliminary, this type of model could be used to optimize the delivery of CMs *in vivo* by testing the best format of delivery, stage in the maturity of delivered cardiomyocytes, etc.

The work in this dissertation has been built upon many recent advancements in the iPSC technologies, 3D engineered tissue systems, and tools for characterization. Together, all of these have facilitated the development of the models presented in this dissertation and many others, enabling improved studies of human cardiac function and insights into many disease processes. As these advancements continue to grow, this will only enable *in vitro* models to become more powerful tools for studying human cardiac disease, ultimately leading to discoveries which can improve patient outcomes.

# Bibliography


1. Mozaffarian, D. *et al. Heart disease and stroke statistics-2015 update : A report from the American Heart Association*. *Circulation* vol. 131 (2015).

2. Awada, Hassan K., Hwang, Mintai P., Wang, Y. Towards Comprehensive Cardiac Repair and Regeneration after Myocardial Infarction: Aspects to Consider and Proteins to Deliver. *Biomaterials* **8**, 583–592 (2016).

3. Gourdie, R. G., Dimmeler, S. & Kohl, P. Novel Therapeutic Strategies Targeting Fibroblasts and Fibrosis in Heart Disease. *Nature Reviews Drug Discovery* **In press**, 620–638 (2016).

4. Prabhu, S. D. & Frangogiannis, N. G. The Biological Basis for Cardiac Repair After Myocardial Infarction. *Circulation Research* **119**, 91–112 (2016).

5. Talman, V. & Ruskoaho, H. Cardiac fibrosis in myocardial infarction—from repair and remodeling to regeneration. *Cell and Tissue Research 2016 365:3* **365**, 563–581 (2016).

6. Holmes, J. W., Laksman, Z. & Gepstein, L. Making better scar: Emerging approaches for modifying mechanical and electrical properties following infarction and ablation. *Progress in Biophysics and Molecular Biology* **120**, 134–148 (2016).

7. Yeh, R. W. *et al.* Population Trends in the Incidence and Outcomes of Acute Myocardial Infarction. *New England Journal of Medicine* **362**, 2155–2165 (2010).

8. Cahill, T. J. & Kharbanda, R. K. Heart failure after myocardial infarction in the era of primary percutaneous coronary intervention: Mechanisms, incidence and identification of patients at risk. *World Journal of Cardiology* **9**, 407 (2017).

9. Gerber, Y. *et al.* Mortality Associated with Heart Failure after Myocardial Infarction: A Contemporary Community Perspective. *Circulation: Heart Failure* **9**, (2016).

10. Francis Stuart, S. D., de Jesus, N. M., Lindsey, M. L. & Ripplinger, C. M. The crossroads of inflammation, fibrosis, and arrhythmia following myocardial infarction. *Journal of Molecular and Cellular Cardiology* **91**, 114–122 (2016).

11. Richardson, W. J., Clarke, S. A., Alexander Quinn, T. & Holmes, J. W. Physiological Implications of Myocardial Scar Structure. *Compr Physiol* **5**, 1877 (2015).

12. Kohl, P. & Gourdie, R. G. Fibroblast-myocyte electrotonic coupling: Does it occur in native cardiac tissue? *Journal of Molecular and Cellular Cardiology* **70**, 37–46 (2014).

13. Ongstad, E. L. & Gourdie, R. G. Myocytefibroblast electrical coupling: The basis of a stable relationship? *Cardiovascular Research* **93**, 215–217 (2012).

14. Leask, A. Getting to the heart of the matter: New insights into cardiac fibrosis. *Circulation Research* **116**, 1269–1276 (2015).

15. Torrent-Guasp, F. *et al.* Towards new understanding of the heart structure and function. *European Journal of Cardio-thoracic Surgery* **27**, 191–201 (2005).

16. Fomovsky, G. M., Thomopoulos, S. & Holmes, J. W. Contribution of extracellular matrix to the mechanical properties of the heart. *Journal of Molecular and Cellular Cardiology* **48**, 490–496 (2010).

17. Litviňuková, M. *et al.* Cells of the adult human heart. *Nature 2020 588:7838* **588**, 466–472 (2020).

18. Zhou, P. & Pu, W. T. Recounting cardiac cellular composition. *Circ Res* **118**, 368 (2016).

19. Novosel, E. C., Kleinhans, C. & Kluger, P. J. Vascularization is the key challenge in tissue engineering. *Advanced Drug Delivery Reviews* **63**, 300–311 (2011).

20. Vunjak-Novakovic, G. *et al.* Challenges in cardiac tissue engineering. *Tissue Eng Part B Rev* **16**, 169–187 (2010).

21. Kanno, S. & Saffitz, J. E. The role of myocardial gap junctions in electrical conduction and arrhythmogenesis. *Cardiovascular Pathology* **10**, 169–177 (2001).

22. Patra, C., Boccaccini, A. R. & Engel, F. B. Vascularisation for cardiac tissue engineering : the extracellular matrix. 532–547 (2015).

23. Tallquist, M. D. & Molkentin, J. D. Redefining the identity of cardiac fibroblasts. *Nature Reviews Cardiology 2017 14:8* **14**, 484–491 (2017).

24. Rog-Zielinska, E. A., Norris, R. A., Kohl, P. & Markwald, R. The Living Scar – Cardiac Fibroblasts and the Injured Heart. *Trends in Molecular Medicine* **22**, 99–114 (2016).

25. Porter, K. E. & Turner, N. A. Cardiac fibroblasts: At the heart of myocardial remodeling. *Pharmacology & Therapeutics* **123**, 255–278 (2009).

26. Kong, P., Christia, P. & Frangogiannis, N. G. The pathogenesis of cardiac fibrosis. *Cell Mol Life Sci* **71**, 549–574 (2014).

27. Segers, V. F. M., Brutsaert, D. L. & de Keulenaer, G. W. Cardiac Remodeling: Endothelial Cells Have More to Say Than Just NO. *Frontiers in Physiology* **9**, 382 (2018).

28. Yan, X. *et al.* Temporal dynamics of cardiac immune cell accumulation following acute myocardial infarction. *Journal of Molecular and Cellular Cardiology* **62**, 24–35 (2013).

29. Lai, S. L., Marín-Juez, R. & Stainier, D. Y. R. Immune responses in cardiac repair and regeneration: a comparative point of view. *Cellular and Molecular Life Sciences* **76**, 1365 (2019).

30. Bönner, F., Borg, N., Burghoff, S. & Schrader, J. Resident Cardiac Immune Cells and Expression of the Ectonucleotidase Enzymes CD39 and CD73 after Ischemic Injury. *PLoS ONE* **7**, (2012).

31. Ma, Y. *et al.* Myofibroblasts and the extracellular matrix network in post-myocardial infarction cardiac remodeling. *Pflugers Archiv European Journal of Physiology* **466**, 1113–1127 (2014).

32. Eghbali, M. & Weber, K. T. Collagen and the myocardium: fibrillar structure, biosynthesis and degradation in relation to hypertrophy and its regression. *Molecular and Cellular Biochemistry 1990 96:1* **96**, 1–14 (1990).

33. Holmes, J. W., Nuñez, J. A. & Covell, J. W. Functional implications of myocardial scar structure. *https://doi.org/10.1152/ajpheart.1997.272.5.H2123* **272**, (1997).

34. Li, B. & Wang, J. H. C. Fibroblasts and myofibroblasts in wound healing: Force generation and measurement. *Journal of Tissue Viability* **20**, 108–120 (2011).

35. Tracy, L. E., Minasian, R. A. & Caterson, E. J. Extracellular Matrix and Dermal Fibroblast Function in the Healing Wound. *Advances in Wound Care* **5**, 119 (2016).

36. Ray, A., Slama, Z. M., Morford, R. K., Madden, S. A. & Provenzano, P. P. Enhanced Directional Migration of Cancer Stem Cells in 3D Aligned Collagen Matrices. *Biophysical Journal* **112**, 1023–1036 (2017).

37. Pang, Y., Wang, X., Lee, D. & Greisler, H. P. Dynamic quantitative visualization of single cell alignment and migration and matrix remodeling in 3-D collagen hydrogels under mechanical force. *Biomaterials* **32**, 3776–3783 (2011).

38. Dickinson, R. B., Guido, S. & Tranquillo, R. T. Biased cell migration of fibroblasts exhibiting contact guidance in oriented collagen gels. *Annals of Biomedical Engineering* **22**, 342–356 (1994).

39. Kubow, K. E. *et al.* Mechanical forces regulate the interactions of fibronectin and collagen i in extracellular matrix. *Nature Communications* **6**, (2015).

40. Smith, M. L. *et al.* Force-induced unfolding of fibronectin in the extracellular matrix of living cells. *PLoS Biology* **5**, 2243–2254 (2007).

41. Lambiase, P. D. & Tinker, A. Connexins in the heart. *Cell and Tissue Research 2014 360:3* **360**, 675–684 (2014).

42. Henderson, C. A., Gomez, C. G., Novak, S. M., Mi-Mi, L. & Gregorio, C. C. Overview of the Muscle Cytoskeleton. *Compr Physiol* **7**, 891 (2017).

43. Kirsner, R. S. & Eaglstein, W. H. The Wound Healing Process. *Dermatologic Clinics* **11**, 629–640 (1993).

44. Clark, R. A. F. *et al.* Fibronectin and fibrin provide a provisional matrix for epidermal cell migration during wound reepithelialization. *Journal of Investigative Dermatology* **79**, 264–269 (1982).

45. Greiling, D. & Clark, R. A. F. Fibronectin provides a conduit for fibroblast transmigration from collagenous stroma into fibrin clot provisional matrix. *Journal of Cell Science* **110**, 861–870 (1997).

46. Barker, T. H. & Engler, A. J. The provisional matrix: setting the stage for tissue repair outcomes. *Matrix Biology* **60–61**, 1–4 (2017).

47. Yaoita, H., Ogawa, K., Maehara, K. & Maruyama, Y. Apoptosis in relevant clinical situations: Contribution of apoptosis in myocardial infarction. *Cardiovascular Research* **45**, 630–641 (2000).

48. Saraste, A. *et al.* Apoptosis in Human Acute Myocardial Infarction. *Circulation* **95**, 320–323 (1997).

49. Anversa, P. *et al.* Apoptosis and myocardial infarction. *Basic Research in Cardiology 1998 93:3* **93**, s008-s012 (1998).

50. Frangogiannis, N. G., Smith, C. W. & Entman, M. L. The inflammatory response in myocardial infarction. *Cardiovascular Research* **53**, 31–47 (2002).

51. Sun, Y. *et al.* Infarct scar as living tissue. *Basic Res Cardiol* **97**, 343–347 (2002).

52. Pasumarthi, K. B. S., Nakajima, H., Nakajima, H. O., Soonpaa, M. H. & Field, L. J. Targeted expression of cyclin D2 results in cardiomyocyte DNA synthesis and infarct regression in transgenic mice. *Circulation Research* **96**, 110–118 (2005).

53. Ma, Y., Iyer, R. P., Jung, M., Czubryt, M. P. & Lindsey, M. L. Cardiac Fibroblast Activation Post-Myocardial Infarction: Current Knowledge Gaps. *Trends in Pharmacological Sciences* **38**, 448–458 (2017).

54. Willems, I. E. M. G., Havenith, M. G., de Mey, J. G. R. & Daemen, M. J. A. P. The alpha-smooth muscle actin-positive cells in healing human myocardial scars. *The American Journal of Pathology* **145**, 868 (1994).

55. van Putten, S., Shafieyan, Y. & Hinz, B. Mechanical control of cardiac myofibroblasts. *Journal of Molecular and Cellular Cardiology* **93**, 133–142 (2016).

56. Davis, J. & Molkentin, J. D. Myofibroblasts: Trust your heart and let fate decide. *Journal of Molecular and Cellular Cardiology* **70**, 9–18 (2014).

57. Jeong, D. *et al.* Matricellular Protein CCN5 Reverses Established Cardiac Fibrosis. *J Am Coll Cardiol* **67**, 1556–1568 (2016).

58. Weber, K. T., Sun, Y., Bhattacharya, S. K., Ahokas, R. A. & Gerling, I. C. Myofibroblast-mediated mechanisms of pathological remodelling of the heart. *Nature Reviews Cardiology* **10**, 15–26 (2013).

59. Deddens, J. C. *et al.* Modeling the Human Scarred Heart In Vitro: Toward New Tissue Engineered Models. *Advanced Healthcare Materials* **201600571**, 1600571 (2016).

60. Rienks, M., Papageorgiou, A. P., Frangogiannis, N. G. & Heymans, S. Myocardial extracellular matrix: An ever-changing and diverse entity. *Circulation Research* **114**, 872–888 (2014).

61. Wu, X., Reboll, M. R., Korf-Klingebiel, M. & Wollert, K. C. Angiogenesis after acute myocardial infarction. *Cardiovascular Research* **117**, 1257–1273 (2021).

62. Zhao, T., Zhao, W., Chen, Y., Ahokas, R. A. & Sun, Y. Vascular endothelial growth factor (VEGF)-A: Role on cardiac angiogenesis following myocardial infarction. *Microvascular Research* **80**, 188–194 (2010).

63. Mollova, M. *et al.* Cardiomyocyte proliferation contributes to heart growth in young humans. *Proc Natl Acad Sci U S A* **110**, 1446–1451 (2013).

64. Yutzey, K. E. Cardiomyocyte Proliferation: Teaching an old dogma new tricks. *Circ Res* **120**, 627 (2017).

65. He, L. & Zhou, B. Cardiomyocyte proliferation: remove brakes and push accelerators. *Cell Research 2017 27:8* **27**, 959–960 (2017).

66. Bergmann, O. *et al.* Evidence for cardiomyocyte renewal in humans. *Science* **324**, 98 (2009).

67. Porrello, E. R. *et al.* Transient regenerative potential of the neonatal mouse heart. *Science (1979)* **331**, 1078–1080 (2011).

68. st. John Sutton, M. G. & Sharpe, N. Left Ventricular Remodeling After Myocardial Infarction. *Circulation* **101**, 2981–2988 (2000).

69. Holmes, J. W., Nuñez, J. A. & Covell, J. W. Functional implications of myocardial scar structure. *https://doi.org/10.1152/ajpheart.1997.272.5.H2123* **272**, (1997).

70. Fomovsky, G. M. & Holmes, J. W. Evolution of scar structure, mechanics, and ventricular function after myocardial infarction in the rat. *American Journal of Physiology - Heart and Circulatory Physiology* **298**, 221–228 (2010).

71. Fomovsky, G. M., Rouillard, A. D. & Holmes, J. W. Regional mechanics determine collagen fiber structure in healing myocardial infarcts. *Journal of Molecular and Cellular Cardiology* **52**, 1083–1090 (2012).

72. Weisman, H. F., Bush, D. E., Mannisi, J. A., Weisfeldt, M. L. & Healy, B. Cellular mechanisms of myocardial infarct expansion. *Circulation* **78**, 186–201 (1988).

73. Hochman, J. S. & Bulkley, B. H. Expansion of acute myocardial infarction: an experimental study. *Circulation* **65**, 1446–1450 (1982).

74. Lew, W. Y. W., Cehn, Z., Guth, B. & Covell, J. W. Mechanisms of augmented segment shortening in nonischemic areas during acute ischemia of the canine left ventricle. *Circulation Research* **56**, 351–358 (1985).

75. Kieken, F. *et al.* Structural and molecular mechanisms of gap junction remodeling in epicardial border zone myocytes following myocardial infarction. *Circulation Research* **104**, 1103–1112 (2009).

76. Gardner, P. I., Ursell, P. C., Fenoglio, J. J. & Wit, A. L. Electrophysiologic and anatomic basis for fractionated electrograms recorded from healed myocardial infarcts. *Circulation* **72**, 596–611 (1985).

77. Camelliti, P., Devlin, G. P., Matthews, K. G., Kohl, P. & Green, C. R. Spatially and temporally distinct expression of fibroblast connexins after sheep ventricular infarction. *Cardiovascular Research* **62**, 415–425 (2004).

78. Kohl, P., Camelliti, P., Burton, F. L. & Smith, G. L. Electrical coupling of fibroblasts and myocytes: relevance for cardiac propagation. *Journal of Electrocardiology* **38**, 45–50 (2005).

79. de Bakker, J. M. T. *et al.* Slow conduction in the infarcted human heart: "Zigzag" course of activation. *Circulation* **88**, 915–926 (1993).

80. Dillon, S. M., Allessie, M. A., Ursell, P. C. & Wit, A. L. Influences of anisotropic tissue structure on reentrant circuits in the epicardial border zone of subacute canine infarcts. *Circulation Research* **63**, 182–206 (1988).

81. Jenča, D. *et al.* Heart failure after myocardial infarction: incidence and predictors. *ESC Heart Failure* **8**, 222–237 (2021).

82. Shen, H. *et al.* Follistatin-like 1 protects mesenchymal stem cells from hypoxic damage and enhances their therapeutic efficacy in a mouse myocardial infarction model. *Stem Cell Research and Therapy* **10**, 1–14 (2019).

83. Gabisonia, K. *et al.* MicroRNA therapy stimulates uncontrolled cardiac repair after myocardial infarction in pigs. *Nature* **569**, 418–422 (2019).

84. Gao, F. *et al.* Therapeutic role of miR-19a/19b in cardiac regeneration and protection from myocardial infarction. *Nature Communications* **10**, (2019).

85. Pang, J. K. S., Phua, Q. H. & Soh, B. S. Applications of miRNAs in cardiac development, disease progression and regeneration. *Stem Cell Research and Therapy* **10**, 1–11 (2019).

86. Murry, C. E. & MacLellan, W. R. Stem cells and the heart - The road ahead. *Science (1979)* **367**, 854–855 (2020).

87. Tachibana, A. *et al.* Paracrine Effects of the Pluripotent Stem Cell-Derived Cardiac Myocytes Salvage the Injured Myocardium. 22–36 (2017) doi:10.1161/CIRCRESAHA.117.310803.

88. Huang, K., Hu, S. & Cheng, K. A New Era of Cardiac Cell Therapy: Opportunities and Challenges. *Advanced Healthcare Materials* **8**, 1–18 (2019).

89. Jackman, C. P. *et al.* Engineered cardiac tissue patch maintains structural and electrical properties after epicardial implantation. *Biomaterials* **159**, 48–58 (2018).

90. Shadrin, I. Y. *et al.* Cardiopatch platform enables maturation and scale-up of human pluripotent stem cell-derived engineered heart tissues. *Nature Communications 2017 8:1* **8**, 1–15 (2017).

91. Wang, L., Liu, Y. & Ye, G. ✉. Injectable and conductive cardiac patches repair infarcted myocardium in rats and minipigs. doi:10.1038/s41551-021-00796-9.

92. Querdel, E. *et al.* Human Engineered Heart Tissue Patches Remuscularize the Injured Heart in a Dose-Dependent Manner. *Circulation* **143**, 1991–2006 (2021).

93. Desgres, M. & Menasché, P. Clinical Translation of Pluripotent Stem Cell Therapies: Challenges and Considerations. *Cell Stem Cell* **25**, 594–606 (2019).

94. Kim, H. K., Missiakas, D. & Schneewind, O. Mouse models for infectious diseases caused by Staphylococcus aureus. *Journal of Immunological Methods* **410**, 88–99 (2014).

95. Fine, B. & Vunjak-Novakovic, G. Shortcomings of Animal Models and the Rise of Engineered Human Cardiac Tissue. *ACS Biomaterials Science & Engineering* acsbiomaterials.6b00662 (2017) doi:10.1021/acsbiomaterials.6b00662.

96. Vunjak Novakovic, G., Eschenhagen, T. & Mummery, C. Myocardial Tissue Engineering: In Vitro Models. *Cold Spring Harbor Perspectives in Medicine* **4**, 1–15 (2014).

97. Kumar, M. *et al.* Animal models of myocardial infarction: Mainstay in clinical translation. *Regulatory Toxicology and Pharmacology* **76**, 221–230 (2016).

98. Shin, H. S., Shin, H. H. & Shudo, Y. Current Status and Limitations of Myocardial Infarction Large Animal Models in Cardiovascular Translational Research. *Frontiers in Bioengineering and Biotechnology* **9**, 321 (2021).

99. Lukács, E. *et al.* Overview of large animal myocardial infarction models (review). *Acta Physiologica Hungarica* **99**, 365–381 (2012).

100. Lian, X. *et al.* Directed cardiomyocyte differentiation from human pluripotent stem cells by modulating Wnt/β-catenin signaling under fully defined conditions. *Nature Protocols 2013 8:1* **8**, 162–175 (2012).

101. Le, M. N. T. & Hasegawa, K. Expansion Culture of Human Pluripotent Stem Cells and Production of Cardiomyocytes. *Bioengineering 2019, Vol. 6, Page 48* **6**, 48 (2019).

102. Wu, P. *et al.* Maturation strategies and limitations of induced pluripotent stem cell-derived cardiomyocytes. *Bioscience Reports* **41**, 20200833 (2021).

103. Tu, C., Chao, B. S. & Wu, J. C. Strategies for improving the maturity of human induced pluripotent stem cell-derived cardiomyocytes. *Circulation Research* **123**, 512–514 (2018).

104. Sun, X. & Nunes, S. S. Biowire platform for maturation of human pluripotent stem cell-derived cardiomyocytes. *Methods* **101**, 21–26 (2016).

105. Zimmermann, W. H., Melnychenko, I. & Eschenhagen, T. Engineered heart tissue for regeneration of diseased hearts. *Biomaterials* **25**, 1639–1647 (2004).

106. Ronaldson-Bouchard, K. *et al.* Advanced maturation of human cardiac tissue grown from pluripotent stem cells. *Nature 2018 556:7700* **556**, 239–243 (2018).

107. Zhao, Y., Eng, G., Lee, B. W., Radisic, M. & Vunjak-Novakovic, G. Cardiac tissue engineering. *Principles of Tissue Engineering* 593–616 (2020) doi:10.1016/B978-0-12-818422-6.00033-2.

108. Boudou, T. *et al.* A microfabricated platform to measure and manipulate the mechanics of engineered cardiac microtissues. *Tissue Engineering - Part A* **18**, 910–919 (2012).

109. Liau, B., Zhang, D. & Bursac, N. Functional cardiac tissue engineering. *Regenerative Med* **7**, 187 (2012).

110. Montgomery, M., Zhang, B. & Radisic, M. Cardiac Tissue Vascularization: From Angiogenesis to Microfluidic Blood Vessels. *J Cardiovasc Pharmacol Ther* **19**, 382–393 (2014).

111. Virag, J. I. & Murry, C. E. Myofibroblast and Endothelial Cell Proliferation during Murine Myocardial Infarct Repair. *The American Journal of Pathology* **163**, 2433–2440 (2003).

112. Fink, C. *et al.* Three-dimensional engineered heart tissue from neonatal rat cardiac myocytes Three-Dimensional Engineered Heart. **0290**, (2000).

113. Radisic, M. *et al.* Functional assembly of engineered myocardium by electrical stimulation of cardiac myocytes cultured on scaffolds. *Proc Natl Acad Sci U S A* **101**, 18129–18134 (2004).

114. Thavandiran, N. *et al.* Design and formulation of functional pluripotent stem cell-derived cardiac microtissues. *Proc Natl Acad Sci U S A* **110**, E4698-707 (2013).

115. Ronaldson-Bouchard, K. *et al.* Advanced maturation of human cardiac tissue grown from pluripotent stem cells. *Nature* **556**, 239–243 (2018).

116. Lian, X. *et al.* Cozzarelli Prize Winner: Robust cardiomyocyte differentiation from human pluripotent stem cells via temporal modulation of canonical Wnt signaling. *Proceedings of the National Academy of Sciences* **109**, E1848–E1857 (2012).

117. Chen, T. & Vunjak-Novakovic, G. In vitro Models of Ischemia-Reperfusion Injury. *Regen Eng Transl Med* **4**, 142–153 (2018).

118. Chen, T. & Vunjak-Novakovic, G. Human Tissue-Engineered Model of Myocardial Ischemia-Reperfusion Injury. *Tissue Engineering - Part A* **25**, 711–724 (2019).

119. Lee, M. O. *et al.* Modelling cardiac fibrosis using three-dimensional cardiac microtissues derived from human embryonic stem cells. *Journal of Biological Engineering* **13**, 1–17 (2019).

120. van Spreeuwel, A. C. C. *et al.* Mimicking Cardiac Fibrosis in a Dish: Fibroblast Density Rather than Collagen Density Weakens Cardiomyocyte Function. *Journal of Cardiovascular Translational Research* **10**, 116–127 (2017).

121. Bracco Gartner, T. C. L. *et al.* Anti-fibrotic Effects of Cardiac Progenitor Cells in a 3D-Model of Human Cardiac Fibrosis. *Frontiers in Cardiovascular Medicine* **6**, 1–11 (2019).

122. Sadeghi, A. H. *et al.* Engineered 3D Cardiac Fibrotic Tissue to Study Fibrotic Remodeling. *Advanced Healthcare Materials* **1601434**, 1601434 (2017).

123. Katare, R. G., Ando, M., Kakinuma, Y. & Sato, T. Engineered Heart Tissue: A Novel Tool to Study the Ischemic Changes of the Heart In Vitro. *PLOS ONE* **5**, e9275 (2010).

124. Chen, T. & Vunjak-Novakovic, G. Human Tissue-Engineered Model of Myocardial Ischemia-Reperfusion Injury. *Tissue Engineering - Part A* **25**, 711–724 (2019).

125. Lee, M. O. *et al.* Modelling cardiac fibrosis using three-dimensional cardiac microtissues derived from human embryonic stem cells. *Journal of Biological Engineering* **13**, 1–17 (2019).

126. Mastikhina, O. *et al.* Human cardiac fibrosis-on-a-chip model recapitulates disease hallmarks and can serve as a platform for drug testing. *Biomaterials* **233**, (2020).

127. Bracco Gartner, T. C. L. *et al.* Anti-fibrotic Effects of Cardiac Progenitor Cells in a 3D-Model of Human Cardiac Fibrosis. *Frontiers in Cardiovascular Medicine* **6**, 52 (2019).

128. Daly, A. C., Davidson, M. D. & Burdick, J. A. 3D bioprinting of high cell-density heterogeneous tissue models through spheroid fusion within self-healing hydrogels. *Nature Communications 2021 12:1* **12**, 1–13 (2021).

129. Wang, E. Y. *et al.* Biowire Model of Interstitial and Focal Cardiac Fibrosis. *ACS Central Science* **5**, 1146–1158 (2019).

130. Richards, D. J. *et al.* Human cardiac organoids for the modelling of myocardial infarction and drug cardiotoxicity. *Nat Biomed Eng* **4**, 446 (2020).

131. Shroff, S. N. *et al.* Voltage Imaging of Cardiac Cells and Tissue Using the Genetically Encoded Voltage Sensor Archon1. *iScience* **23**, 100974 (2020).

132. Das, S. L. *et al.* Extracellular Matrix Alignment Directs Provisional Matrix Assembly and Three Dimensional Fibrous Tissue Closure. *Tissue Engineering - Part A* **27**, 1447–1457 (2021).

133. Mozaffarian, D. *et al.* Heart Disease and Stroke Statistics—2016 Update. *Circulation* **133**, e38–e48 (2016).

134. Sun, Y. & Weber, K. T. Infarct scar: A dynamic tissue. *Cardiovascular Research* **46**, 250–256 (2000).

135. Anversa, P., Beghi, C., Kikkawa, Y. & Olivetti, G. Myocardial response to infarction in the rat. Morphometric measurement of infarct size and myocyte cellular hypertrophy. *The American Journal of Pathology* **118**, 484 (1985).

136. Pfeffer, M. A. & Braunwald, E. Ventricular remodeling after myocardial infarction. Experimental observations and clinical implications. *Circulation* **81**, 1161–1172 (1990).

137. Gaudron, P., Eilles, C., Kugler, I. & Ertl, G. Progressive left ventricular dysfunction and remodeling after myocardial infarction. Potential mechanisms and early predictors. *Circulation* **87**, 755–763 (1993).

138. Liu, H. *et al.* Heart-on-a-Chip Model with Integrated Extra- And Intracellular Bioelectronics for Monitoring Cardiac Electrophysiology under Acute Hypoxia. *Nano Letters* **20**, 2585–2593 (2020).

139. Acun, A. & Zorlutuna, P. Engineered Myocardium Model to Study the Roles of HIF-1α and HIF1A-AS1 in Paracrine-only Signaling under Pathological Level Oxidative Stress. *Acta Biomater* **58**, 323 (2017).

140. Sadeghi, A. H. *et al.* Engineered Three-Dimensional Cardiac Fibrotic Tissue to Study Fibrotic Remodeling. *Advanced Healthcare Materials* **6**, 11–39 (2017).

141. Sadeghi, A. H. *et al.* Engineered 3D Cardiac Fibrotic Tissue to Study Fibrotic Remodeling. *Adv Healthc Mater* **6**, (2017).

142. Sharma, A. *et al.* CRISPR/Cas9-Mediated Fluorescent Tagging of Endogenous Proteins in Human Pluripotent Stem Cells. *Current Protocols in Human Genetics* **96**, 21.11.1-21.11.20 (2018).

143. Professional, G. B.-Dr. D. J. S. T. for the & 2000, undefined. The openCV library. *elibrary.ru*.

144. Virtanen, P. *et al.* SciPy 1.0: fundamental algorithms for scientific computing in Python. *Nature Methods 2020 17:3* **17**, 261–272 (2020).

145. van der Walt, S. *et al.* Scikit-image: Image processing in python. *PeerJ* **2014**, e453 (2014).

146. Legant, W. R. *et al.* Microfabricated tissue gauges to measure and manipulate forces from 3D microtissues. *Proc Natl Acad Sci U S A* **106**, 10097–10102 (2009).

147. Harris, C. R. *et al.* Array programming with NumPy. *Nature 2020 585:7825* **585**, 357–362 (2020).

148. Shi, J. & Tomasi, C. Good features to track. *Proceedings of the IEEE Computer Society Conference on Computer Vision and Pattern Recognition* 593–600 (1994) doi:10.1109/CVPR.1994.323794.

149. Lucas, B. & Kanade, T. An iterative image registration technique with an application to stereo vision. (1981).

150. Lejeune, E. & Linder, C. Quantifying the relationship between cell division angle and morphogenesis through computational modeling. *Journal of Theoretical Biology* **418**, 1–7 (2017).

151. Sato, S. *et al.* Nanosecond, high-intensity pulsed laser ablation of myocardium tissue at the ultraviolet, visible, and near-infrared wavelengths: In-vitro study. *Lasers in Surgery and Medicine* **29**, 464–473 (2001).

152. Shen, N., Schaffer, C. B., Datta, D. & Mazur, E. Photodisruption in biological tissues and single cells using femtosecond laser pulses. *Conference on Lasers and Electro-Optics Europe - Technical Digest* 403–404 (2001) doi:10.1109/CLEO.2001.947974.

153. Thompson, K. P., Ren, Q. S. & Parel, J. M. Therapeutic and Diagnostic Application of Lasers in Ophthalmology. *Proceedings of the IEEE* **80**, 838–860 (1992).

154. Walsh, J. T., Flotte, T. J. & Deutsch, T. F. Er:YAG laser ablation of tissue: Effect of pulse duration and tissue type on thermal damage. *Lasers in Surgery and Medicine* **9**, 314–326 (1989).

155. Ogura, M. *et al.* Myocardium tissue ablation with high-peak-power nanosecond 1,064- and 532-nm pulsed lasers: Influence of laser-induced plasma. *Lasers in Surgery and Medicine* **31**, 136–141 (2002).

156. Stelzle, F. *et al.* The impact of laser ablation on optical soft tissue differentiation for tissue specific laser surgery-an experimental ex vivo study. *Journal of Translational Medicine* **10**, 1–10 (2012).

157. Vogel, A. & Venugopalan, V. Mechanisms of pulsed laser ablation of biological tissues. *Chemical Reviews* **103**, 577–644 (2003).

158. Pfeffer, M., Circulation, J. P.- & 1987, undefined. Ventricular enlargement and reduced survival after myocardial infarction. *europepmc.org*.

159. Ummel, R. R., Rutsch, W. & Schmutzler, H. Left ventricular hyperkinesis in acute myocardial infarction and at control angiography after 1 month. *Eur Heart J* **11**, 740–748 (1990).

160. Tennant, R. & Wiggers, C. J. The Effect of Coronary Occlusion on Myocardial Contraction. *https://doi.org/10.1152/ajplegacy.1935.112.2.351* **112**, 351–361 (1935).

161. Nahrendorf, M. *et al.* The healing myocardium sequentially mobilizes two monocyte subsets with divergent and complementary functions. *J Exp Med* **204**, 3037–3047 (2007).

162. Wynn, T. A. & Ramalingam, T. R. Mechanisms of fibrosis: therapeutic translation for fibrotic disease. *Nature Medicine 2012 18:7* **18**, 1028–1040 (2012).

163. Fadok, V. A. *et al.* Macrophages that have ingested apoptotic cells in vitro inhibit proinflammatory cytokine production through autocrine/paracrine mechanisms involving TGF-beta, PGE2, and PAF. *J Clin Invest* **101**, 890–898 (1998).

164. Zhang, W. *et al.* Necrotic myocardial cells release damage-associated molecular patterns that provoke fibroblast activation in vitro and trigger myocardial inflammation and fibrosis in vivo. *J Am Heart Assoc* **4**, (2015).

165. Ninh, V. K. & Brown, J. H. The contribution of the cardiomyocyte to tissue inflammation in cardiomyopathies. *Curr Opin Physiol* **19**, 129 (2021).

166. Turner, N. A. Inflammatory and fibrotic responses of cardiac fibroblasts to myocardial damage associated molecular patterns (DAMPs). *J Mol Cell Cardiol* **94**, 189–200 (2016).

167. Aoyagi, T., therapy, T. M.-J. of cell science & & 2011, undefined. The cardiomyocyte as a source of cytokines in cardiac injury. *ncbi.nlm.nih.gov*.

168. Bers, D. M. Cardiac excitation–contraction coupling. *Nature 2002 415:6868* **415**, 198–205 (2002).

169. Bers, D. M. Calcium cycling and signaling in cardiac myocytes. *Annual Review of Physiology* **70**, 23–49 (2008).

170. Eisner, D. A., Caldwell, J. L., Kistamás, K. & Trafford, A. W. Calcium and Excitation-Contraction Coupling in the Heart. *Circulation Research* **121**, 181–195 (2017).

171. Hobai, I. A. & O'Rourke, B. Decreased sarcoplasmic reticulum calcium content is responsible for defective excitation-contraction coupling in canine heart failure. *Circulation* **103**, 1577–1584 (2001).

172. Leyton-Mange, J. S. & Milan, D. J. Pluripotent stem cells as a platform for cardiac arrhythmia drug screening. *Current Treatment Options in Cardiovascular Medicine* **16**, (2014).

173. Leyton-Mange, J., Mills, R., Macri, V., reports, M. J.-S. cell & 2014, undefined. Rapid cellular phenotyping of human pluripotent stem cell-derived cardiomyocytes using a genetically encoded fluorescent voltage sensor. *Elsevier*.

174. Olivari, M. T. *et al.* Treatment of hypertension with nifedipine, a calcium antagonistic agent. *Circulation* **59**, 1056–1062 (1979).

175. Peng, S., Lacerda, A., Kirsch, G., ... A. B.-... of pharmacological and & 2010, undefined. The action potential and comparative pharmacology of stem cell-derived human cardiomyocytes. *Elsevier*.

176. Sanguinetti, M. C. & Jurkiewicz, N. K. Delayed rectifier outward K+ current is composed of two currents in guinea pig atrial cells. *American Journal of Physiology - Heart and Circulatory Physiology* **260**, (1991).

177. Sanguinetti, M. C., Kurkiewicz, N. K., Scott, A. & Siegl, P. K. S. Isoproterenol antagonizes prolongation of refractory period by the class III antiarrhythmic agent E-4031 in guinea pig myocytes. Mechanism of action. *Circulation Research* **68**, 77–84 (1991).

178. Shaheen, N. *et al.* Human induced pluripotent stem cell-derived cardiac cell sheets expressing genetically encoded voltage indicator for pharmacological and arrhythmia studies. *Elsevier*.

179. Shinnawi, R., Huber, I., Maizels, L., reports, N. S.-S. cell & 2015, undefined. Monitoring human-induced pluripotent stem cell-derived cardiomyocytes with genetically encoded calcium and voltage fluorescent reporters. *Elsevier*.

180. Song, L. *et al.* Dual Optical Recordings for Action Potentials and Calcium Handling in Induced Pluripotent Stem Cell Models of Cardiac Arrhythmias Using Genetically Encoded Fluorescent Indicators. *Stem Cells Translational Medicine* **4**, 468–475 (2015).

181. Entcheva, E. & Bien, H. Macroscopic optical mapping of excitation in cardiac cell networks with ultra-high spatiotemporal resolution. *Prog Biophys Mol Biol* **92**, 232–257 (2006).

182. Herron, T. J., Lee, P. & Jalife, J. Optical imaging of voltage and calcium in cardiac cells & tissues. *Circulation Research* **110**, 609–623 (2012).

183. Hortigon-Vinagre, M. P. *et al.* The use of ratiometric fluorescence measurements of the voltage sensitive dye Di-4-ANEPPS to examine action potential characteristics and drug effects on human induced pluripotent stem cell-derived cardiomyocytes. *Toxicological Sciences* **154**, 320–331 (2016).

184. Panáková, D., Werdich, A. A. & MacRae, C. A. Wnt11 patterns a myocardial electrical gradient through regulation of the L-type Ca2+ channel. *Nature* **466**, 874–878 (2010).

185. Salama, G. *et al.* Properties of new, long-wavelength, voltage-sensitive dyes in the heart. *Journal of Membrane Biology* **208**, 125–140 (2005).

186. Salama, G. & Morad, M. Merocyanine 540 as an optical probe of transmembrane electrical activity in the heart. *Science (1979)* **191**, 485–487 (1976).

187. Hou, J. H., Kralj, J. M., Douglass, A. D., Engert, F. & Cohen, A. E. Simultaneous mapping of membrane voltage and calcium in zebrafish heart in vivo reveals

chamber-specific developmental transitions in ionic currents. *Frontiers in Physiology* **5 AUG**, (2014).

188. Abdelfattah, A. S. *et al.* Bright and photostable chemigenetic indicators for extended in vivo voltage imaging. *Science (1979)* **365**, 699–704 (2019).

189. Adam, Y. *et al.* Voltage imaging and optogenetics reveal behaviour-dependent changes in hippocampal dynamics. *Nature* **569**, 413–417 (2019).

190. Chamberland, S. *et al.* Fast two-photon imaging of subcellular voltage dynamics in neuronal tissue with genetically encoded indicators. *Elife* **6**, (2017).

191. Flytzanis, N., Bedbrook, C., … H. C.-N. & 2014, undefined. Archaerhodopsin variants with enhanced voltage-sensitive fluorescence in mammalian and Caenorhabditis elegans neurons. *nature.com*.

192. Gong, Y., Wagner, M., Li, J. Z., communications, M. S.-N. & 2014, undefined. Imaging neural spiking in brain tissue using FRET-opsin protein voltage sensors. *nature.com*.

193. Gong, Y. *et al.* High-speed recording of neural spikes in awake mice and flies with a fluorescent voltage sensor. *Science (1979)* **350**, 1361–1366 (2015).

194. Hochbaum, D. R. *et al.* All-optical electrophysiology in mammalian neurons using engineered microbial rhodopsins. *Nature Methods* **11**, 825–833 (2014).

195. Jin, L. *et al.* Single action potentials and subthreshold electrical events imaged in neurons with a fluorescent protein voltage probe. *Elsevier*.

196. Lou, S. *et al.* Genetically targeted all-optical electrophysiology with a transgenic cre-dependent optopatch mouse. *Soc Neuroscience* (2016) doi:10.1523/JNEUROSCI.1582-16.2016.

197. Piatkevich, K. D. *et al.* Erratum to: A robotic multidimensional directed evolution approach applied to fluorescent voltage reporters (Nature Chemical Biology, (2018), 14, 4, (352-360), 10.1038/s41589-018-0004-9). *Nature Chemical Biology* **14**, 901 (2018).

198. St-Pierre, F. *et al.* High-fidelity optical reporting of neuronal electrical activity with an ultrafast fluorescent voltage sensor. *Nature Neuroscience* **17**, 884–889 (2014).

199. Villette, V. *et al.* Ultrafast two-photon imaging of a high-gain voltage indicator in awake behaving mice. *Elsevier*.

200. Zou, P. *et al.* Bright and fast multicoloured voltage reporters via electrochromic FRET. *nature.com* (2014) doi:10.1038/ncomms5625.

201. Johnston, C., Krafft, A., … M. R.- & 2018, undefined. A new look at the heart—novel imaging techniques. *Springer*.

202. Liao, M. L. C. *et al.* Sensing Cardiac Electrical Activity with a Cardiac Myocyte-Targeted Optogenetic Voltage Indicator. *Circulation Research* **117**, 401–412 (2015).

203. Mutoh, H. *et al.* Spectrally-resolved response properties of the three most advanced FRET based fluorescent protein voltage probes. *PLoS ONE* **4**, (2009).

204. Tsutsui, H., Higashijima, S. ichi, Miyawaki, A. & Okamura, Y. Visualizing voltage dynamics in zebrafish heart. *Journal of Physiology* **588**, 2017–2021 (2010).

205. van Opbergen, C. J. M. *et al.* Optogenetic sensors in the zebrafish heart: A novel in vivo electrophysiological tool to study cardiac arrhythmogenesis. *Theranostics* **8**, 4750–4764 (2018).

206. Lee, S. *et al.* Improving a genetically encoded voltage indicator by modifying the cytoplasmic charge composition. *nature.com*.

207. Nakajima, R., Jung, A., Yoon, B. J. & Baker, B. J. Optogenetic monitoring of synaptic activity with genetically encoded voltage indicators. *Frontiers in Synaptic Neuroscience* **8**, (2016).

208. Storace, D., Rad, M., Kang, B., ... L. C.-T. in & 2016, undefined. Toward better genetically encoded sensors of membrane potential. *Elsevier*.

209. Kaestner, L. *et al.* Genetically encoded voltage indicators in circulation research. *International Journal of Molecular Sciences* **16**, 21626–21642 (2015).

210. Lundby, A., Mutoh, H., Dimitrov, D., Akemann, W. & Knöpfel, T. Engineering of a genetically encodable fluorescent voltage sensor exploiting fast Ci-VSP voltage-sensing movements. *PLoS ONE* **3**, (2008).

211. Piatkevich, K. D. *et al.* Population imaging of neural activity in awake behaving mice. *Nature* **574**, 413–417 (2019).

212. Faivre, J., Forest, M., Gout, B., pharmacology, A. B.-E. journal of & 1999, undefined. Electrophysiological characterization of BRL-32872 in canine Purkinje fiber and ventricular muscle: Effect on early after-depolarizations and repolarization. *Elsevier*.

213. Ma, J. *et al.* High purity human-induced pluripotent stem cell-derived cardiomyocytes: Electrophysiological properties of action potentials and ionic currents. *American Journal of Physiology - Heart and Circulatory Physiology* **301**, (2011).

214. Maddah, M. *et al.* A non-invasive platform for functional characterization of stem-cell-derived cardiomyocytes with applications in cardiotoxicity testing. *Stem Cell Reports* **4**, 621–631 (2015).

215. Scheel, O. *et al.* Action potential characterization of human induced pluripotent stem cell-derived cardiomyocytes using automated patch-clamp technology. *Assay and Drug Development Technologies* **12**, 457–469 (2014).

216. Nunes, S. S. *et al.* Biowire: A platform for maturation of human pluripotent stem cell-derived cardiomyocytes. *Nature Methods* **10**, 781–787 (2013).

217. Ronaldson-Bouchard, K. *et al.* Advanced maturation of human cardiac tissue grown from pluripotent stem cells. *Nature* **556**, 239–243 (2018).

218. Tu, C., Chao, B. S. & Wu, J. C. Strategies for improving the maturity of human induced pluripotent stem cell-derived cardiomyocytes. *Circulation Research* **123**, 512–514 (2018).

219. Zimmermann, W. H. *et al.* Tissue engineering of a differentiated cardiac muscle construct. *Circulation Research* **90**, 223–230 (2002).

220. Stern, J. A. *et al.* A small molecule inhibitor of sarcomere contractility acutely relieves left ventricular outflow tract obstruction in feline hypertrophic cardiomyopathy. *PLoS ONE* **11**, (2016).

221. Dempsey, G., Chaudhary, K., ... N. A.-... of pharmacological and & 2016, undefined. Cardiotoxicity screening with simultaneous optogenetic pacing, voltage imaging and calcium imaging. *Elsevier*.

222. Beuckelmann, D. J., Näbauer, M. & Erdmann, E. Intracellular calcium handling in isolated ventricular myocytes from patients with terminal heart failure. *Circulation* **85**, 1046–1055 (1992).

223. Gwathmey, J. K. *et al.* Abnormal intracellular calcium handling in myocardium from patients with end-stage heart failure. *Circulation Research* **61**, 70–76 (1987).

224. Kääb, S. *et al.* Ionic mechanism of action potential prolongation in ventricular myocytes from dogs with pacing-induced heart failure. *Circulation Research* **78**, 262–273 (1996).

225. Splawski, I. *et al.* Severe arrhythmia disorder caused by cardiac L-type calcium channel mutations. *Proc Natl Acad Sci U S A* **102**, 8089–8096 (2005).

226. Lenselink, E. A. Role of fibronectin in normal wound healing. *International Wound Journal* **12**, 313–316 (2015).

227. Poujade, M. *et al.* Collective migration of an epithelial monolayer in response to a model wound. *Proc Natl Acad Sci U S A* **104**, 15988–15993 (2007).

228. Werner, S., Krieg, T. & Smola, H. Keratinocyte-fibroblast interactions in wound healing. *Journal of Investigative Dermatology* **127**, 998–1008 (2007).

229. El Ghalbzouri, A. *et al.* Fibroblasts facilitate re-epithelialization in wounded human skin equivalents. *Laboratory Investigation* **84**, 102–112 (2004).

230. Pastar, I. *et al.* Epithelialization in Wound Healing: A Comprehensive Review. *Advances in Wound Care* **3**, 445–464 (2014).

231. Billingham, R. E. & Russel, P. S. Studies on wound healing, with special reference to the phenomenon of contracture in experimental wounds in rabbits' skin. *Ann Surg* **144**, 961–981 (1956).

232. Watts, G. Wound shape and tissue tension in healing. *British Journal of Surgery* **47**, 555–561 (1960).

233. Cardinal, M., Eisenbud, D. E. & Armstrong, D. G. Wound shape geometry measurements correlate to eventual wound healing. *Wound Repair and Regeneration* **17**, 173–178 (2009).

234. Vedula, S. R. K. *et al.* Mechanics of epithelial closure over non-adherent environments. *Nature Communications* **6**, 1–10 (2015).

235. Ravasio, A. *et al.* Gap geometry dictates epithelial closure efficiency. *Nature Communications* **6**, (2015).

236. Martin, P. & Lewis, J. Actin cables and epidermal movement in embryonic wound healing. *Nature* **360**, 179–183 (1992).

237. Jacinto, A., Woolner, S. & Martin, P. Dynamic analysis of dorsal closure in Drosophila: From genetics to cell biology. *Developmental Cell* **3**, 9–19 (2002).

238. Danjo, Y. & Gipson, I. K. Actin "purse string" filaments are anchored by E-cadherin-mediated adherens junctions at the leading edge of the epithelial wound, providing coordinated cell movement. *Journal of Cell Science* **111**, 3323–3332 (1998).

239. Bidan, C. M. *et al.* How linear tension converts to curvature: Geometric control of bone tissue growth. *PLoS ONE* **7**, (2012).

240. Bidan, C. M. *et al.* Geometry as a Factor for Tissue Growth: Towards Shape Optimization of Tissue Engineering Scaffolds. *Advanced Healthcare Materials* **2**, 186–194 (2013).

241. Knychala, J. *et al.* Pore geometry regulates early stage human bone marrow cell tissue formation and organisation. *Annals of Biomedical Engineering* **41**, 917–930 (2013).

242. Dehn, R. & Asprey, D. *Essential Clinical Procedures, 4th Edition*. (Elsevier, 2020).

243. Schreier, T., Degen, E. & Baschong, W. Fibroblast migration and proliferation during in vitro wound healing - A quantitative comparison between various growth factors and a low molecular weight blood dialyzate used in the clinic to normalize impaired wound healing. *Research in Experimental Medicine* **193**, 195–205 (1993).

244. Selman Sakar, M. *et al.* Cellular forces and matrix assembly coordinate fibrous tissue repair. *Nature Communications* **7**, 1–8 (2016).

245. Bose, P., Eyckmans, J., Nguyen, T. D., Chen, C. S. & Reich, D. H. Effects of Geometry on the Mechanics and Alignment of Three-Dimensional Engineered Microtissues. *ACS Biomaterials Science and Engineering* **5**, 3843–3855 (2019).

246. Foolen, J., Wunderli, S. L., Loerakker, S. & Snedeker, J. G. Tissue alignment enhances remodeling potential of tendon-derived cells - Lessons from a novel microtissue model of tendon scarring. *Matrix Biology* **65**, 14–29 (2018).

247. Preibisch, S., Saalfeld, S. & Tomancak, P. Globally optimal stitching of tiled 3D microscopic image acquisitions. *Bioinformatics* **25**, 1463–1465 (2009).

248. Boudaoud, A. *et al.* FibrilTool, an ImageJ plug-in to quantify fibrillar structures in raw microscopy images. *Nature Protocols* **9**, 457–463 (2014).

249. Alnæs, M. S. *et al.* The FEniCS Project Version 1.5. **3**, 9–23 (2015).

250. Logg, A., Mardal, K.-A. & Wells, G. *Automated Solution of Differential Equations by the Finite Element Method*. (Springer, 2012). doi:10.1007/978-3-642-23099-8.

251. Geuzaine, C. & Remacle, J.-F. Gmsh: A 3-D finite element mesh generator with built-in pre- and post-processing facilities. *International Journal for Numerical Methods in Engineering* **79**, 1309–1331 (2009).

252. Ambrosi, D. *et al.* Perspectives on biological growth and remodeling. *Journal of the Mechanics and Physics of Solids* **59**, 863–883 (2011).

253. Van Rossum, G., Guido & Drake, F. L. Python tutorial. *Amsterdam: Centrum voor Wiskunde en Informatica* **620**, (1995).

254. Harris, C. R. *et al.* Array programming with NumPy. *Nature* **585**, 357–362 (2020).

255. Hunter, J. D. Matplotlib: A 2D Graphics Environment. *Computing in Science & Engineering* **9**, 90–95 (2007).

256. Ehrig, S. *et al.* Surface tension determines tissue shape and growth kinetics. *Science Advances* **5**, 1–9 (2019).

257. Zordan, M. D., Mill, C. P., Riese, D. J. & Leary, J. F. A high throughput, interactive imaging, bright-field wound healing assay. *Cytometry Part A* **79 A**, 227–232 (2011).

258. Bao, M., Xie, J., Piruska, A., Hu, X. & Huck, W. T. S. Microfabricated Gaps Reveal the Effect of Geometrical Control in Wound Healing. *Advanced Healthcare Materials* **2000630**, 1–8 (2020).

259. Foolen, J., Yamashita, T. & Kollmannsberger, P. Shaping tissues by balancing active forces and geometric constraints. *Journal of Physics D: Applied Physics* **49**, (2015).

260. Mailand, E., Li, B., Eyckmans, J., Bouklas, N. & Sakar, M. S. Surface and Bulk Stresses Drive Morphological Changes in Fibrous Microtissues. *Biophysical Journal* **117**, 975–986 (2019).

261. Wang, W. Y. *et al.* Extracellular matrix alignment dictates the organization of focal adhesions and directs uniaxial cell migration. *APL Bioengineering* **2**, 046107 (2018).

262. Fraley, S. I. *et al.* Three-dimensional matrix fiber alignment modulates cell migration and MT1-MMP utility by spatially and temporally directing protrusions. *Scientific Reports* **5**, 1–13 (2015).

263. Sander, E. A., Barocas, V. H. & Tranquillo, R. T. Initial fiber alignment pattern alters extracellular matrix synthesis in fibroblast-populated fibrin gel cruciforms and correlates with predicted tension. *Annals of Biomedical Engineering* **39**, 714–729 (2011).

264. Piotrowski-Daspit, A. S., Nerger, B. A., Wolf, A. E., Sundaresan, S. & Nelson, C. M. Dynamics of Tissue-Induced Alignment of Fibrous Extracellular Matrix. *Biophysical Journal* **113**, 702–713 (2017).

265. Eastwood, M., Mudera, V. C., McGrouther, D. A. & Brown, R. A. Effect of precise mechanical loading on fibroblast populated collagen lattices: Morphological changes. *Cell Motility and the Cytoskeleton* **40**, 13–21 (1998).

266. Hao, Y. *et al.* Integrated analysis of multimodal single-cell data. *Cell* **184**, 3573-3587.e29 (2021).

267. Semenza, G. L. Hypoxia-Inducible Factor 1 and Cardiovascular Disease. *Annu Rev Physiol* **76**, 39 (2014).

268. Song, H. H. G. *et al.* Transient Support from Fibroblasts is Sufficient to Drive Functional Vascularization in Engineered Tissues. *Advanced Functional Materials* **30**, 2003777 (2020).

269. Laflamme, M. A. & Murry, C. E. Heart regeneration. *Nature 2011 473:7347* **473**, 326–335 (2011).

270. Braunwald, E. Cell-based therapy in cardiac regeneration: An overview. *Circulation Research* **123**, 132–137 (2018).

271. Menasché, P. Cell therapy trials for heart regeneration — lessons learned and future directions. *Nature Reviews Cardiology 2018 15:11* **15**, 659–671 (2018).

272. Wu, K. H., Mo, X. M., Han, Z. C. & Zhou, B. Stem Cell Engraftment and Survival in the Ischemic Heart. *The Annals of Thoracic Surgery* **92**, 1917–1925 (2011).

273. Mancuso, A. *et al.* Cardiac Stem Cell-Loaded Delivery Systems: A New Challenge for Myocardial Tissue Regeneration. *International Journal of Molecular Sciences* **21**, 7701 (2020).

274. Wu, K. H., Mo, X. M., Han, Z. C. & Zhou, B. Stem cell engraftment and survival in the ischemic heart. *Annals of Thoracic Surgery* **92**, 1917–1925 (2011).

275. Camacho, P., Fan, H., Liu, Z. & He, J. Q. Large Mammalian Animal Models of Heart Disease. *Journal of Cardiovascular Development and Disease* **3**, (2016).

276. Spannbauer, A. *et al.* Large Animal Models of Heart Failure With Reduced Ejection Fraction (HFrEF). *Frontiers in Cardiovascular Medicine* **6**, 117 (2019).

277. Portillo Esquivel, L. E. & Zhang, B. Application of Cell, Tissue, and Biomaterial Delivery in Cardiac Regenerative Therapy. *ACS Biomaterials Science and Engineering* **7**, 1000–1021 (2021).

278. Hastings, C. L. *et al.* Drug and cell delivery for cardiac regeneration. *Advanced Drug Delivery Reviews* **84**, 85–106 (2015).

279. Roth, G. A. *et al.* Global, Regional, and National Burden of Cardiovascular Diseases for 10 Causes, 1990 to 2015. *J Am Coll Cardiol* **70**, 1–25 (2017).

280. Zou, Z. *et al.* Time Trends in Cardiovascular Disease Mortality across the BRICS: An Age-Period-Cohort Analysis of Key Nations with Emerging Economies Using the Global Burden of Disease Study 2017. *Circulation* 790–799 (2020) doi:10.1161/CIRCULATIONAHA.119.042864.

281. Elliott, N. T. & Yuan, F. A Review of Three-Dimensional In Vitro Tissue Models for Drug Discovery and Transport Studies. *Journal of Pharmaceutical Sciences* **100**, 59–74 (2011).